Dissertation

submitted to the

Combined Faculties of the Natural Sciences and Mathematics

of the Ruperto-Carola-University of Heidelberg, Germany

for the degree of

Doctor of Natural Sciences

put forward by

M. Sc. Niklas Michel

born in Salzkotten, Germany

Oral examination: February 6th, 2019

Relativistic theory
of nuclear structure effects
in heavy atomic systems

Zusammenfassung

In dieser Arbeit werden verschiedene Einflüsse der Kernstruktur und der Korrekturen der Quantenelektrodynamik (QED) auf die Spektren wasserstoffartiger Systeme untersucht. Im ersten Teil geht es um die Struktur gebundener Zustände zwischen einem Myon und einem Atomkern, sogenannter myonischer Atome. Hierbei werden präzise Berechnungen der Übergangsenergien und -wahrscheinlichkeiten mit modernen numerischen Methoden durchgeführt. QED Korrekturen, Hyperfeinaufspaltung und die Wechselwirkung mit Hüllenelektronen werden berücksichtigt und die Ausdehnung des Atomkerns wird ohne Störungstheorie behandelt. Des Weiteren werden neue Methoden für die Berechnung von Korrekturen höherer Ordnung zu der Hyperfeinstruktur präsentiert. Dies beinhaltet eine vollständige Berechnung der Hyperfeinaufspaltung zweiter Ordnung und Korrekturen aufgrund von Vakuumpolarisationseffekten für Quadrupolverteilungen im Innern des Atomkerns. In Verbindung mit kürzlich durchgeführten Experimenten wird das Quadrupolemoment von $^{185}_{75}$Re und $^{187}_{75}$Re Kernen ermittelt. Im zweiten Teil dieser Arbeit wird der g-Faktor des gebundenen Elektrons untersucht, welcher von der Form der Ladungsverteilung im Atomkern abhängt. Ein numerischer, nicht-perturbativer Ansatz für die Berechnung der entsprechenden Kernformkorrektur zum g-Faktor wird vorgestellt und Implikationen für die Unsicherheiten theoretischer Vorhersagen werden diskutiert. Im Besonderen kann die Modellabhängigkeit der Kerngrößenkorrektur zum g-Faktor aufgrund des besseren Modells für die Ladungsverteilung im Kern verringert werden. Des weiteren tragen Berechnungen der Kerngrößen- und Vakuumpolarisationskorrekturen für den g-Faktor des gebundenen Myons in $^4_2$He zu einer Vorhersage auf dem 10^{-9} Niveau bei. Wie in einer früheren Arbeit gezeigt, könnte in experimenteller Wert mit derselben Genauigkeit eine genauere Ermittlung der Myonmasse oder des magnetischen Moments des Myons ermöglichen.

Abstract

In this thesis, several aspects of nuclear structure effects and corrections from quantum electrodynamics (QED) in the spectra of hydrogen-like systems are investigated. The first part is concerned with the structure of bound states between a muon and an atomic nucleus, so-called muonic atoms. Here, precise calculations for transition energies and probabilities are presented, using state-of-the-art numerical methods. QED corrections, hyperfine interactions, and the interaction with atomic electrons were evaluated and finite nuclear size effects were incorporated non-perturbatively. Furthermore, new methods for the calculation of higher-order corrections for the hyperfine structure are presented, including a complete calculation of the second-order hyperfine structure and leading-order vacuum polarization corrections for extended electric quadrupole distributions inside the nucleus. In connection with recent x-ray spectroscopic measurements on muonic atoms, the nuclear quadrupole moment of $^{185}_{75}$Re and $^{187}_{75}$Re is extracted. The second part of this thesis is about the g factor of a bound electron and its dependence on the shape of the nuclear charge distribution. A numerical, non-perturbative approach for the calculation of the corresponding nuclear shape correction is presented and implications for the uncertainties of theoretical predictions are discussed. In particular, the model-uncertainty of the finite-nuclear-size correction to the g factor can be reduced due to the more realistic model of the nuclear charge distribution. Finally, calculations of finite-size and vacuum-polarization corrections to the g factor of a muon bound to a $^4_2$He nucleus significantly contribute to the theoretical prediction on the 10^{-9} uncertainty level. As shown in an earlier work, an experimental value of the same accuracy could give access to an improved value of the muon's mass or magnetic moment anomaly.

The following articles covered by this thesis have been published in peer-reviewed journals or have been submitted for publication:

- Niklas Michel, Natalia S. Oreshkina, Christoph H. Keitel
  Theoretical prediction of the fine and hyperfine structure of heavy muonic atoms
  Phys. Rev. A. **96**, 032510 (2017) (Ref. [1])

- Bastian Sikora, Halil Cakir, Niklas Michel, Vincent Debierre, Natalia S. Oreshkina, Nikolay A. Belov, Vladimir A. Yerokhin, Christoph H. Keitel, Zoltán Harman
  Improving the accuracy of the muon mass and magnetic moment anomaly via the bound-muon g factor
  Phys. Rev. D. **97**, 111301(R) (2018) (Ref. [2])

- Niklas Michel, Natalia S. Oreshkina
  Higher-order corrections for the dynamic hyperfine structure of muonic atoms
  submitted, arXiv:1809.06623 (2018) (Ref. [3])

- Niklas Michel, Jacek Zatorski, Natalia S. Oreshkina, Christoph H. Keitel
  Non-perturbative analysis of nuclear shape effects on the bound electron g factor
  submitted, arXiv:1806.00405 (2018) (Ref. [4])

The following article is in preparation:

- A. Adamczak, A. Antognini, K. Kirch., N. Ritjoho, A. Skawaran, N. Berger, R. Pohl, F. Wauters, T. E. Cocolios, N. Seveijns, R. Dressler, R. Eichler, A. Knecht, A. Papa, E. Rapisarda, P. Indelicato, K. Jungmann, L. Willmann, N. Michel, N. S. Oreshkina, C. H. Keitel, M. Pospelov, P. Reiter, S. Roccia
  On the analysis of the hyperfine splitting in muonic spectra: Re-185 and Re-187
  in preparation (Ref. [5])

The following article not covered by this thesis has been published:

- Natalia S. Oreshkina, Stefano M. Cavaletto, Niklas Michel, Zoltán Harman, Christoph H. Keitel
  Hyperfine splitting in simple ions for the search of the variation of fundamental constants
  Phys. Rev. A. **96**, 030501(R) (2017) (Ref. [6])

The following contribution to a conference proceeding will be published:

- Z. Harman, B. Sikora, V. A. Yerokhin, H. Cakir, V. Debierre, N. Michel, N. S. Oreshkina, N. A. Belov, J. Zatorski, and C. H. Keitel
  The g factor of highly charged ions
  accepted in Journal of Physics: Conference Series

Contents

4 Bound muon g factor in $^{4}_{2}$He   **89**

Summary & Outlook   **93**

A Appendix   **97**

Bibliography   **109**

Acknowledgements   **127**

Introduction

Advances in spectroscopy have always given new insights into the physical laws which govern our world at the smallest scales. The first observation of a discrete absorption spectrum was due to Wollaston in 1802 [7] and Fraunhofer in 1814 [8], who discovered the Fraunhofer lines in the solar spectrum independently from each other. In the following decades, the emission spectra of different elements were explored. Especially noteworthy are the systematic investigations by Kirchhoff and Bunsen in Heidelberg [9, 10]. It became apparent that elements can be identified by their characteristic spectrum and that laboratory emission spectra are connected to astrophysical absorption spectra [11].

Since the hydrogen atom consists of only one electron bound to a single proton, it has the simplest spectrum among all atoms and therefore was particularly important for the development of theoretical models. It was recognized by Balmer in 1885 [12] that the position of spectral lines as measured by Ångström [13], Huggins [14], and Vogel [15] could be described with surprising accuracy by a simple formula. This was generalized later in terms of the Rydberg formula [16, 17]. It describes the Balmer series as a special case and also predicts the Lyman, Paschen, Brackett, Pfund, and Humphreys series, which were confirmed subsequently by experiments [18–22]. However, the Rydberg formula is purely empirical, without an underlying theoretical framework.

Additionally, the electron was discovered by the investigation of cathode rays [23, 24], and Rutherford scattering showed that the positive charge and almost the entire mass of an atom is concentrated in its center in form of an atomic nucleus [25]. Also, the spectral density of black-body radiation was explained by Planck using the quantum hypothesis [26]. This motivated the Bohr model of the atom [27], according to which the electron can revolve around the nucleus only on certain quantized orbits. Compared to the previous Thomson [28] and Rutherford model, now the Rydberg formula and thereby the hydrogen spectrum could be derived, and the discrete energies could be expressed in terms of the fine-structure constant α, the electron mass m_e, and the speed of light c_0. The relativistic extension of this model is the Bohr-Sommerfeld model [29], which explains also finer features of the hydrogen spectrum. However, despite the success of describing the quantized energies, the Bohr-Sommerfeld model has difficulties with the generalization to many-electron systems. A consistent theoretical framework for non-relativistic atomic theory, also for more complicated atoms, was finally obtained with the Schrödinger equation [30–33] and matrix mechanics [34–36], which were shown to be equivalent formulations of quantum theory [37].

Due to the Zeeman effect [38], spectral lines of atoms exposed to an external magnetic field are split into sublevels. This could only be explained consistently by assigning, besides the orbital angular momentum, also the spin angular momentum to the electron [39]. The Dirac equation [40] incorporates the electron's spin naturally and predicts that the corresponding magnetic moment due to spin is twice as large as the orbital

angular momentum. Additionally, Dirac's equation obeys the laws of special relativity, and among its solutions negative energy states occur, which led to the prediction of the positron, the electron's antiparticle. The negative-energy states also lead to problems with the one-particle interpretation of the Dirac equation due to phenomena such as the instability of the hydrogen ground state, Zitterbewegung, and Klein's paradox [41].

Two experimental results pointed out that the Dirac equation, despite its success in describing the energy levels of the hydrogen atom, could not be the end of the story for the theory of atomic structure. The Dirac equation for a point-like nucleus predicts that two energy levels with the same principal quantum number and total angular momentum are degenerate [42]. Therefore, the $2s_{1/2}$ and $2p_{1/2}$ levels should be degenerate according to Dirac's theory. However, Lamb and Retherford showed for hydrogen that these levels are separated by about $1060\,\text{MHz}$ by driving the transition directly with radio waves [43]. On the other hand, anomalies in the magnetic hyperfine structure of hydrogen and deuterium [44] as well as sodium and gallium [45, 46] were revealed. Both phenomena were explained in the framework of quantum electrodynamics (QED) [47], which yields small corrections to the energy levels in atoms and to the magnetic moment of the electron. To this date, the comparison of experiment and theory for the hyperfine and Zeeman splitting in simple atomic systems keeps challenging QED and delivering values for fundamental physical constants [48]. The following two sections describe more recent developments in this field.

Muonic atoms

For further studies of H-like systems, either the atomic nucleus or the bound electron can be exchanged with another charged particle. This establishes the field of research on *exotic atoms*. Depending on the type of considered particles, nuclear structure effects can either be avoided or enhanced. Bound states between two leptons are not affected by the strong interaction or nuclear effects and are therefore suitable for tests of bound-state QED in a cleaner environment. One example is positronium [49], a system formed by an electron and its antiparticle, the positron. The energy levels were studied up to order α^6 in Refs. [50–53] and measured on a 10^{-4} up to 10^{-9} level, e.g. in Refs. [54–58], despite a lifetime in the range of 10^{-9}s due to pair annihilation. Another interesting leptonic system is *muonium* [59], a bound state consisting of an antimuon and an electron. The antimuon is the positively charged lepton in the second generation of matter in the Standard Model of particle physics and the muon the negatively charged one. Since the mass ratio of muon and proton is $m_p/m_\mu \approx 8.9$, the spectrum of muonium is quite similar to that of hydrogen, except that effects due to proton structure are avoided. The hyperfine splitting in muonium was measured to a part-per-billion level in Refs. [60, 61] and calculated with a similar accuracy in Refs. [62–66]. The *MuSEUM* collaboration [67] plans new precision experiments on the hyperfine structure in muonium. The muon-antimuon bound state is called *true muonium* [68], or *dimuonium*. It has yet to be observed, which is the aim of the $\mu\mu$-tron collider, which is constructed at the Budker Institute of Nuclear Physics (Russia) [69]. A similar bound state exists in principle also for third-generation of matter, a tau-antitau bound state called *true tauonium*. However, due to the extremely short lifetime of tau leptons, it would be even more difficult to

observe [68].

The negatively charged muon can also form bound states with atomic nuclei. These exotic atoms are commonly referred to as *muonic atoms*. In this case, the nuclear structure effects are greatly enhanced for the following reason: The muon is about 207 times heavier than the electron. Therefore, the Bohr radius of the muonic orbitals, which is an estimate for the distance between bound particle and nucleus, is also 207 times smaller. As a consequence, especially for high Z, the bound-muon wave function has a large overlap with the nuclear charge distribution, which results in remarkable interplays between atomic and nuclear physics. Observation of x-rays from bound-bound transitions in muonic atoms was reported for the first time in Ref. [70] in cosmic ray studies, and in Ref. [71] with a laboratory muon beam. The beginning of muonic atom theory is marked by the seminal paper by Wheeler [72]. Since then, the spectra of muonic atoms have been investigated in numerous experiments, e.g. [73–81]. In particular, absolute RMS charge radii of atomic nuclei were obtained by analysis of muonic x-ray spectra for the majority of stable nuclei [82]. An overview over the progress in theoretical calculations can be found in Refs. [83–85]. In the past, the codes `MUON` and `RURP` [86] based on simple solutions of the Dirac equations and developed in the 1970s have been used frequently for the comparison of theoretical predictions and measurements of muonic x-rays.

Muonic hydrogen came to attention recently because laser spectroscopy of a $2p \rightarrow 2s$ transition enabled the extraction of the proton charge radius as $r_p^{(\mu)} = 0.84184(67)\,\text{fm}$, and the result turned out to be smaller than the CODATA value $0.8768(69)\,\text{fm}$ at the time by 5.0 standard deviations [87]. In 2013, a new measurement increased the deviation to 7 standard deviations [88]. Measurements on muonic deuterium confirmed these results [89] for the deuterium charge radius and lately, also an experiment with atomic hydrogen measured the small proton radius [90]. Results from elastic electron-proton scattering, which are also used for the CODATA value [91], seem to confirm the larger value for the proton radius, but the proton-radius extraction from scattering data is not unambiguous [92]. However, a new result from atomic hydrogen spectroscopy resulted in the larger value again [93], thus this *proton radius puzzle* is not resolved until now. Together with anomalies on the magnetic moment of the muon [94], this motivates further investigation of muonic systems.

In the high-Z regime, the MuX collaboration at the Paul Scherrer Institut (Switzerland) has recently started to revive x-ray spectroscopy of muonic atoms after these kind of measurements have not been performed for nearly thirty years. The aim is to measure muonic x-ray spectra for the heaviest and also radioactive nuclei, for example $^{226}_{88}\text{Ra}$ and $^{248}_{96}\text{Cm}$, and to extract information on nuclear parameters.

The *g* factor of the bound electron

The magnetic moment of the electron is commonly expressed by the dimensionless gyromagnetic factor, or g factor, which is the proportionality constant between magnetic moment and angular momentum. Experiments on the g factor of the free electron provide one of the most stringent tests of QED without a strong external electromagnetic field. It was measured with an uncertainty below the part-per-trillion level [95, 96] and predicted to order α^5 theoretically, e.g. [47, 97–104]. A combination of experiment and

theory has allowed the extraction of the fine-structure constant α on the parts-per-billion level [105, 106].

The g factor can also be measured and theoretically calculated to an extraordinary precision in case of the electron bound in a highly charged ion. Here, QED can be tested in the regime of strong fields, since the electron is exposed to the nuclear Coulomb potential. It has been measured for H-like $^{12}_{6}\text{C}^{5+}$ [107, 108], $^{16}_{8}\text{O}^{7+}$ [109], and $^{28}_{14}\text{Si}^{13+}$ [110], and for Li-like $^{28}_{14}\text{Si}^{11+}$ [111], $^{40}_{20}\text{Ca}^{17+}$ [112], and $^{48}_{20}\text{Ca}^{17+}$ [112] on the part-per-billion level with Penning trap experiments performed in Mainz (Germany) using a single trapped ion. A Penning trap is a device for trapping charged particles with a combination of a static electric quadrupole field and a homogeneous magnetic field [113, 114].

Two developing experiments aim at measuring the bound-electron g factor in H-like ions also for very high charge numbers. The *ALPHATRAP* experiment [115] uses a measurement scheme with two Penning traps similar to the *Mainz g-Factor Experiment.* Now, the ions are not created *in situ* but can be injected from external sources, like the *Heidelberg EBIT* (electron-beam ion trap) [116]. In this way, g factors of ions up to H-like $^{208}_{82}\text{Pb}^{81+}$ can be investigated with an expected accuracy of 10 parts-per-trillion [115]. The *ARTEMIS* experiment at the GSI Darmstadt (Germany) [115, 117] will investigate the structure of Zeeman sublevels in highly charged ions. In this way, ground- and excited-state g factors can be accessed. With connection to the *HITRAP* beamline, the heaviest hydrogen-like ions, e.g. $^{238}_{92}\text{U}^{91+}$, will be available [118].

The precision experiments on the bound-electron g factor demand theoretical calculations on a competing level of accuracy. The interaction of a bound electron with the atomic nucleus is characterized by the parameter $Z\alpha$, where Z is the nuclear charge number and $\alpha \approx 1/137$. For light nuclei, $Z\alpha$ is a small parameter and corrections to the binding energies can be calculated by a perturbative expansion in this parameters. On the other hand, for heavy nuclei, $Z\alpha$ is on the order of unity, and a power series expansion of energy corrections in $Z\alpha$ is not always viable. The leading contribution to the binding corrections to the bound-electron g factor is due to the point-like Coulomb potential and has been obtained by Breit [119]. The one- and two-loop vacuum-polarization (VP) and self-energy (SE) corrections have been calculated to order $(Z\alpha)^4$ in Refs. [120–124]. Two-loop corrections to order $(Z\alpha)^5$ have been recently presented in Ref. [125]. One-loop QED corrections for the VP and SE to all orders in $Z\alpha$ has been calculated in Refs. [126–134]. Two-loop calculations to all orders in $Z\alpha$ have not been completed to date. They have been presented for two VP loops and for the mixed VP-SE effect in Ref. [135], and for the SE loop-after-loop terms in Ref. [136].

Furthermore, nuclear effects beyond those due to the point-like Coulomb potential have to be considered. Although the nucleus is much smaller than the typical extent of the electron wave function, it is an extended object and, correspondingly, the Coulomb potential is modified at small distances. This causes the finite nuclear size correction to the energy levels and to the g factor of the bound electron. A relativistic analytic formula for this effect has been given in Ref. [137] and the corresponding non-relativistic limit in Ref. [120]. In case of two-photon exchanges between the bound electron and internal nuclear currents, also excited nuclear states contribute, leading to the nuclear polarization correction. This has been considered in Refs. [138, 139]. The calculation of all effects mentioned so far assumed an infinitely heavy resting nucleus. The nuclear

recoil corrections account for the finite nuclear mass. Here, besides α for QED loops and $Z\alpha$ for interactions with the nuclear potential, an additional expansion parameter m_e/M appears, which is the electron-to-nucleus mass ratio. To order $\alpha(Z\alpha)^2(m_e/M)^2$, results can be found in Refs. [140] and to all orders in m_e/M and first order in $Z\alpha$ in Ref. [141]. Suitable for heavy ions, the recoil correction to first order in m_e/M, but to all orders in $Z\alpha$, is given in Refs. [142, 143]. In Ref. [144], the nuclear shape effect, also called nuclear deformation effect, was introduced for spinless nuclei, which takes the deformation, i.e. the deviation from a perfect spherically symmetric shape of the nuclear charge distribution into account. This contribution is not significant for light nuclei at the current level of experimental accuracy. However, it scales strongly with the nuclear charge and therefore becomes important for high Z.

The combination of theory and experiment for the bound-electron g factor in $^{12}_{6}\text{C}^{5+}$ provided an improved value of the electron mass [108, 145, 146]. For $^{28}_{14}\text{Si}^{13+}$ [110], it was shown as a proof-of-principle determination that nuclear parameters like the RMS charge radius can be obtained. Also, the extraction of nuclear magnetic moments was suggested theoretically [147, 148]. Furthermore, it was argued that an independent and more accurate value for the fine-structure constant can be obtained [149–151]. With upcoming experiments in the high-Z regime, further tests of QED in strong fields, new information on nuclear parameters, and the extraction of fundamental constants can be expected, and improved theoretical calculations especially for heavy nuclei are needed.

The subject of this thesis

This thesis presents calculations of spectra of muonic atoms with new methods for predicting higher order effects and up-to-date numerical schemes. The calculation of transition energies and transition probabilities in heavy muonic atoms is necessary for the comparison with the above-mentioned recent experiments by the MuX collaboration and the extraction of nuclear parameters.

In muonic atoms, the connection between measured spectra and nuclear parameters is obscured due to the highly complicated level structure. Complex computations need to be performed for the generation of the spectrum for a given nuclear charge distribution. Conversely, the theoretically calculated spectrum can be matched to the experimentally measured one by adjustment of the nuclear parameters in the computations. In this way, nuclear parameters can be extracted. Correspondingly, for the fitting process, all theoretical calculations need to be unified in one single approach. During the last years, the dual-kinetic-balance (DKB) method [152] has proved to be a very successful numerical approach in relativistic atomic structure calculations, but has not been used to date for muonic atoms. In this thesis, the DKB method based on B-spline representations of wave functions is used to calculate the energy levels of the bound muon in the electric field of heavy nuclei, where contributions due to the finite nuclear size, QED corrections, hyperfine interactions, and electron screening are readily included. With the DKB method, a direct numerical evaluation of second-order energy corrections is possible by a summation over the complete spectrum of the bound muon. This is demonstrated in the thesis with the second-order electric quadrupole interaction and it is shown that this contribution is important in experiments with very heavy nuclei.

The vacuum polarization (VP) correction due to a virtual electron-positron pair gives a sizable correction to energy levels in muonic atoms. This correction also affects electric multipole operators, in particular, the electric quadrupole interaction. In this thesis, it is shown how matrix elements of multipole potentials of any order due to an arbitrary deformed nuclear charge distribution can be systematically corrected for the leading-order VP. For the quadrupole interaction, analytical expressions in terms of special functions have been derived. Numerical studies for uranium and rhenium are presented in this thesis.

The calculations are compared to measurements of spectra of isotopically pure muonic rhenium, which were recorded in 2016 at the Paul Scherrer Institute (Switzerland). A comparison of theory and experiment enabled the extraction of the nuclear quadrupole moment. In this thesis, a fitting procedure with the consideration of effects non-linear in the quadrupole moment is constructed. With planned measurements on elements as heavy as $^{248}_{96}$Cm in the near future, extraction of further nuclear parameters with this approach can be expected.

In addition, nuclear effects on the bound electron g factor were considered in this thesis. To date, the nuclear deformation correction was calculated with perturbative methods only. This thesis contributes to the theory landscape by investigating the nuclear deformation correction non-perturbatively with advanced numerical methods. It is shown that the perturbative approach overestimated the nuclear deformation effect by about 20% and the reason for the difference is analyzed.

Furthermore, in this thesis the finite nuclear size effect and several one- and two-loop QED corrections for the bound-muon g factor in helium are calculated, namely, the all-order Uehling and the Källén-Sabry terms. Together with calculations of further contributions by other authors, this enabled a theoretical prediction of the g factor on a 10^{-9} level. As shown in Ref. [2], this can potentially give access to an improved determination of the muon's mass or magnetic moment anomaly, provided that a measurement of similar accuracy could be performed.

The structure of the thesis

This thesis is organized in the following way:
Chapter 1 gives an introduction to the framework of bound-state QED. The Dirac equation is discussed, and analytical and numerical solutions for nuclear potentials and vacuum polarization potentials are given.
In Chapter 2, the energy levels and transition probabilities of muonic atoms are obtained. An improved numerical spectrum generator for the extraction of nuclear parameters is presented in Section 2.1, as well as new methods and calculations for vacuum polarization and higher-order hyperfine splitting effects in Section 2.2.
Then, in connection with measurements on isotopically pure muonic rhenium, the nuclear spectroscopic quadrupole moment is extracted in Section 2.3.
In Chapter 3, the nuclear finite size and deformation corrections to the bound-electron g factor are examined. A numerical method for their precise calculation is introduced and

results are compared to previous studies.

For muonic helium, the high-precision calculations of the finite nuclear-size and one- and two-loop vacuum-polarization corrections are described in Chapter 4.

Finally, the main findings of the thesis are summarized and an outlook is given.

System of units and physical constants

Relativistic natural units are used in this thesis, where $\hbar = c_0 = 1$, where $\hbar$ is the reduced Planck's constant, and c_0 is the speed of light in vacuum. In Chapter 2, relativistic muonic natural units are used, where additionally the mass of the muon m_μ is set to unity. For example, the electron mass in this system of units has the numerical value of the mass ratio $m_e/m_\mu = 1/206.768\,282\,6$ [91]. Furthermore, Lorentz-Heavyside units of electromagnetism are used, corresponding to $\epsilon_0 = \mu_0 = 1$, where ϵ_0 is the vacuum permittivity and μ_0 the vacuum permeability. The following table gives an overview of the SI-values of the basis units and derived quantities in muonic natural units.

Overview of the SI-values of the base units and important derived units for the muonic natural units. SI Values for $\hbar$, c, m_μ, ϵ_0, μ_0 are taken from [91].

base units:		
Planck's constant	$\hbar$	$1.054\,571\,800 \times 10^{-34}\,\mathrm{kg\,m^2 s^{-1}}$
speed of light	c_0	$299\,792\,458 \quad \mathrm{m\,s^{-1}}$
muon mass	m_μ	$1.883\,531\,594 \times 10^{-28}\,\mathrm{kg}$
vacuum permittivity	ϵ_0	$8.854\,187\,817 \times 10^{-12}\,\mathrm{kg^{-1}m^{-3}s^4 A^2}$
vacuum permeability	μ_0	$12.566\,370\,614 \times 10^{-7}\ \mathrm{kg\,m\,s^{-2}A^{-2}}$
derived units:		
distance	$\hbar/(m_\mu c_0)$	$1.867\,594\,31 \times 10^{-15}\,\mathrm{m}$
time	$\hbar/(m_\mu c_0^2)$	$6.229\,624\,05 \times 10^{-24}\,\mathrm{s}$
energy	$m_\mu c_0^2$	$1.692\,833\,77 \times 10^{-11}\,\mathrm{kg\,m^2 s^{-2}}$

Chapter 1

Bound state quantum electrodynamics in the Furry picture

In this thesis, relativistic atomic structure calculations are performed in order to investigate nuclear effects on the energy levels of electrons or muons bound in the potential of an atomic nucleus. In this chapter, as an introduction, the starting point is the Lagrangian of quantum electrodynamics (QED) and results will be derived from there. This includes the derivation of the Dirac equation as the zero-order solution and the study of radiative corrections due to virtual particles. The leading-order vacuum polarization corrections, and their inclusion as potentials in the Dirac equation, are discussed. Finally, the analytical solution of the Dirac equation for the relativistic Coulomb problem is presented, as well as numerical solutions for arbitrary nuclear potentials.

1.1 The external field approximation

The correct prediction of the fine structure of the hydrogen atom was a huge success of the Dirac equation [40]. Originally intended to be a relativistic generalization of the Schrödinger equation, it was a one-particle equation for a wave function. However, a relativistic quantum theory always has to be a many-body theory, since for high energies effects like pair creation have to be considered. The relativistic quantum field theory which describes the electromagnetic interaction is QED. In this framework, the bound state energies of atomic systems can be obtained including radiative corrections due to the quantized photon field and virtual particle-antiparticle pairs.

In this thesis, hydrogen-like systems and heavy nuclei are considered, so a single fermion (electron or muon) bound to a nucleus with a high charge number Z. The interaction strength of electron and nucleus is characterized by the parameter $Z\alpha$, where $\alpha \approx 1/137$ is the fine-structure constant. For high Z, this parameter is not small and as a result the Coulomb interaction between a fermion and the nucleus cannot be treated in perturbation theory effectively. For heavy nuclei, the fermion-nucleus mass ratio m_f/M is small. Accordingly, the external field approximation [153, Section 13.6] $m_f/M \to 0$ can be used, which is also called the Furry picture of QED [154]. Here, recoil effects are neglected and the nucleus is considered as the source of a classical electromagnetic field, to which the bound fermion is exposed.

The starting point of the derivations in this chapter is the QED Lagrangian

$$
\begin{aligned}
\mathcal{L}_{\text{QED}} &:= \mathcal{L}_{\text{free}}^{\text{D}} + \mathcal{L}_{\text{free}}^{\text{E.M.}} + \mathcal{L}_{\text{int}}, \\
\mathcal{L}_{\text{free}}^{\text{D}} &:= \bar{\psi}\left(i\gamma^\mu \partial_\mu - m_f\right)\psi, \\
\mathcal{L}_{\text{free}}^{\text{E.M.}} &:= -\frac{1}{4}F_{\mu\nu}F^{\mu\nu}, \\
\mathcal{L}_{\text{int}} &:= -e\bar{\psi}\gamma^\mu\psi A_\mu,
\end{aligned}
\tag{1.1}
$$

which is the sum of free Dirac, free electromagnetic and interaction Lagrangians. Here, ψ is the fermion field operator, $F_{\mu\nu} = \partial_\mu A_\nu - \partial_\nu A_\mu$ the field strength tensor of the electromagnetic four-potential A_μ. Detailed introductions to QED starting from this Lagrangian can be found in several excellent textbooks, e.g. [153, 155, 156], thus the focus of this section is on the external field approximation and extraction of bound state energies. The counter terms are not included, so the derivations here should be understood on a formal level, for calculations including the counterterms and renormalization, see for example Ref. [153, Section 14], or Ref. [157].

In the external field approximation, the electromagnetic four-potential is written as

$$
A_\mu(x) = \mathcal{A}_\mu(x) + \hat{A}_\mu(x),
$$

where $\mathcal{A}_\mu(x)$ is the classical four-potential, caused by the nuclear charge and current distribution and $\hat{A}_\mu(x)$ is the quantized field describing quantum fluctuations. Correspondingly, the interaction part in Eq. (1.1) can be written as

$$
\mathcal{L}_{\text{int}} = -e\bar{\psi}\gamma^\mu\psi\mathcal{A}_\mu - e\bar{\psi}\gamma^\mu\psi\hat{A}_\mu =: \mathcal{L}_{\text{int}}^{\text{C}} + \mathcal{L}_{\text{int}}^{\text{Q}}.
\tag{1.2}
$$

For hydrogen-like systems, bound state energies can be extracted from the poles of the fermion propagator. In the following, it will be demonstrated how the poles of the propagator in the interacting theory can be obtained by perturbation theory in powers of the fine-structure constant α, including the interaction with the classical field to all orders. For this purpose, full propagator is connected to the propagator in the external classical field and to the propagator of the free theory.

Propagator in the free Dirac theory

As a start, the Lagrangian of the free Dirac theory $\mathcal{L}_{\text{free}}^{\text{D}}$ from Eq. (1.1) is considered. The Euler-Lagrange equations result in the Dirac equation as the equation of motion for the quantum field as

$$
\left(i\gamma^\mu\partial_\mu - m_f\right)\psi(x) = 0.
\tag{1.3}
$$

The solution of Eq. (1.3) can be written as a superposition of plane-wave solutions [156, Sec. 3.3.] as

$$\psi(x) = \int \frac{d^3p}{(2\pi)^3} \frac{1}{\sqrt{2E_\mathbf{p}}} \sum_{s=1}^{2} \left(a_\mathbf{p}^s u^{(s)}(p) \mathrm{e}^{-ip\cdot x} + b_\mathbf{p}^{s\,\dagger} v^{(s)}(p) \mathrm{e}^{ip\cdot x} \right),$$

$$\bar{\psi}(x) = \int \frac{d^3p}{(2\pi)^3} \frac{1}{\sqrt{2E_\mathbf{p}}} \sum_{s=1}^{2} \left(b_\mathbf{p}^s \bar{v}^{(s)}(p) \mathrm{e}^{-ip\cdot x} + a_\mathbf{p}^{s\,\dagger} \bar{u}^{(s)}(p) \mathrm{e}^{ip\cdot x} \right),$$

where the plane wave solutions read

$$u^{(1,2)}(p) = \begin{pmatrix} \sqrt{p\cdot\sigma}\,\xi_{(1,2)} \\ \sqrt{p\cdot\bar{\sigma}}\,\xi_{(1,2)} \end{pmatrix}, \ v^{(1,2)}(p) = \begin{pmatrix} \sqrt{p\cdot\sigma}\,\xi_{(1,2)} \\ -\sqrt{p\cdot\bar{\sigma}}\,\xi_{(1,2)} \end{pmatrix}, \ \text{with } \xi_1 = \begin{pmatrix} 1 \\ 0 \end{pmatrix}, \ \xi_2 = \begin{pmatrix} 0 \\ 1 \end{pmatrix}.$$

The operators $a_\mathbf{p}^s$, $b_\mathbf{p}^s$ satisfy the anticommutation relations

$$\left\{ a_\mathbf{p}^r, a_\mathbf{q}^{s\,\dagger} \right\} = \left\{ b_\mathbf{p}^r, b_\mathbf{q}^{s\,\dagger} \right\} = (2\pi)^3 \delta(\mathbf{p} - \mathbf{q}) \delta_{rs},$$

and zero otherwise. The vacuum state of the theory is defined as the state destroyed by the annihilation operators as

$$a_\mathbf{p}^s \left| 0 \right\rangle = b_\mathbf{p}^s \left| 0 \right\rangle = 0,$$

while the one-particle fermion and anti-fermion states are created from the vacuum as

$$\left| \mathbf{p}, s \right\rangle = \sqrt{2E_\mathbf{p}}\, a^{s\,\dagger} \left| 0 \right\rangle,$$

$$\left| \mathbf{q}, r \right\rangle = \sqrt{2E_\mathbf{q}}\, b^{r\,\dagger} \left| 0 \right\rangle.$$

Now, the Feynman propagator is defined as the vacuum expectation value of the time-ordered product [156, Section 3.5.] and reads

$$S_F(x - y) := \left\langle 0 \right| T \psi(x) \bar{\psi}(x) \left| 0 \right\rangle = \int \frac{\mathrm{d}^4 p}{(2\pi)^4} \frac{(\gamma^\mu p_\mu + m_f)}{p^2 - m_f^2 + i\epsilon} \mathrm{e}^{-ip\cdot(x-y)}. \tag{1.4}$$

The Feynman propagator is a Green's function of the Dirac equation (1.3), thus

$$\left(i\gamma^\mu \partial_\mu - m_f \right) S_F(x - y) = \delta(x - y). \tag{1.5}$$

Propagator in the external field

As a next step, we will consider the sum $\mathcal{L}_\mathrm{free}^\mathrm{D} + \mathcal{L}_\mathrm{int}^\mathrm{C}$ of free Dirac Lagrangian and the interaction with the classical external field from Eq. (1.2). In the following, it is assumed that the external field is independent of time. The equations of motion for the fermion field are

$$\left(i\gamma^\mu \partial_\mu - m_f - e\gamma^\mu \mathcal{A}_\mu \right) \psi(x) = 0,$$

which simply is the Dirac equation in an external field. However, this is still an equation for the quantum field. The corresponding equation for the classical Dirac field is obtained by using a complete set of states $|n\rangle$ with energies E_n, where $|0\rangle$ is the vacuum state, and define the Dirac wave functions as matrix elements of the fermion field operator [153, Section 14.1] as

$$
\begin{aligned}
u_n(x) &= u_n(\mathbf{x})\, e^{-iE_n^{(1)}t} := \langle 0|\, \psi(x)\, |n\rangle \\
v_k(x) &= v_k(\mathbf{x})\, e^{+iE_k^{(2)}t} := \langle n|\, \psi(x)\, |0\rangle \,,
\end{aligned}
\tag{1.6}
$$

where the first equality follows from time translation invariance, and is only valid in static background fields. Then, it can be shown from the anti-commutation relations of the field operator that the wave functions fulfill the completeness relation

$$
\sum_n u_n(\mathbf{x})u_n^\dagger(\mathbf{y}) + \sum_k v_k(\mathbf{x})v_k^\dagger(\mathbf{y}) = \delta(\mathbf{x} - \mathbf{y}),
$$

and that both $u_n(\mathbf{x})$ and $v_k(\mathbf{x})$ satisfy the Dirac equation, now for wave functions:

$$
\begin{aligned}
\left(i\boldsymbol{\alpha}\cdot\nabla + \beta m_f + e\mathcal{A}^0 - e\boldsymbol{\alpha}\cdot\boldsymbol{\mathcal{A}}\right)u_n(\mathbf{x}) &= E_n^{(1)}u_n(\mathbf{x}) \\
\left(i\boldsymbol{\alpha}\cdot\nabla + \beta m_f + e\mathcal{A}^0 - e\boldsymbol{\alpha}\cdot\boldsymbol{\mathcal{A}}\right)v_k(\mathbf{x}) &= -E_k^{(2)}v_k(\mathbf{x})
\end{aligned}
\tag{1.7}
$$

The propagator in the external field is defined, similarly to Eq. (1.4), as the vacuum expectation value of time-ordered product

$$
S_{\mathcal{A}}(x,y) := \langle 0_{\mathcal{A}}|\, T\psi(x)\bar{\psi}(x)\, |0_{\mathcal{A}}\rangle \,,
\tag{1.8}
$$

where $|0_{\mathcal{A}}\rangle$ denotes the vacuum state in the external field. It is a Green's function of the equation of motion of the fermion field operator, analogously to Eq. (1.5):

$$
(i\gamma^\mu\partial_\mu - m_f - e\gamma^\mu\mathcal{A}_\mu(x))\, S_{\mathcal{A}}(x,y) = \delta(x - y).
\tag{1.9}
$$

Since the external field breaks translation invariance, the propagator in the external field now depends on the spacial components of x and y separately, and not only on the difference $(x - y)$. Radiative corrections in the Furry picture can be calculated by using the usual Feynman rules and the dressed propagator instead of the free propagator, as well as solutions of the Dirac equation including the external field for the in and out states. Combining Eq. (1.5) with Eq. (1.9) gives a relation between the propagators of the free theory and in the external field [155, Section 2.5.], which can be solved iteratively,
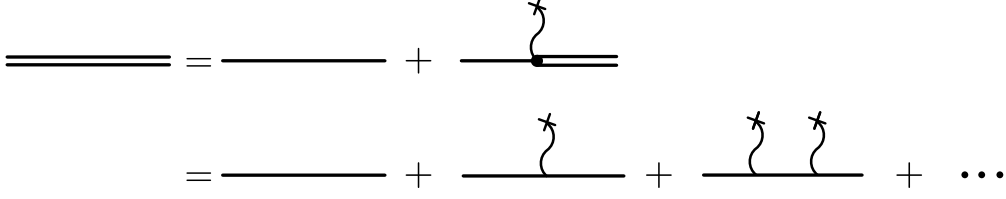
Figure 1.1: Relation between the propagator including the external field and the propagator of the free theory in Feynman diagrams corresponding to Eq. (1.10). A double line corresponds to the dressed propagator in the external field, a single line to the free Dirac propagator, and a wave line with a cross to the interaction with the external field. The propagator in the external field is obtained by including all interactions with the external field in the free propagator.

as

$$
\begin{aligned}
S_{\mathcal{A}}(x,y) = \ & S_F(x-y) + \int \mathrm{d}x \ S_F(x-z)\left(-e\gamma^\mu \mathcal{A}_\mu(z)\right) S_{\mathcal{A}}(z,y) \\
= \ & S_F(x-y) + \int \mathrm{d}z \ S_F(x-z)(-e\gamma^\mu \mathcal{A}_\mu(z)) S_F(z-y) \\
& + \iint \mathrm{d}z_1 \mathrm{d}z_2 \ S_F(x-z_1)(-e\gamma^\mu \mathcal{A}_\mu(z_1)) S_F(z_1-z_2)(-e\gamma^\mu \mathcal{A}_\mu(z_2)) S_F(z_2-y)
\end{aligned}
$$

$$
+ \dots . \tag{1.10}
$$

As demonstrated in Fig. 1.1, this gives an intuitive picture of the dressed propagator: Propagation in the external field corresponds to free propagation with all possible interactions with the external field included. Another useful form of the propagator in the external field is the spectral representation in terms of the Dirac wave functions (1.6). By inserting a complete set of states in Eq. (1.8), one obtains

$$
S_{\mathcal{A}}(x,y) = \Theta(x^0 - y^0) \sum_n u_n(x)\bar{u}_n(y) - \Theta(y^0 - x^0) \sum_k v_k(x)\bar{v}_k(y).
$$

For a time-independent external field, a Fourier transformation in the zeroth component yields

$$
\tilde{S}(\mathbf{x},\mathbf{y},E) = \sum_n \frac{u_n(\mathbf{x})\bar{u}_n(\mathbf{y})}{E_n^{(1)} - E - i\,\epsilon} - \sum_k \frac{v_k(\mathbf{x})\bar{v}_k(\mathbf{y})}{E_k^{(2)} + E - i\,\epsilon}. \tag{1.11}
$$

Therefore, bound states due to the external field lead to additional isolated poles in the propagator.

Propagator of interacting theory

Finally, we will consider the propagator in the interacting theory, including the interaction with the quantized photon field. A similar argument as in the derivation of Eq. (1.11) also holds for the interacting theory [153, Section 14.2.]. That is, bound state energies including all radiative corrections appear as isolated poles of the full propagator. In order to
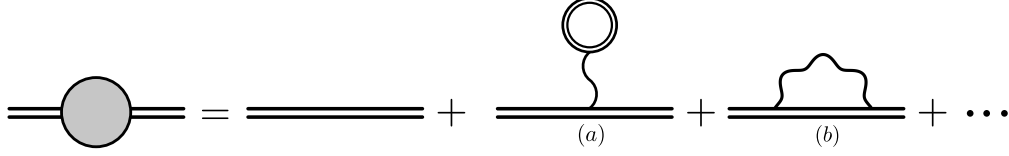
Figure 1.2: Perturbative expansion of the propagator of the interacting theory in powers of the fine-structure constant α. The zero-order contribution is the propagator in the external field. To first order in α, the contributions are the vacuum-polarization diagramm (a) and the self-energy diagram (b).

locate the positions of these poles, perturbation theory with the propagator including the external field is used, expanding the propagator in powers of the fine-structure constant α. The zero-order term is the dressed propagator in the background field, corresponding to solving the Dirac equation with the background field. The diagrams contributing to the radiative corrections to first order in α are the vacuum-polarization (VP) and self-energy (SE) diagrams, which are shown in Fig. 1.2 (a) and (b), respectively. Using the Feynman rules [155, Section 6.1.], the propagator of the interacting theory $S_I(x,y)$ is expanded to first order in α as

$$S_I(x,y) \quad \approx S_{\mathcal{A}}(x,y) + \int \mathrm{d}^4 z_1 \, \mathrm{d}^4 z_2 \, S_{\mathcal{A}}(x,z_1) \left[\Sigma_{\mathrm{VP}}(z_1,z_2) + \Sigma_{\mathrm{SE}}(z_1,z_2) \right] S_{\mathcal{A}}(z_2,y),$$

with

$$\Sigma_{\mathrm{VP}}(z_1,z_2) := -\delta(z_1 - z_2)(-ie\gamma^\mu) \int \mathrm{d}z \, S_P(z_1 - z)\mathrm{Tr}[(-ie\gamma_\mu)S_{\mathcal{A}}(z,z)],$$

$$\Sigma_{\mathrm{SE}}(z_1,z_2) := (-ie\gamma^\mu)S_{\mathcal{A}}(z_1,z_2)S_P(z_1 - z_2)(-ie\gamma_\mu),$$

where $g_{\mu\nu}S_P(x - y)$ is the photon propagator in position space (Appendix A.1). Using the Fourier transformed functions

$$\Sigma_{\mathrm{VP/SE}}(\mathbf{z}_1, \mathbf{z}_2, E) = \int \mathrm{d}z_1^0 \, \mathrm{e}^{iE(z_1^0 - z_2^0)} \Sigma_{\mathrm{VP/SE}}(z_1, z_2),$$

and the spectral representation of the propagator from Eq. (1.11), the level shifts of the n-th level can be extracted from the shift of the poles [153, Section 14.2.] as

$$\Delta E_n = \int \mathrm{d}^3\mathbf{x} \, \mathrm{d}^3\mathbf{y} \, \bar{u}_n(\mathbf{x}) \left(-\Sigma_{\mathrm{VP}}(\mathbf{x}, \mathbf{y}, E_n) - \Sigma_{\mathrm{SE}}(\mathbf{x}, \mathbf{y}, E_n) \right) u_n(\mathbf{y}).$$

1.1.1 Vacuum polarization potentials

For practical calculations of the vacuum polarization (VP) of order α, the closed fermion loop in Fig. 1.2 (b) can be expanded in numbers of interactions with the background field, using Eq. 1.10. For the case of atomic physics, since the nuclear potential is proportional to the nuclear charge number Z, this expansion is in powers of $Z\alpha$. The corresponding diagrams in order $\alpha(Z\alpha)$ (Uehling potential [158]) and $\alpha(Z\alpha)^3$ (Wichmann-Kroll

potential [159]) are shown in Fig. 1.3. Since the closed loop now is formed by the free fermion propagator, all diagramms of order $\alpha(Z\alpha)^n$ with even n vanish as a consequence of Furry's theorem [156, Section 10.1.]. Formally, the order $\alpha(Z\alpha)$ correction δS_{Uehl} from diagram (a) in Fig. 1.4 to the propagator $S_{\mathcal{A}}$ reads

$$\delta S_{\mathrm{Uehl}}(x,y) = \int \mathrm{d}z_1\, S_{\mathcal{A}}(x,z_1)\Sigma_{\mathrm{Uehl}}(z_1)S_{\mathcal{A}}(z_1,y) \tag{1.12}$$

with

$$\begin{aligned} \Sigma_{\mathrm{Uehl}}(z_1) \quad &:= - \int \mathrm{d}z_2 (-ie\gamma^\mu) S_P(z_1 - z_2) \\ &\times \int \mathrm{d}z_3\, \mathrm{Tr}\left[(-ie\gamma_\mu)S_F(z_2 - z_3)(-e\gamma^\nu \mathcal{A}_\nu(z_3))S_F(z_3 - z_2)\right]. \end{aligned}$$

Analogously to the inclusion of the external field in the propagator from Eq. (1.9), Eq. (1.12) and the corresponding iterations from diagrams (b), (c), ... in Fig. 1.4 can be summed to define a propagator $S_{\mathcal{A}+\mathrm{Uehl}}$ which contains all iterations both in the external field and the order $\alpha(Z\alpha)$ VP via the integral equation

$$S_{\mathcal{A}+\mathrm{Uehl}}(x,y) = S_{\mathcal{A}}(x,y) + \int \mathrm{d}z_1\, S_{\mathcal{A}}(x,z_1)\Sigma_{\mathrm{Uehl}}(z_1)S_{\mathcal{A}+\mathrm{Uehl}}(z_1,y). \tag{1.13}$$

This propagator is a Green's function for the Dirac equation including the external field and the Uehling potential as

$$\left(i\gamma^\mu\partial_\mu - m_f - e\gamma^\mu\mathcal{A}_\mu + \Sigma_{\mathrm{Uehl}}\right)S_{\mathcal{A}+\mathrm{Uehl}}(x,y) = \delta(x-y).$$

As a result, the diagrams in Fig. 1.4 can be treated by solving the Dirac equation (1.7) including the Uehling potential. The same reasoning holds as well for the Wichmann-Kroll potential (Fig. 1.3 (b)) and for the order $\alpha^2(Z\alpha)$ VP, referred to as the Källén-Sabry potential [160], where the corresponding diagrams are shown in Fig. 1.5.

Since the formal expressions for the VP potentials contain divergences, they have to be renormalized. This section concludes with giving the corresponding expressions for the renormalized Uehling (order $\alpha(Z\alpha)$) and Källén-Sabry (order $\alpha^2(Z\alpha)$) potentials for a virtual electron-positron pair and an extended, spherically symmetric nuclear charge distribution $\rho(r)$, which can be included in the Dirac equation. It is important to note, that the virtual particle in the loop can be a different one compared to the considered fermion. Therefore, the mass of the virtual particle is m_l, which is an additional dependency of the potential. For an electron-positron loop, correspondingly $m_l = m_e$ and for a muon-antimuon loop $m_l = m_\mu$. For example, the electronic VP in muonic atoms is more important than the muonic VP. The Uehling potential reads as [161, 162]

$$\begin{aligned} V_{\mathrm{Uehl}}^{(m_l)}(r) = -\alpha\frac{2\alpha}{3\pi}\int_0^\infty \mathrm{d}r'\, 4\pi\rho(r')\int_1^\infty \mathrm{d}t\left(1 + \frac{1}{2t^2}\right) \\ \times \frac{\sqrt{t^2-1}}{t^2}\frac{\exp(-2m_l|r-r'|t) - \exp(-2m_l(r+r')t)}{4m_l rt}, \end{aligned} \tag{1.14}$$
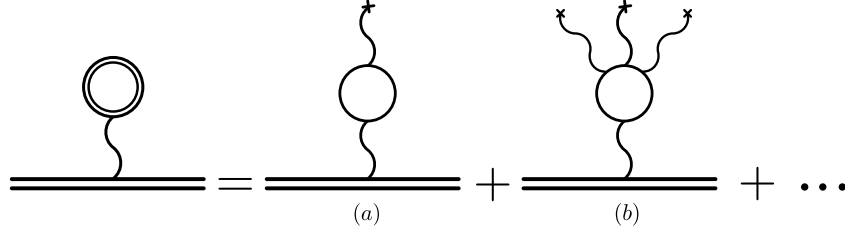
Figure 1.3: Expansion of the order α VP in powers of $(Z\alpha)$, i.e. in number of interactions with the nuclear field. The contributions with odd powers vanish due to Furry's theorem. The $\alpha(Z\alpha)$ contribution (diagram a) is the Uehling term, the $\alpha(Z\alpha)^3$ contribution (diagram b) is the Wichmann-Kroll term.
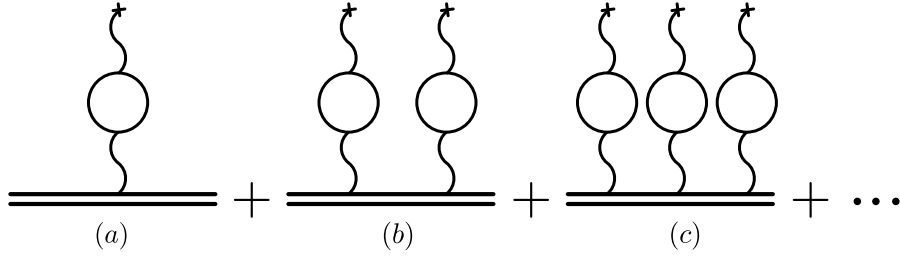
Figure 1.4: Resummation of iterations of the Uehling potential needed for the modified propagator from Eq. (1.13).

and the Källén-Sabry potential, corresponding to the diagrams in Fig. 1.5, is derived in Refs. [163–166] and given e.g. in Refs. [161, 167] as

$$V_{\text{KS}}^{(m_l)}(r) = \frac{\alpha^2(Z\alpha)}{\pi r} \int\limits_0^\infty dr'\, r'\rho(r') \left(L_0(2m_l|r-r'|) - L_0(2m_l(r+r'))\right), \qquad (1.15)$$

with

$$L_0(x) = -\int^x dy\, L_1(y),$$

$$L_1(x) = \int\limits_1^\infty dt\, e^{-rt} \left\{ \left(\frac{2}{3t^5} - \frac{8}{3t}\right) f(t) + \left(\frac{2}{3t^4} + \frac{4}{3t^2}\right) \sqrt{t^2-1}\, \ln[8t(t^2-1)] \right.$$

$$\left. + \left(\frac{2}{9t^2} + \frac{7}{108t^4} + \frac{13}{54t^2}\right) \sqrt{t^2-1} + \ln(\sqrt{t^2-1}+t)\left(\frac{2}{9t^7} + \frac{5}{4t^5} + \frac{2}{3t^3} - \frac{44}{9t}\right) \right\},$$

$$f(t) = \int\limits_t^\infty dx \left[\frac{(3x^2-1)\ln(\sqrt{x^2-1}+x)}{x(x^2-1)} - \frac{\ln(8x(x^2-1))}{\sqrt{x^2-1}} \right].$$
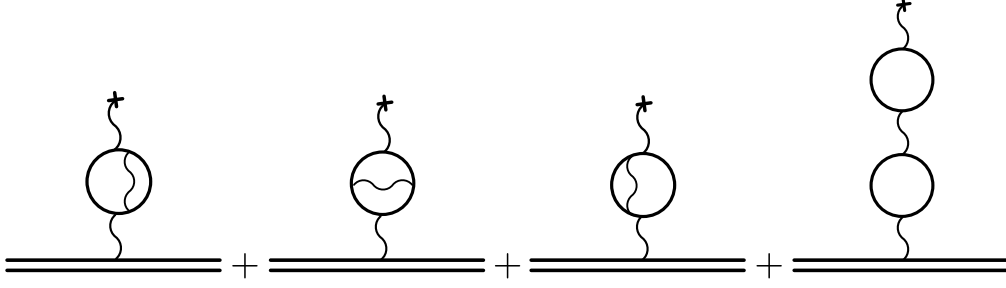
Figure 1.5: Feynman diagrams corresponding contribution to the Källén-Sabry potential of order $\alpha^2(Z\alpha)$, as given in Eq. (1.15).

1.2 Dirac equation in central potentials

In the previous section, the binding energies of a fermion bound by an atomic nucleus were analyzed in the framework of the Furry picture of QED. The zeroth order approximations were shown to be the eigenenergies of the solutions of the Dirac equation (for a $\mathbb{C}$-number field) including the nuclear background field. Furthermore, it was demonstrated that certain radiative corrections can be included as potentials in the Dirac equation as well. To a first approximation, the nuclear potential can be described by a static electric field which possesses spherical symmetry, and deviations thereof may be treated later on by perturbation theory. Thus, in this section, the solutions of the Dirac equation for a spherical symmetric potential are discussed, mainly following [42, 153]. Then, the case of the pure Coulomb potential is discussed, where the solution can be given in closed form due to the high degree of symmetry. Finally, the dual-kinetic-balance method [152] for numerical solutions for arbitrary spherical symmetric potentials is discussed.

Firstly, the Dirac equation (1.7) for the functions v_n is rewritten, such that it has the same form as for u_n. For this, add a new range of indices $\tilde{n}$ to the original n and define $u_{\tilde{n}}(x) \coloneqq v_n(x)$, $E_{\tilde{n}} \coloneqq -E_n$. Secondly, static electric background fields are considered, which corresponds to a four potential

$$\mathcal{A}_\mu(x) = (\Phi(\mathbf{x}), \mathbf{0}),$$

where the electric potential $\Phi(\mathbf{r})$ can be expressed in terms of a spherically symmetric nuclear charge distribution $\rho(|\mathbf{r}|)$ as

$$e\Phi(\mathbf{r}) = -Z\alpha \int \mathrm{d}^3\mathbf{r}' \, \frac{\rho(|\mathbf{r}'|)}{|\mathbf{r} - \mathbf{r}'|}, \tag{1.16}$$

where $\int \mathrm{d}V \, \rho(|\mathbf{r}|) = 1$. Since Φ only depends on $|\mathbf{r}|$, we define

$$V(r) \coloneqq e\Phi((r, 0, 0))$$

for spherical coordinates $\mathbf{r} = (r, \vartheta, \varphi)$. Thereby, the Dirac equation (1.7) reads as

$$\mathrm{H}_D u_n(\mathbf{r}) := (i \boldsymbol{\alpha} \cdot \nabla + \beta m_f + V(r)) u_n(\mathbf{r}) = E_n u_n(\mathbf{r}), \qquad (1.17)$$

where the eigenenergies E_n are both positive and negative and the spectrum contains both continuum and discrete parts. $u_n(\mathbf{r})$ are the corresponding solutions in form of four-component spinors. For an arbitrary spherically symmetric potential $V(r)$, the solution can be simplified significantly by reducing the partial differential equation (1.17) to an ordinary differential equation.

For the Dirac Hamiltonian with spherical symmetry, energy eigenfunctions can be found, which also have a well-defined parity and total angular momentum. At first, the relativistic angular quantum number κ is introduced as a function of the orbital angular momentum quantum number l and total angular momentum quantum number j as

$$\kappa(j, l) := (-1)^{j+l+1/2} \left(j + \frac{1}{2} \right).$$

Since for a Dirac particle every value of l has two possible values $j = l \pm 1/2$, the mapping $\kappa \leftrightarrow (j, l)$ is bijective with $j(\kappa) = |\kappa| - 1/2$; $l(\kappa) = |\kappa| + (\mathrm{sgn}(\kappa) - 1)/2$. Eigenfunctions of the total angular momentum can be constructed by the eigenfunctions of the orbital angular momentum and spin operator, the spherical harmonics $\mathrm{Y}_{lm}(\vartheta, \varphi)$ and two-component spinors $\chi_{1/2} = (1, 0)^T$; $\chi_{-1/2} = (0, 1)^T$, respectively as

$$\Omega_{\kappa m}(\vartheta, \varphi) := \sum_{m_l=-l(\kappa)}^{l(\kappa)} \sum_{m_s=-1/2}^{1/2} \mathrm{C}_{l(\kappa)m_l \, 1/2 \, m_s}^{j(\kappa)m} \mathrm{Y}_{l(\kappa)m_l}(\vartheta, \varphi) \chi_{m_s}, \qquad (1.18)$$

where $\mathrm{C}_{l_2 m_2 \, l_3 m_3}^{l_1 m_1}$ are the Clebsch-Gordan coefficients [168]. The functions defined in Eq. (1.18) are called *spherical spinors*. Direct calculations shows that a pair $(\Omega_{\kappa m}, \Omega_{-\kappa m})$ have the same values for j, but opposite parity. Motivated by the solutions of the free Dirac equation, the solution is written with an ansatz in two component spinors, with a priori different values for κ_1, κ_2, m_1, m_2. However, for a well defined total angular momentum and z-component of the total angular momentum $|\kappa_1| = |\kappa_2|$ and $m_1 = m_2$ are needed. Furthermore, the application of the parity operator reveals that the lower component needs to have the opposite parity compared to the upper component such that the total four-component spinors has a well-defined parity. Therefore, it has to hold that $\kappa_1 = -\kappa_2$. As a result, the solutions are written as

$$u_{n\kappa m_j}(\mathbf{r}) = \begin{pmatrix} g_{n\kappa}(r)\Omega_{\kappa m_j}(\vartheta, \varphi) \\ i f_{n\kappa}(r)\Omega_{-\kappa m_j}(\vartheta, \varphi) \end{pmatrix}. \qquad (1.19)$$

Using this ansatz in Eq. (1.17) leads to the following system of equations for the radial

functions $g_{n\kappa}(r)$ and $f_{n\kappa}(r)$:

$$\frac{\mathrm{d}g(r)}{\mathrm{d}r} + (1 + \kappa)\frac{g(r)}{r} - [E + m_f - V(r)]\, f(r) = 0,$$

$$\frac{\mathrm{d}f(r)}{\mathrm{d}r} + (1 - \kappa)\frac{f(r)}{r} + [E - m_f - V(r)]\, g(r) = 0. \tag{1.20}$$

1.2.1 Bound state solutions of the Coulomb problem

For a point-like nucleus with charge number Z, the pure Coulomb potential reads

$$V_C(r) = -\frac{Z\alpha}{r}, \tag{1.21}$$

and the radial equations (1.20) can be solved analytically in this case. As a first step, the radial wave functions are substituted with

$$g_{n\kappa}(r) = \sqrt{1 + E_{n\kappa}}\, \mathrm{e}^{-\lambda r}(\varphi_1(r) + \varphi_2(r))$$
$$f_{n\kappa}(r) = \sqrt{1 - E_{n\kappa}}\, \mathrm{e}^{-\lambda r}(\varphi_1(r) - \varphi_2(r)),$$

and for the functions $\varphi_i(r)$ the power-series ansatz

$$\varphi_i(r) = (2\lambda r)^\gamma \sum_{k=0}^\infty a_k^{(i)}(2\lambda r)^k,$$

is assumed, where $\lambda = \sqrt{1 - E_{n\kappa}^2}$ and $\gamma = \pm\sqrt{\kappa^2 - (Z\alpha)^2}$. Plugging this ansatz into Eq. (1.20) results in recurrence relations, such that the solution can be expressed only in terms of the normalization coefficient $a_0^{(1)}$ as

$$\varphi_1(r) = a_0^{(1)}(2\lambda r)^\gamma\, \mathrm{F}(1 - n_r, 2\gamma + 1, 2\lambda r)$$
$$\varphi_2(r) = a_0^{(1)}(\kappa - Z\alpha/\lambda)(2\lambda r)^\gamma\, \mathrm{F}(-n_r, 2\gamma + 1, x)/n_r,$$

where $n_r = Z\alpha E_{n\kappa}/\lambda - \gamma$ and $\mathrm{F}(a, b, c)$ are the hypergeometric function, as defined in Eq. (A.3). Now, for the positive value of γ, the solutions are regular at the origin, but behave as $\mathrm{e}^{\lambda r}$ as $r \to \infty$. On the other hand, linear combination of positive and negative values of γ enable solutions which are regular at infinity but are divergent at the origin. Solutions regular both at the origin and at infinity can only be obtained for certain energies, corresponding to integer values of n_r [169]. Therefore, with the principal quantum number $n = n_r + |\kappa|$, the bound state energies read

$$E_{n\kappa} = \frac{m_f}{\sqrt{1 + \dfrac{(Z\alpha)^2}{\left(n - |\kappa| + \sqrt{|\kappa|^2 - (Z\alpha)^2}\right)^2}}}, \tag{1.22}$$

for $n = 1, 2, 3, \ldots$ and $\kappa = \pm 1, \ldots, \pm(n-1), -n$. These solution explains the spectrum of hydrogen-like atoms to a reasonable accuracy, including fine-structure splitting, as long as $Z\alpha \ll 1$. The solutions are degenerate in the sign of κ, i.e. states with the same j but different l have the same energy. As a result, the $2s_{1/2}$ and $2p_{1/2}$ states are degenerate. The lifting of this degeneracy (Lamb shift) can be explained by radiative corrections and finite nuclear size effects. However, in situations where $Z\alpha$ is on the order of unity, the point-like approximation becomes increasingly worse and solutions of the Dirac equation for non-Coulomb, extended potentials have to be used.

1.2.2 Numerical solution in a cavity for arbitrary potentials

Except the rare cases, where the radial equations (1.20) can be solved exactly (e.g. Coulomb potential, spherical potential well), numerical methods have to be used to obtain solutions for $g(r)$ and $f(r)$. In particular, for atomic systems with large finite nuclear size effects, like highly charged, heavy ions and muonic atoms, the nuclear potential deviates from the Coulomb potential significantly and numerical solutions have to be found, including the extended nuclear charge distribution.

Generally, for finite basis set solutions of the Dirac equation, the radial equations (1.20) are considered, but the domain is changed from $r \in [0, \infty)$ to a finite cavity $r \in [0, R]$. On the original domain, the spectrum of the energy eigenvalues E has a negative continuum $E \in (-\infty, -m_f]$, a positive continuum $E \in [m_f, \infty)$, and a discrete part $E \in (-m_f, m_f)$ of infinitely many bound states, where m_f is the mass of the bound fermion. On the modified domain, the positive and negative continuum become discrete [170], but still infinite. A problem with numerical solutions of the Dirac equation is the appearance of unphysical, or spurious states [170, 171]. A method circumventing this problem was presented in Ref. [152], which is shortly described in the following.

The radial equations (1.20) can be rewritten in matrix form as

$$\begin{pmatrix} m_f + V(r) & -\partial_r + \kappa/r \\ \partial_r + \kappa/r & -m_f + V(r) \end{pmatrix} \nu(r) =: \mathrm{H}_\kappa \nu(r) = E\,\nu(r) \tag{1.23}$$

for the function $\nu(r) = (G(r), F(r))^T = (rg(r), rf(r))^T$. As a finite set of basis functions, B-splines $\Pi_{i,k}(r)$ of order k with a suitable knot sequence as described in Ref. [170] are selected, where the first and last spline is set to zero. With the size of the basis set n, the solutions are expressed with $2n$ coefficients c_i as

$$\nu(r) = \sum_{i=1}^{2n} c_i\,\nu_i(r) := \sum_{i=1}^{n} c_i \begin{pmatrix} \Pi_{i,k}(r) \\ (\partial_r + \kappa/r)\Pi_{i,k}(r)/(2m_f). \end{pmatrix} + \sum_{i=n+1}^{2n} c_i \begin{pmatrix} (\partial_r - \kappa/r)\Pi_{i,k}(r)/(2m_f) \\ \Pi_{i,k}(r) \end{pmatrix}. \tag{1.24}$$

Thereby, the infinite amount of discrete states in the cavity are reduced to $2n$ states. The finite basis expansion (1.24) can be plugged into the radial equations (1.23) which results in the generalized eigenvalue problem [152] for the $2n$ coefficients c_j

$$\mathrm{A}\mathbf{c} = E\,\mathrm{B}\mathbf{c}, \tag{1.25}$$

where $\mathbf{c} = (c_1, ..., c_{2n})^T$ and for $i, j \in \{1, ..., 2n\}$ the matrices read

$$A_{ij} = \left(\nu_i^T(r) H_\kappa(r) \nu_j(r) + \nu_j^T(r) H_\kappa(r) \nu_i(r) \right) / 2,$$
$$B_{ij} = \nu_i(r)^T \nu_j(r).$$

This eigenvalue problem can be solved efficiently with existing libraries for B-splines and linear algebra.

In the case of a positively charged nucleus with $Z\alpha < 1$, the eigenvalues of the solution of Eq. (1.25) consist of n negative values, forming a discrete representation of the negative continuous spectrum and of n positive values representing the bound state spectrum and the positive continuous spectrum [171]. Besides the eigenenergies, approximations of the bound and continuum Dirac wave functions are obtained in terms of the coefficients c_i and Eq. (1.24). This enables the numerical evaluation of intermediate sum of states occurring in second order perturbation theory or in the spectral representation of the Dirac propagator.

Chapter 2

Level structure of muonic atoms

This chapter is devoted to the prediction of the level structure and transition probabilities in muonic atoms, with focus on high nuclear charge numbers. Compared to conventional atomic electrons, the much higher muon mass reduces the length- and increases the energy scales by the muon-to-electron mass ratio. Thereby, all finite nuclear size and shape effects are much more important and excited nuclear states also have to be taken into account.

This chapter is organized in the following way:

At first, a motivation for new structure calculations is given in Section 2.1.1 and the current status of existing methods is reviewed. The status of new experiments in the field are explained.

Afterwards, the theoretical framework and implementation of several important effects is shown in Sections 2.1.2 to 2.1.4. Here, finite-basis-set methods are used for precision calculations and results for selected nuclei are presented.

In Sections 2.2.1 and 2.2.2, improved methods for the calculation of higher-order effects in electric hyperfine interactions are presented.

Finally, in Sections 2.3, calculations and data from recent experiments on isotopically pure $^{185}_{75}$Re and $^{187}_{75}$Re are compared. Here, a combination of theoretical predictions and experimental measurements of muonic transitions enabled the extraction of the nuclear quadrupole moment.

2.1 Calculation of spectra for muonic atoms

2.1.1 Motivation

Atomic nuclei are one of the building blocks of matter and therefore, information on their structure, like the distribution of electric charge inside the nucleus, is of intrinsic interest. Furthermore, the charge radii of atomic nuclei are of importance as an input parameter for the interpretation of other experiments. For example, radium is a candidate for measuring atomic parity violation effects, but for this a more accurate value of the radium charge radii is needed [172]. There are several methods for extracting information on the nuclear charge distribution, i.e. the distribution of protons inside the atomic nucleus, like electron scattering [173] or laser spectroscopy [174–176]. One method is also muonic atom spectroscopy. Here, a muon, which is a negatively charged elementary particle is brought in the proximity of an atomic nucleus. Then, the negatively charged muon forms bound states with the positively charged nucleus and radiation due to muonic transitions

can be analyzed in order to extract information on the nuclear charge distribution and measure quantities like nuclear charge radii and quadrupole moments.

Correspondingly, the theory of muonic atoms has been developed in order to describe the level structure and the probabilities for muonic transitions. The general approach is that for a given nuclear charge distribution, the spectrum of the corresponding muonic atom needs to be predicted. Then, vice versa, for a measured spectrum the nuclear charge distribution can be extracted. An overview of the different contributions to the energy levels of muonic atoms can be found for example in Ref. [83]. Hitherto, the majority of analyses of the spectra of heavy muonic atoms used the computer programs `MUON` and `RURP` from the 1970s [86]. There are two main differences compared to the approach used in this thesis: Firstly, in the `MUON` and `RURP` codes, only up to 9 muonic states can be considered whereas in this thesis, the dual-kinetic-balance method [152] is used. With this finite-basis-set method, an approximation of the complete muon spectrum can be obtained, i.e. bound states and positive as well as negative continuum states, including the effects of the finite nuclear charge distribution. Thereby, numerical summations over the complete muon spectrum are possible. In this way, the numerical calculation of the second order hyperfine interactions without approximations is presented in Section 2.2.2. Secondly, whereas in the `MUON` and `RURP` codes, the fine and hyperfine structure are calculated separately, in this thesis the calculations of the fine and hyperfine structure are performed at once, based on a given nuclear charge distribution, enabling improved analysis of the dependence of the muonic spectrum on parameters of the nuclear charge distribution.

Furthermore, new experiments on high Z muonic atoms are performed by the MuX-Collaboration at the Paul Scherrer Institute (PSI) in Villigen (Switzerland) [177, p. 3]. One of the goals is to measure the charge radius for radium, needed for experiments on atomic parity violations, as mentioned earlier in this section. Furthermore, measurements on muonic atoms involving several nuclei will be or have been performed for the first time, involving isotopically pure rhenium. The corresponding structure calculations for muonic rhenium were performed during the work on this thesis. The combined analysis of theoretical and experimental results is shown in Section 2.3.

2.1.2 Theoretical framework

A muon is a charged elementary particle, which is in many aspects similar to the electron, in particular, it has the same electric charge, but it is approximately 207 times heavier than the electron [91]. When coming close to an atom, a muon can be captured by the nucleus and can form a hydrogen-like muonic ion. This atomic system is commonly referred to as a muonic atom. The lifetime of the muon is big enough to be considered stable in the structure calculations of these muonic bound states. In muonic atoms, nuclear effects on the energy levels are much larger compared to conventional electronic atoms. This can be seen by considering the ratio of the nuclear radius and the Bohr radius of the bound fermion, which is the typical length scale for the bound muon or electron. The larger this ratio is, the larger are nuclear finite size effects. The Bohr radius for a hydrogen-like atomic system with a bound fermion of mass m_f and a nuclear

Table 2.1: Comparison of the nuclear charge radius R_N and the Bohr radius r_B of a bound electron or muon in the corresponding hydrogen-like atomic system for hydrogen, helium, rhenium, and uranium. If this ratio is small, the finite size of the nucleus does not influence the bound fermion significantly. On the other hand, if this ratio is on the order of 1, large finite nuclear size and nuclear structure effects can be expected. The nuclear charge radii are taken from [178].

Fermion type	Nucleus	R_N[fm]	r_B[fm]	R_N/r_B
e^-	$^1_1$H	0.8783	52917.721	1.660×10^{-5}
μ^-	$^1_1$H	0.8783	255.928	3.432×10^{-3}
e^-	$^4_2$He	1.6755	26458.861	6.332×10^{-5}
μ^-	$^4_2$He	1.6755	127.964	1.309×10^{-2}
e^-	$^{185}_{75}$Re	5.3596	705.570	7.596×10^{-3}
μ^-	$^{185}_{75}$Re	5.3596	3.412	1.571
e^-	$^{238}_{92}$U	5.8571	575.193	1.018×10^{-2}
μ^-	$^{238}_{92}$U	5.8571	2.782	2.105

charge number Z reads as

$$r_B = \hbar/(m_f c_0 Z \alpha),$$

where $\hbar$ is the Planck's constant, α is the fine-structure constant and c_0 is the speed of light in vacuum. In Table 2.1, the nuclear radius, the Bohr radii for the corresponding electronic and muonic hydrogen-like ions, and their ratios are shown for a selection of nuclei, from very light to very heavy. It can be seen that, that for electronic atoms, the nucleus is generally a few orders of magnitude smaller compared to the extent of the electronic wave function, which is given by the Bohr radius, although for high Z, the electron is much closer to the nucleus due to the strong Coulomb attraction. Since the Bohr radius is inversely proportional to the mass of the bound fermion, the situation in muonic atomic systems is different. While for low Z, the extent of the muonic wave functions is still much larger than the nuclear radius, for high Z, the nuclear radius is actually larger than the muonic Bohr radius. In Fig. 2.1, the muonic and electronic ground state wave functions for hydrogen-like uranium are shown in comparison to the nuclear charge distribution. This means the overlap between muonic wave functions and nucleus is large in this case. Also, a typical energy scale for hydrogen-like systems is the ground state binding energy from Eq. (1.22) for a point-like nucleus, which reads as

$$E_{0,\text{point}} = m_f(1 - \sqrt{1 - (Z\alpha)^2}),$$

and is proportional the fermion mass. As a consequence, for muonic atoms and high charge numbers, muonic transitions can have an energy of several MeV and fine-structure splitting can be on the order of 100 keV. Excitation energies of nuclear rotational states
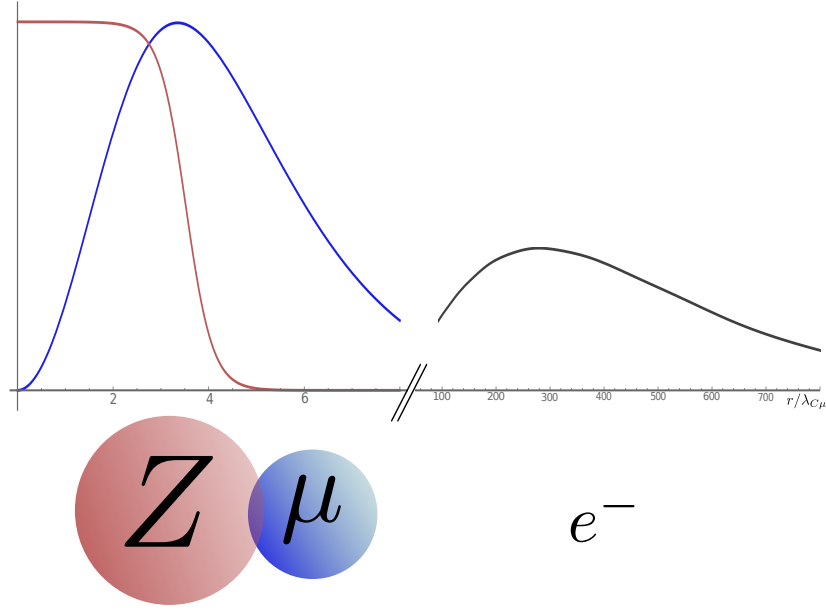
Figure 2.1: The monopole charge distribution for the nucleus (red) and the $1s_{1/2}$ wave functions of the muon (blue) and the electron (gray, enhanced by a factor of 50) for hydrogen-like uranium. The muonic wave function overlaps strongly with the nuclear charge distribution. Therefore finite nuclear size effects are enhanced in muonic atoms

are of the same order [179] and therefore, an extended nuclear model has to be used, which contains the excited nuclear states of the ground state rotational band. Here, the symmetric rigid rotor model for nuclei with axial symmetry has proved successful in describing heavy muonic atoms, see e.g. Refs. [73, 78, 84, 85], and also is used in this thesis. The symmetric rigid rotor model is presented in Appendix A.4, where also the expressions for the nuclear wave functions in terms of Wigner D-functions can be found. In the symmetric rigid rotor model, the nucleus is described by a charge distribution $\rho(\mathbf{r})$ given in the body fixed nuclear frame, and the Euler angles $\Omega = (\phi, \theta, \psi)$ describe its position in the laboratory frame. The rotational state of the nucleus $|IM_IK\rangle$ is given by the total nuclear angular momentum quantum number I, its projection on the z axis of the laboratory frame M_I and on the z axis of the body fixed frame K, where K also corresponds to the ground state angular momentum. As derived in Chapter 1, the muonic bound states without radiative corrections can be obtained by solving the Dirac equation for the nuclear potential. Therefore, the coupled system of muon as a Dirac particle and nucleus as a rigid rotor is described by the eigenvalue equation

$$\mathrm{H}\left(|N\rangle \otimes |\mu\rangle\right) = \left(\mathrm{H_N} + \mathrm{H}_\mu + V_{\mathrm{el}}\right)\left(|N\rangle \otimes |\mu\rangle\right) = E\left(|N\rangle \otimes |\mu\rangle\right), \qquad (2.1)$$

where H_{N} is the nuclear rigid rotor Hamiltonian, and $H_\mu = \boldsymbol{\alpha} \cdot \mathbf{p} + \beta m_\mu$ is the free Dirac Hamiltonian for the muon with momentum $\mathbf{p}$, and $\boldsymbol{\alpha}$, β are the four Dirac matrices. $|N\rangle$ is the nuclear state and $|\mu\rangle$ is the muon state. Following Eq. (1.16), the electric potential

energy between muon and nuclear charge distribution reads as

$$V_{\text{el}}(\mathbf{r}'_\mu) = -Z\alpha \int \mathrm{d}^3 r'_N \frac{\rho(\mathbf{r}'_N)}{|\mathbf{r}'_\mu - \mathbf{r}'_N|}. \tag{2.2}$$

It is important to recall, that the nuclear charge distribution is given in the body fixed nuclear frame, thus the integration in Eq. (2.2) in most conveniently performed in this frame. The resulting expression in dependence of the position of the muon, however, is needed in the laboratory frame. Therefore, in the following, a multipole expansion of Eq. (2.2) is performed, and the result is given as a function of the muon position in the laboratory frame and the Euler angles describing the orientation of the nuclear frame. Here, vectors are written in spherical components as $\mathbf{r}_i = (r_i, \vartheta_i, \varphi_i)$ in the laboratory frame and as $\mathbf{r}'_i = (r'_i, \vartheta'_i, \varphi'_i)$ in the body-fixed nuclear frame. Since rotations do not change the absolute values, it holds that $r'_i = r_i$.

With the multipole expansion of the Coulomb potential [180]

$$\frac{1}{|\mathbf{r}'_\mu - \mathbf{r}'_N|} = \sum_{l=0}^{\infty} \frac{r^l_<}{r^{l+1}_>} \sum_{m=-l}^{l} \mathrm{C}^*_{lm}(\vartheta'_N, \varphi'_N)\mathrm{C}_{lm}(\vartheta'_\mu, \varphi'_\mu),$$

where $r_< := \min(r'_\mu, r'_N)$, $r_> := \max(r'_\mu, r'_N)$, the electric potential (2.2) can be written as

$$V_{\text{el}}(\mathbf{r}'_\mu) = \sum_{l,m} -Z\alpha \left[\int \mathrm{d}^3 r'_N \frac{r^l_<}{r^{l+1}_>} \mathrm{C}^*_{lm}(\vartheta'_N, \varphi'_N)\rho(\mathbf{r}'_N) \right] \mathrm{C}_{lm}(\vartheta'_\mu, \varphi'_\mu),$$

where $\mathrm{C}_{lm}(\vartheta, \varphi) = \sqrt{4\pi/(2l+1)}\mathrm{Y}_{lm}(\vartheta, \varphi)$ are the normalized spherical harmonics. For axially symmetric charge distributions, only the $m=0$-terms contribute after integrating over the charge distribution. The dependency on the muonic angular variables can be transformed to the laboratory system using the Euler angles by

$$\mathrm{P}_l(\cos\vartheta'_\mu) = \sum_{m=-l}^{l} C^*_{lm}(\theta, \phi)C_{lm}(\vartheta_\mu, \varphi_\mu),$$

which is a special case of Eq. (A.9). Thereby, the potential as a function of the Euler angles and the muon's position in the laboratory frame reads

$$\begin{aligned}
V_{\text{el}}(\mathbf{r}_\mu, \phi, \theta) &= \sum_{l=0}^{\infty} -Z\alpha \left[\int \mathrm{d}^3 r'_N \frac{r^l_<}{r^{l+1}_>} \mathrm{P}_l(\cos\vartheta'_N)\rho(\mathbf{r}'_N) \right] \sum_{m=-l}^{l} \mathrm{C}^*_{lm}(\theta, \phi)\mathrm{C}_{lm}(\vartheta_\mu, \varphi_\mu). \\
&=: \sum_{l=0}^{\infty} Q^{(l)}_{\text{el}}(r_\mu) \sum_{m=-l}^{l} C^*_{lm}(\theta, \phi)C_{lm}(\vartheta_\mu, \varphi_\mu) \\
&=: \sum_{l=0}^{\infty} V^{(l)}_{\text{el}}(\mathbf{r}_\mu, \phi, \theta),
\end{aligned} \tag{2.3}$$

where $Q_{\mathrm{el}}^{(l)}(r_\mu)$ describe the radial distribution of the multipole moments and the dependency on the muonic angles and the Euler angles is in form of a scalar product of spherical tensor operators. This means that the interaction energy only depends on the relative orientation of the muon with respect to the body fixed nuclear z' axis.

Most nuclei turn out to be symmetric with respect to reflection in the (x', y')-plane [181]. This results in only even-l terms in Eq. (2.3) being non-zero, thus the first two terms are the monopole term $l = 0$ and the quadrupole term $l = 2$. The next term would be the $l = 4$ hexadecapole terms. However, the higher order terms are usually not needed for the correct description of the hyperfine level structure [83]. From Eq. (2.3), it follows that the monopole terms only depends on the muonic radial variable, since it can be written as

$$V_{\mathrm{el}}^{(0)}(r_\mu) = -Z\alpha \int \mathrm{d}^3\mathbf{r}'_N \frac{\rho(\mathbf{r}'_N)}{r_>}.$$

In fact, the $l = 0$ term is the averaged nuclear potential already derived in Eq. (3.2) in the previous chapter on the g factor of spinless nuclei. As a consequence, the $l = 0$-term can be used as a potential in the spherically symmetric Dirac equation to define the unperturbed muonic states as

$$\left(\boldsymbol{\alpha} \cdot \mathbf{p} + \beta m_\mu + V_{\mathrm{el}}^{(0)}(r_\mu)\right) |n\kappa m\rangle = E_{n\kappa} |n\kappa m\rangle. \tag{2.4}$$

The unperturbed nuclear states are the rigid rotor states from Eq. (A.16) with

$$\mathrm{H}_N |IM_I K\rangle = E_N |IM_I K\rangle, \tag{2.5}$$

where the excitation energies of the nuclear rotational states are typically taken from experiments [179], and not parametrized by the moment of inertia from Eq. (A.15). The $l = 2$ quadrupole term couples nuclear and muonic degrees of freedom and is treated in Section 2.1.4, and 2.2.2. The multipole interaction from Eq. (2.3) in general, and the quadrupole interaction with $l = 2$ in particular has the structure of a scalar product of two irreducible tensor operators, as defined in Eq. (A.12). One operator acts on the nuclear angular variables, i.e. the Euler angles, and one on the muonic angular variables. For these types of operators, the calculation of expectation values can be simplified by using the theory of irreducible tensor operators, as described in Appendix A.3. Therefore, states of defined total angular momentum have to be considered as

$$|FM_F\, IK\, n\kappa\rangle = \sum_{M_I, m} \mathrm{C}_{IM_I\, j(\kappa)m}^{FM_F} |IM_I K\rangle \, |n\kappa m\rangle \tag{2.6}$$

with total angular momentum F, nuclear angular momentum I and muonic angular momentum j. The muonic angular momentum j is already composed out of the orbital angular momentum l and the spin angular momentum, as described in Eq. (1.19). The total energy of the muon-nucleus system can be calculated as the sum of nuclear energy E_N from Eq. (2.5), the muonic energy from Eq. (2.4) and the expactation value of the quadrupole interaction $\left\langle V_{\mathrm{el}}^{(2)} \right\rangle$ from Eq. (2.3).

2.1.3 Fine and first-order hyperfine structure

In this subsection, the solution of the Dirac equation and the calculation of first-order hyperfine interactions for the muon will be discussed. In particular, the effects of vacuum polarization in Uehling approximation, recoil corrections, and electron screening are implemented, using known methods. The usage of the dual-kinetic-balance method [152] in the framework of muonic atoms is presented. Results are shown for muonic $^{205}_{83}\mathrm{Bi}$, $^{147}_{62}\mathrm{Sm}$, and $^{89}_{40}\mathrm{Zr}$. This subsection follows Ref. [1], which was published in the framework of this thesis.

2.1.3.1 Finite nuclear size corrections

For considering monopole and quadrupole interactions, the nuclear charge distribution is divided into a spherically symmetric part $\rho_0(r)$ and a part $\rho_2(r)$ describing the quadrupole distribution in the nuclear frame as [73]

$$\rho(\mathbf{r}') = \rho_0(r') + \rho_2(r')\, Y_{20}(\vartheta', \varphi'), \tag{2.7}$$

with the spherical harmonics $Y_{lm}(\vartheta, \varphi)$. Since an analogous part for the dipole distribution would be an operator of odd parity, it would vanish after averaging with muon wave functions of defined parity [182], and thus it is not considered here and neither are higher multipoles beyond the quadrupole term. Correspondingly, the electric potential from Eq. (2.3) contains only the monopole and quadrupole part, and can be written as

$$V_{\mathrm{el}}(\mathbf{r}_\mu, \phi, \theta) = V_{\mathrm{el}}^{(0)}(r_\mu) + V_{\mathrm{el}}^{(2)}(\mathbf{r}_\mu, \phi, \theta), \tag{2.8}$$

where the spherically symmetric part of the charge distribution can be written as

$$V_{\mathrm{el}}^{(0)}(r_\mu) = -4\pi Z \alpha \int_0^\infty \mathrm{d}r\, r^2 \frac{\rho_0(r)}{r_>}, \tag{2.9}$$

with $r_> = \max(r, r_\mu)$. This interaction potential will be included in the numerical solution of the Dirac equation for the muon as described in Section 2.1.3.1. The quadrupole part of the interaction $V_{\mathrm{el}}^{(2)}$ causes hyperfine splitting, which is calculated in Section 2.1.4.

The appropriate states have well-defined angular momentum, as introduced in Eq. (2.6). As a basis for further calculations, the Dirac equation

$$\left(\boldsymbol{\alpha} \cdot \mathbf{p} + \beta + V_{\mathrm{el}}^{(0)}(r_\mu) \right) |n\kappa m\rangle = (1 - E_{n\kappa}^{(B)}) |n\kappa m\rangle \tag{2.10}$$

is solved for the muon. Here, $E_{n\kappa}^{(B)}$ are the binding energies, and the potential $V_{\mathrm{el}}^{(0)}(r_\mu)$ is the spherically symmetric part of the interaction with the nucleus. This is the monopole contribution from the electric interaction in Eq. (2.9) and, if vacuum polarization is considered, the Uehling potential from Eq. (2.13). A Fermi type charge distribution [126]

is used to model the monopole charge distribution as

$$\rho_0(r) = N \left[1 + \exp\left(\frac{r - c}{a} \right) \right]^{-1}, \tag{2.11}$$

where a is a skin thickness parameter and c the half-density radius. The normalization constant N is chosen such that the volume integral is equal to one, since the charge is already included in the fine-structure constant. It has been proven, that $a = t/(4\log 3)$, with $t = 2.30\,\mathrm{fm}$, is a good approximation for most of the nuclei [126]. The parameter c is then determined by demanding, that the charge radius squared

$$\left\langle r^2 \right\rangle = \frac{\int \mathrm{d}r\, r^4 \rho_0(r)}{\int \mathrm{d}r\, r^2 \rho_0(r)}$$

agrees with the values from the literature [178]. Since the potential in Eq. (2.10) is spherically symmetric, the angular part can be separated and the solution can be written in terms of the spherical spinors $\Omega_{\kappa m}(\vartheta, \varphi)$ from Eqs. (1.18), (1.19) as [42]

$$|n\kappa m\rangle = \frac{1}{r} \begin{pmatrix} G_{n\kappa}(r)\, \Omega_{\kappa m} \\ i\, F_{n\kappa}(r)\, \Omega_{-\kappa m} \end{pmatrix}.$$

The remaining equations for the radial functions are solved with the dual-kinetic-balance method [152] to obtain $G_{n\kappa}$ and $F_{n\kappa}$, and the corresponding eigenenergies $E_{n\kappa}$ numerically.

In Table 2.2, the binding energies for muonic $^{205}_{83}\mathrm{Bi}$, $^{147}_{62}\mathrm{Sm}$, and $^{89}_{40}\mathrm{Zr}$ are shown, where the finite nuclear size effect is illustrated by also including the binding energies $E^{(C)}_{n\kappa}$ from Eq. (1.22) of the pure Coulomb potential $-Z\alpha/r_\mu$, which read [42]

$$E^{(C)}_{n\kappa} = 1 - \left(1 + \frac{(Z\alpha)^2}{\left(n - |\kappa| + \sqrt{\kappa^2 - (Z\alpha)^2} \right)^2} \right)^{-\frac{1}{2}}. \tag{2.12}$$

Furthermore, the corrections from the Uehling potential in Eq. (2.13) are shown separately. The uncertainties include the error in the tabulated RMS radius value as well as a model error, which is estimated via the difference of the binding energies with the Fermi potential from Eq. (2.11) and the potential of a charged sphere with the same RMS radius. For heavy nuclei, the finite nuclear size correction can amount up to 50 %, and thus the binding energy is halved.

2.1.3.2 Vacuum polarization in Uehling approximation

For atomic electrons, there are two QED corrections of the order α, namely the self-energy (SE) QED and the vacuum polarization (VP) correction [126], which usually contribute equally. For muons, however, the VP correction is much larger due to virtual electron-positron pairs, which are less suppressed due to the small electron-to-muon mass ratio [83]. The spherically symmetric part of the VP to first order in α and $Z\alpha$ is the

Uehling potential [162]

$$V_{\text{Uehl}}(r_\mu) = -\alpha \frac{2\alpha}{3\pi} \int_0^\infty \mathrm{d}r' \, 4\pi\rho_0(r') \int_1^\infty \mathrm{d}t \left(1 + \frac{1}{2t^2}\right)$$

$$\times \frac{\sqrt{t^2-1}}{t^2} \frac{\exp(-2m_e|r_\mu - r'|t) - \exp(-2m_e(r_\mu + r')t)}{4m_e r_\mu t}, \qquad (2.13)$$

where m_e is the electron mass and ρ_0 is the spherically symmetric part of the charge distribution from Eq. (2.7). This potential can be directly added to the Dirac equation (2.10). In this way, all iterations of the Uehling potential are included [167]. Results for our calculations can be found in Table 2.2.

2.1.3.3 Recoil corrections

Taking into account the finite mass and the resulting motion of the nucleus leads to recoil corrections to the bound muon energy levels. In nonrelativistic quantum mechanics, as in classical mechanics, the problem of describing two interacting particles can be reduced to a one particle problem by using the reduced mass m_r of the muon-nucleus system [183]. With the mass of the nucleus m_N, the reduced mass reads in the chosen system of units as

$$m_r = \frac{m_N}{m_N + 1}, \qquad (2.14)$$

and the Dirac equation is accordingly modified to

$$\left(\boldsymbol{\alpha} \cdot \mathbf{p} + \beta \, m_r + V_{\text{el}}^{(0)}(r_\mu)\right) |n\kappa m\rangle = (m_r - E_{n\kappa}^{(B)}) |n\kappa m\rangle.$$

In relativistic quantum mechanics, this separation is not possible. We follow an approach used in Refs. [83, 184], which includes the nonrelativistic part of the recoil correction already in the wave functions by using the reduced mass in the Dirac equation and calculating the leading relativistic corrections perturbatively. If $E_{n\kappa}^{(\text{fm})}$ denotes the binding energy of Eq. (2.10) with the finite size potential from Eq. (2.9), but with the reduced mass replaced by the full muon rest mass, and $E_{n\kappa}^{(\text{rm})}$ the binding energy in the same potential but with the reduced mass from Eq. (2.14), then the leading relativistic recoil correction $\Delta E_{n\kappa}^{(\text{rec,rel})}$ according to Ref. [83] reads

$$\Delta E_{n\kappa}^{(\text{rec,rel})} = -\frac{\left(E_{n\kappa}^{(\text{fm})}\right)^2}{2M_N} + \frac{1}{2M_N} \left\langle h(r) + 2E_{n\kappa}^{(\text{fm})} P_1(r) \right\rangle,$$

where M_N is the mass of the nucleus, and the functions $h(r)$ and $P_1(r)$ are defined in Eqs. (109) and (111) of Ref. [83], respectively. In Table 2.3, the binding energies obtained by solving the Dirac equation with the muon rest mass and the reduced mass of the muon-nucleus system are compared. Furthermore, the leading relativistic recoil correction is shown. The uncertainties include errors in the RMS radius, the model of the charge distribution and for the relativistic recoil, and a $(m_\mu/M_N)^2$ term due to higher-order corrections in the mass ratio of muon and nucleus, which dominates the uncertainty for

lower Z.

2.1.3.4 Interaction with atomic electrons

The effect of the surrounding electrons on the binding energies of the muon is commonly referred to as electron screening and was estimated following Ref. [185] by calculating an effective screening potential from the charge distribution of the electrons as

$$V_e(\mathbf{r}_\mu) = -\alpha \int \mathrm{d}^3\mathbf{r}\,\frac{\rho_e(\mathbf{r})}{|\mathbf{r}_\mu - \mathbf{r}|}, \tag{2.15}$$

and using this potential in the Dirac equation for the muon. The charge distribution of the electrons is obtained by their Dirac wave functions as $\rho_e(\mathbf{r}) = \sum_i \psi_{e_i}^*(\mathbf{r}) \cdot \psi_{e_i}(\mathbf{r})$, where $\psi_{e_i}(\mathbf{r})$ is the four component spinor of the i-th considered electron. In order to obtain the wave functions of the electrons, it has to be taken into account, that the muon essentially screens one unit of charge from the nucleus. The simplest possibility is to replace the nuclear charge by an effective charge $\tilde{Z} = Z - 1$ and then solve the Dirac equation for the electron with this modified nuclear potential. Another possibility is to start solving the Dirac equation for the muon in the nuclear potential without electron screening. Then, the Dirac equation for the electron is solved for all required states, with the screening potential due to the bound muon

$$V_\mu(\mathbf{r}_e) = -\alpha \int \mathrm{d}^3\mathbf{r}\,\frac{\psi_\mu^*(\mathbf{r}) \cdot \psi_\mu(\mathbf{r})}{|\mathbf{r}_e - \mathbf{r}|},$$

analogously to Eq. (2.15). The interaction between the electrons is not taken into account here. Finally, the Dirac equation for the muon is solved again, now including the nuclear potential and the screening potential (2.15) due the atomic electrons from the considered electron configuration. This procedure can be repeated in the spirit of Hartree's method [186] until the electrons and the muon are self-consistent in the fields of each other. Our studies show that one iteration is usually enough since the overlap of muon and electron wave functions in heavy muonic atoms is small. It is important to note, that here the screening potential depends to a small extent on the state of the muon, since the muon wave function is used in the calculation for the electron wave function. The atomic electrons primarily behave like a charged shell around the muon and the nucleus; thus every muon level is mainly shifted by a constant term, which is not observable in muonic transitions. The correction ΔE_S is defined as the difference of the binding energy without and with screening potential, respectively. Therefore, a positive value indicates that the muon is less bound due to the screening effect. The main contribution to the nonconstant part of the screening potential comes from the $1s$ electrons, since their wave functions have the biggest overlap with the muon; therefore the exact electron configuration has only a minor effect on transition energies [185]. In Table 2.4, results for the screening correction are shown for both mentioned methods and for different electron configurations. Values of the screening correction for different electron configurations show that a 10% error for the non-constant part is a reasonable estimate.

2.1.3.5 Electric quadrupole splitting

Since for heavy nuclei the nuclear radius is comparable to the muon's Compton wavelength [91, 178], the muonic wavefunction overlaps strongly with the nucleus and the muon is sensitive to nuclear shape corrections, which results in hyperfine splitting of the energy levels. The quadrupole part of the electric interaction (2.8) can be rewritten as [187]

$$V_{\mathrm{el}}^{(2)}(\mathbf{r}_\mu, \theta, \phi) = -\alpha \frac{Q_0 F_{\mathrm{QD}}(r_\mu)}{2\, r_\mu^3} \sum_{m=-2}^{2} C_{2m}(\theta, \phi) C_{2m}^*(\vartheta_\mu, \varphi_\mu), \tag{2.16}$$

where $C_{lm}(\vartheta, \varphi) = \sqrt{4\pi/(2l+1)} Y_{lm}(\vartheta, \varphi)$ and angles with a subscript μ describe the position of the muon in the laboratory frame. Here, the nuclear intrinsic quadrupole moment is defined via the charge distribution from Eq. (2.7) as

$$Q_0 = 2\sqrt{\frac{4\pi}{5}} \int_0^\infty r^4 \rho_2(r)\, \mathrm{d}r, \tag{2.17}$$

and the distribution of the quadrupole moment is described by the function $F_{\mathrm{QD}}(r_\mu)$, with the point-like limit $F_{\mathrm{QD}}(r_\mu) = 1$. For the shell model, where the quadrupole distribution is concentrated around the nuclear RMS radius R_N, the divergence for $r_\mu = 0$ is removed, and the corresponding quadrupole distribution function is

$$F_{\mathrm{QD}}(r_\mu) = \begin{cases} (r_\mu/R_N)^5 & r_\mu \le R_N \\ 1 & r_\mu > R_N \end{cases}. \tag{2.18}$$

Formally, this corresponds to a charge distribution with

$$\rho_2(r_\mu) = \frac{Q_0}{2}\sqrt{\frac{5}{4\pi}} \frac{\delta(r_\mu - R_N)}{R_N^4}. \tag{2.19}$$

The matrix elements of the quadrupole interaction from Eq. (2.16) in the states (2.6) read [188]

$$\langle FM_F I\kappa | H_E^{(2)} | FM_F I\kappa \rangle = -\alpha(-1)^{j+I+F} \begin{Bmatrix} j & I & F \\ I & j & 2 \end{Bmatrix} \tag{2.20}$$

$$\times \langle I|| \frac{Q_0}{2}\widehat{C}_2(\vartheta_N, \varphi_N) ||I\rangle \langle n\kappa|| \frac{F_{\mathrm{QD}}(r_\mu)}{r_\mu^3}\widehat{C}_2(\vartheta_\mu, \varphi_\mu) ||n\kappa\rangle.$$

The reduced matrix element in the nuclear coordinates can be expressed with the spectroscopic nuclear quadrupole moment Q as

$$\langle I|| \frac{Q_0}{2}\widehat{C}_2(\vartheta_N, \varphi_N) ||I\rangle = Q\sqrt{\frac{(2I+3)(2I+1)(I+1)}{4I(2I-1)}},$$

and the reduced matrix elements in the muonic coordinates are

$$\langle n\kappa || f(r_\mu)\widehat{C}_2(\vartheta_\mu, \varphi_\mu) || n\kappa \rangle = \tag{2.21}$$

$$-\sqrt{\frac{(2j+3)(2j+1)(2j-1)}{16j(j+1)}} \int_0^\infty \left(G_{n\kappa}^2(r_\mu) + F_{n\kappa}^2(r_\mu) \right) \frac{F_{\text{QD}}(r_\mu)}{r_\mu^3} \mathrm{d}r_\mu.$$

The values for the nuclear RMS radii R_N and the spectroscopic quadrupole moments Q are taken from Refs. [178, 189]. In Table 2.5, results for the electric quadrupole hyperfine splitting for the nuclei $^{205}_{83}\text{Bi}$, $^{147}_{62}\text{Sm}$, and $^{89}_{40}\text{Zr}$ are shown for a selection of hyperfine states, with uncertainties stemming from the error in the quadrupole moment and an estimation of the modeling uncertainty, which was estimated by using quadrupole distributions of the form

$$\tilde{\rho}_2(r_\mu) = \begin{cases} \rho_0 \, r_\mu^n, & r_\mu \leq R_N; \\ 0, & r_\mu > R_N \end{cases}$$

for different n instead of Eq. (2.19). Here, ρ_0 is chosen such that Eq. (2.17) is fulfilled. This leads to the quadrupole distributions

$$\tilde{F}_{\text{QD}}(r_\mu) = \begin{cases} (r_\mu/R_N)^5 \left[\frac{n+5}{n} - \frac{5}{n} \left(\frac{r_\mu}{R_N} \right)^n \right], & r_\mu \leq R_N; \\ 1, & r_\mu > R_N \end{cases}$$

and Eq. (2.18) is formally the limit for large n.

2.1.3.6 Magnetic dipole splitting

As for the magnetic part, dipole interaction is considered. Therefore, the corresponding interaction Hamiltonian reads [162]

$$H_M = \frac{|e|}{4\pi} \boldsymbol{\mu} \cdot \left(F_{\text{BW}}(r) \frac{\mathbf{r}}{r^3} \times \boldsymbol{\alpha} \right), \tag{2.22}$$

with the charge of the muon $e = -|e|$, the nuclear magnetic moment $\boldsymbol{\mu}$, its distribution function F_{BW}, and the Dirac matrices $\boldsymbol{\alpha}$. The difference in the hyperfine splitting between a point-like magnetic moment and a spatial distribution of the magnetization is called the Bohr-Weisskopf effect [190]. In the following, the diagonal matrix elements of the magnetic interaction are analyzed, paying special attention to the distribution function F_{BW}. We expect the contribution of the higher-order terms, namely electric octupole, magnetic quadrupole, and beyond, to be smaller than the uncertainty of the considered terms [84, 191]. Therefore they can be ignored here.

The hyperfine splitting arises from the interaction of the nuclear magnetic moment with the muon's magnetic moment, which is also sensitive to the spatial distribution of the nuclear currents. Since the magnetic moment of the muon is inversely proportional to its mass, the magnetic hyperfine splitting in muonic atoms is less important than in electronic atoms. The matrix elements of the corresponding Hamiltonian (2.22) in the

state (2.6) are [188]

$$\langle FM_F I\kappa| \, H_M \, |FM_F I\kappa\rangle = \; [F(F+1) - I(I+1) - j(j+1)] \tag{2.23}$$

$$\times \frac{\alpha}{2m_p} \frac{\mu}{\mu_N} \frac{\kappa}{Ij(j+1)} \int_0^\infty \frac{G_{n\kappa}(r_\mu) F_{n\kappa}(r_\mu) F_{\mathrm{BW}}(r_\mu)}{r_\mu^2} \mathrm{d}r_\mu,$$

where m_p is the proton mass, and the ratio of the observed magnetic moment $\mu := \langle II| \, (\boldsymbol{\mu})_z \, |II\rangle$ and the nuclear magneton μ_N can be found in the literature [189]. For the simple model of a homogeneous nuclear current, the distribution function of the Bohr-Weisskopf effect reads

$$F_{\mathrm{BW}}(r_\mu) = \begin{cases} (r_\mu/R_N)^3 & r_\mu \leq R_N \\ 1 & r_\mu > R_N \end{cases}.$$

Furthermore, an additional method is used to obtain the distribution function F_{BW} from the nuclear single particle model, where the nuclear magnetic moment is assigned to the odd nucleon and the Schrödinger equation for this nucleon is solved in the Woods-Saxon potential of the other nucleons [162]. In Table 2.5, results for the magnetic dipole hyperfine splitting for the nuclei $^{205}_{83}\mathrm{Bi}$, $^{147}_{62}\mathrm{Sm}$, and $^{89}_{40}\mathrm{Zr}$ are presented for a selection of hyperfine states, using both methods for obtaining F_{BW}, where the model error is estimated by the difference of these two methods and the uncertainty in the magnetic moment is also taken into account.

2.1.4 Dynamical hyperfine structure

In this subsection, the hyperfine structure of muonic atoms is discussed in detail. In electronic systems, the energy splitting due to hyperfine interactions is usually calculated in first order perturbation theory. This is not enough for the correct prediction of the level structure of heavy muonic atoms. There are two reasons for this:

Firstly, the fine-structure splitting between states of the same parity, especially between the $2p_{1/2}$ and $2p_{3/2}$ states, is up to the energy scale of a few hundred keV. On the other hand, the first order energy correction due to the electric quadrupole interaction can also be on the order of 100 keV in the $2p_{3/2}$ states. It should be noted that the expectation value of the quadrupole interaction in the $2p_{1/2}$ states vanishes because of angular momentum selection rules. The quadrupole interaction is represented as a rank 2 tensor operator, thus the sum of the involved angular momenta must also be larger than or equal to 2. This is not the case for the expectation value of the $2p_{1/2}$ states with $j = 1/2$. There are, however, also the non-diagonal matrix elements with one $2p_{1/2}$ and one $2p_{3/2}$ states, which are also on the hundred keV level for high Z muonic atoms. If the quadrupole hyperfine structure is only calculated in first order perturbation theory, these non-diagonal elements are not considered. Since the separation between the two unperturbed states ($2p_{1/2}$ and $2p_{3/2}$) is on the same level as the non-diagonal matrix elements, first order perturbation theory is not sufficient. As a consequence, the non-diagonal matrix elements have to be taken into account. One possibility would be to use higher order perturbation theory, which involves a sum over the complete muonic

spectrum. However, already the consideration of the non-diagonal matrix elements for a muonic fine-structure doublet can explain the majority of the higher order effects. Therefore, the formalism of quasi-degenerate perturbation theory [192] is useful, and the general approach will be briefly reviewed in the following section. Here, the quadrupole interaction is rediagonalized in finite-dimensional subspaces by only using a small number of muonic states.

Secondly, the energy scale of the fine structure and electric quadrupole splitting is on the same scale as the typical excitation energy of the excited nuclear states in the rotational ground state band. In addition, the nuclear states in the ground state rotational band have the same parity and thus are coupled to each other by the quadrupole interaction. This means that the expectation value of the quadrupole operator is generally non-zero, also for the case of different nuclear rotational states. As a consequence, the excited nuclear states have to be taken into account when rediagonalizing the quadrupole interaction in finite-dimensional subspaces as mentioned above.

2.1.4.1 Quasi-degenerate perturbation theory

In this section, the general approach to quasi-degenerate perturbation theory is briefly reviewed, following [83, 192], before it will be applied to muonic atoms in the following sections. For simplicity, a system with unperturbed eigenstates $|n\rangle$ and corresponding unperturbed energies $\mathcal{E}_n$ is investigated. The corresponding eigenvalue equation is

$$H_0 |n\rangle = \mathcal{E}_n |n\rangle ,$$

where H_0 is the unperturbed Hamiltonian. Now, a perturbation H_1 is considered. The connection to the muonic atom case can be made by considering $|n\rangle$ as a multi-index for all the quantum numbers of the muonic atom and using the quadrupole interaction for the perturbation H_1. The perturbed eigenvalue equation reads

$$(H_0 + H_1) |a\rangle = E_a |a\rangle . \tag{2.24}$$

If m different states $|n_i\rangle$ are almost degenerate, their energy separation is on the same order as the first order correction due to H_1. In this case, the corresponding modelspace is defined as all $|n_i\rangle$ with $i = 1, ..., m$, if necessary the states have to be relabeled, such that the lowest indices correspond to the states defining the model space. The projector P on the modelspace is defined by acting on an eigenstate $|a\rangle = \sum_n a_n |n\rangle$ of Eq. (2.24) as

$$P |a\rangle = \sum_{i=1}^{m} a_i |n_i\rangle ,$$

thus considering only the states inside of the modelspace. Analogously, the projector Q is defined as the complement, i.e. keeping only coefficients of states outside of the modelspace. Thereby, it holds that $P + Q = \mathbb{1}$ and the following relations [83] can be derived

for eigenstates of the total Hamiltonian from Eq. (2.24):

$$Q \ket{a} = -(H_0 - E_a)^{-1} Q H_1 \ket{a} \, ,$$
$$(H_0 - E_a + P H_1) P \ket{a} = -P H_1 Q \ket{a} \, .$$

A combination of these two equations results in

$$P \left((H_0 - E_a + H_1) P \ket{a} - H_1 (H_0 - E_a)^{-1} Q H_1 \ket{a} \right) = 0, \qquad (2.25)$$

which can be expanded in Q. Thereby, states outside of the finite dimensional modelspace can be treated systematically. The zero-order term is obtained by neglecting the term containing a Q operator:

$$P (H_0 + H_1 - E_a) P \ket{a} = 0. \qquad (2.26)$$

This is essentially Eq. (2.24), but projected on the modelspace. To zeroth order in the projection operator Q, the states outside of the modelspace can be neglected. Since this is a finite-dimensional system, an exact solution can be obtained by diagonalization of the Hamiltonian matrix.

When applied to muonic atoms, the unperturbed Hamiltonian is the sum of a rigid rotor Hamiltonian for the nucleus and Dirac Hamiltonian with the monopole potential for the muon. The perturbation is the hyperfine (mainly quadrupole) interaction. Then, a modelspace needs to be chosen, for example the first few nuclear rotational states and a muonic fine-structure doublet like the $(2p_{1/2}, 2p_{3/2})$ or $(3d_{3/2}, 3d_{5/2})$ states. Finally, the diagonal and non-diagonal matrix elements of the hyperfine interactions need to be calculated for all states in the modelspace and the matrix representation of the total Hamiltonian in the modelspace has to be diagonalized.

The solution of Eq. (2.26) results in an approximation for the eigenstates of the full Hamiltonian as

$$\ket{a^{(0)}} = \sum_{i=1}^{m} a_i^{(0)} \ket{n_i} \, , \qquad (2.27)$$

which is a linear combination of the unperturbed states forming the modelspace with the coefficients obtained from the diagonalization of the Hamiltonian matrix. The corresponding eigenvalues are the approximations $E_a^{(0)}$ of the eigenenergy.

Eq. (2.25) is used for the leading order corrections due to the operator Q, including the Q-dependent term. However, only the effect on the modelspace is investigated, corresponding to the approximation $\ket{a} \approx P \ket{a}$. Using the property of a projection operator $P^2 = P$, Eq. (2.25) can be written as

$$\underbrace{P(H_0 + H_1 - E_a)P}_{\tilde{H}_0} + \underbrace{P(H_1(E_a - H_0)^{-1} Q H_1)P}_{\tilde{H}_1} \ket{a} = 0,$$

which takes the form of an eigenvalue problem with the unperturbed Hamiltonian $\tilde{H}_0$ and the perturbation $\tilde{H}_1$. Because of P on the left and right side, this is a finite dimensional problem, although each matrix element of $\tilde{H}_1$ involves a summation over the complete spectrum as shown below. The unperturbed solutions are given by Eq. (2.27). Thereby,

the energy correction due to the perturbation $\tilde{H}_1$ can be calculated within first order perturbation theory as

$$E_a^{(1)} = \left\langle a^{(0)} \middle| \tilde{H}_1 \middle| a^{(0)} \right\rangle \tag{2.28}$$

$$= \sum_{k>m} \frac{\left\langle a^{(0)} \middle| H_1 \middle| n_k \right\rangle \left\langle n_k \middle| H_1 \middle| a^{(0)} \right\rangle}{E_a^{(0)} - \mathcal{E}_{n_k}}$$

$$= \sum_{i,j=1}^{m} a_i^{(0)\,*} a_j^{(0)} \sum_{k>m} \frac{\left\langle n_i \middle| H_1 \middle| n_k \right\rangle \left\langle n_k \middle| H_1 \middle| n_j \right\rangle}{E_a^{(0)} - \mathcal{E}_{n_k}},$$

where the projector on states outside of the modelspace is formally written as $Q = \sum_{k>m} |n_k\rangle \langle n_k|$. If there are continuous parts in the spectrum, this sum also involves integrals. Once the zeroth order energies and states are found by diagonalizing the Hamiltionian in the modelspace, the first order energy correction due to states outside of the modelspace is calculated by calculating the second order energy correction due to the original perturbation H_1, but the intermediate sum only involves states not contained in the modelspace, i.e. those not already considered in the diagonalization. As a result, the sum $E_a = E_a^{(0)} + E_a^{(1)}$ contains a complete second order treatment of the perturbation H_1, and additionally the contributions of the states in the modelspace to all orders.

For actual calculations in the context of muonic atoms, these computations are very time-consuming for the following reasons: Already the unperturbed Hamiltonian involves a numerical solution of the Dirac equation with an extended nuclear monopole potential. The diagonal and non-diagonal matrix elements of the electric quadrupole interaction have to be calculated via numerical integration as well, before diagonalizing the total Hamiltonian. Since finite-basis-set methods [152] are used in this thesis for solving the Dirac equation, a numerical, discrete representation of the complete muonic spectrum is obtained. Therefore numerical evaluations of Eq. (2.28) without approximations is possible in the framework of this thesis.

In the following sections, the approach of quasi-degenerate perturbation theory from Section 2.1.4.1 will be applied to muonic atoms considering electric monopole and quadrupole interaction, as well as magnetic dipole interaction. The starting point is a given deformed nuclear charge distribution $\rho(\mathbf{r})$ and a distribution of the static currents $\mathbf{j}(\mathbf{r})$ inside the nucleus. The necessary steps are the following:

- definition of the unperturbed and perturbed Hamiltonian

- calculation of the potentials starting from the given charge and current distribution

- solve the Dirac equation with the electric monopole potential

- definition of modelspaces

- calculation of diagonal and non-diagonal matrix elements of the hyperfine operators in the modelspace and rediagonalization

- calculation of energy correction due to states outside of the modelspace

2.1.4.2 Non-diagonal elements of hyperfine interactions

The unperturbed Hamiltonian for the muonic atom is already given by Eq. (2.4) for the nucleus and in Eq. (2.5) for the muon in terms of the nuclear charge distribution $\rho(\mathbf{r})$. The corresponding states of defined total angular momentum F are given in Eq. (2.6). The next step for the calculation of the hyperfine structure of muonic atoms in the framework of quasi-degenerate perturbation theory is the computation of the diagonal and non-diagonal matrix elements of the electric quadrupole and magnetic dipole interactions.

The multipole expansion of the electric potential in Eq. (2.3) can be used to express the electric quadrupole interaction energy in terms of the nuclear charge distribution. The quadrupole terms with $l = 2$ is

$$
V_{\text{el}}^{(2)}(\mathbf{r}_\mu, \phi, \theta) = -Z\alpha \left[\int \mathrm{d}^3 \mathbf{r}_N' \frac{\min(r_N, r_\mu)^2}{\max(r_N, r_\mu)^3} \mathrm{P}_2(\cos\vartheta_N')\rho(\mathbf{r}_N') \right] \sum_{m=-2}^{2} \mathrm{C}_{2m}^*(\theta, \phi)\mathrm{C}_{2m}(\vartheta_\mu, \varphi_\mu).
$$
(2.29)

As a next step, the matrix element of (2.29) with two arbitrary states from Eq. (2.6) is considered, which reads as

$$
\Delta E^{(2)} = \left\langle F_1 M_1\, I_1 K\, n_1\kappa_1 \middle| V_{\text{el}}^{(2)} \middle| F_2 M_2\, I_2 K\, n_2\kappa_2 \right\rangle.
$$
(2.30)

With the relation $\mathrm{C}_{lm}^*(\vartheta, \varphi) = (-1)^m \mathrm{C}_{l(-m)}(\vartheta, \varphi)$, and fact that the normalized spherical harmonic are irreducible tensor operators as introduced in Appendix A.3, the sum in Eq. (2.29) is a scalar product of two rank-2 irreducible tensors. Therefore, Eq. (A.13) can be used to rewrite the matrix element from Eq. (2.30) in terms of the reduced matrix elements of the spherical harmonics as

$$
\Delta E^{(2)} = -\, Z\alpha\delta_{F_1 F_2}\delta_{M_1 M_2}(-1)^{F+I_2+j_1} \begin{Bmatrix} I_1 & I_2 & 2 \\ j_2 & j_1 & F \end{Bmatrix} \langle I_1 K \| \mathrm{C}_2 \| I_2 K \rangle
$$

$$
\times \left\langle n_1\kappa_1 \middle\| \mathrm{C}_2 \int \mathrm{d}^3 \mathbf{r}_N' \frac{r_<^2}{r_>^3}\mathrm{P}_2(\cos\vartheta_N')\rho(\mathbf{r}_N') \middle\| n_2\kappa_2 \right\rangle,
$$
(2.31)

where it is useful to define

$$
f_Q(r_\mu)/r_\mu^3 := \int \mathrm{d}^3 \mathbf{r}_N' \frac{r_<^2}{r_>^3}\mathrm{P}_2(\cos\vartheta_N')\rho(\mathbf{r}_N'),
$$
(2.32)

since for the approximation of a point-like quadrupole moment or generally for large r_μ it holds that $f_Q(r_\mu) = 1$, and thus the usual r_μ^{-3} radial integral for quadrupole hyperfine structure is recovered. Accordingly, $f_Q(r_\mu)$ describes the finite distribution of the quadrupole moment inside the nucleus. The reduced matrix element in the nuclear coordinates can be calculated with the rigid rotor wave functions from Appendix A.4 and the definition of the reduce matrix element from Eq. (A.10). It is given in Eq. (A.17)

and reads

$$\langle I_1 K || C_l || I_2 K \rangle = (-1)^{I_2 + K} \sqrt{(2I_1 + 1)(2I_2 + 1)} \begin{pmatrix} I_1 & I_2 & l \\ -K & K & 0 \end{pmatrix}.$$

The reduced matrix elements in the muonic variables can be evaluated as [182]

$$\langle n_1 \kappa_1 || f(r_\mu) C_l(\vartheta_\mu, \varphi_\mu) || n_2 \kappa_2 \rangle = (-1)^{j_1 + 1/2} \sqrt{(2j_1 + 1)(2j_2 + 1)}$$

$$\times \begin{pmatrix} j_1 & j_2 & l \\ -\frac{1}{2} & \frac{1}{2} & 0 \end{pmatrix} \pi(l_1 + l_2) \int dr (g_{n_1\kappa_1}(r_\mu) g_{n_2\kappa_2}(r_\mu) + f_{n_1\kappa_1}(r_\mu) f_{n_2\kappa_2}(r_\mu)) f(r_\mu),$$

where $f_{n\kappa}(r_\mu)$ and $g_{n\kappa}(r_\mu)$ are the radial wave functions (1.20) obtained by solving the Dirac equation (2.4). The function

$$\pi(n) = \begin{cases} 1, & n \text{ even}; \\ 0, & \text{otherwise} \end{cases} \tag{2.33}$$

represents the parity selection rules. Thus, the evaluation of a single reduced muonic matrix element requires one numerical integration, and for every calculation of $f_Q(r_\mu)$ therein, another numerical integration of Eq. (2.32) has to be performed.

In the following, the matrix elements of the magnetic hyperfine structure will be calculated for diagonal elements, and for non-diagonal matrix elements in the framework of the rigid rotor nuclear model, following the analysis in Ref. [191]. The magnetic Hamiltonian due to the vector potential $\mathbf{A}_N$ caused by the nuclear static currents in the nuclear body fixed frame reads

$$H_M(\mathbf{r}_\mu) = |e| \, \boldsymbol{\alpha} \cdot \mathbf{A}_N(\mathbf{r}_\mu),$$

where the vector potential is generated by the static currents in the nucleus, and the connection reads [180]

$$\mathbf{A}_N(\mathbf{r}_\mu) = \frac{1}{4\pi} \int d^3r' \frac{\mathbf{j}(\mathbf{r}')}{|\mathbf{r}_\mu - \mathbf{r}'|}.$$

For extended nuclei without a divergence at the origin the current distribution can be expressed in terms of the curl of another vector field, since the divergence of the current distribution in the static case is zero [180]. This field is called magnetization $\mathbf{M}(\mathbf{r})$ and the connection between current distribution and magnetization is

$$\mathbf{j}(\mathbf{r}) = \boldsymbol{\nabla} \times \mathbf{M}(\mathbf{r}).$$

The restriction to magnetic dipole interactions is done by writing the magnetization as

$$\mathbf{M}(\mathbf{r}) = \boldsymbol{\mu} f(r) = \mu \mathbf{e}'_z f(r),$$

where $\boldsymbol{\mu}$ is the nuclear magnetic dipole operator and μ its absolute value. The second equality follows from the fact, that the symmetric rigid rotor model is used and the magnetic moment has to be aligned with the nuclear body fixed z-axis $\mathbf{e}'_z$. Otherwise,

axial symmetry would be violated. In Cartesian coordinates in the laboratory system, the basis vector $\mathbf{e}'_z$ of the body fixed system reads as

$$\boldsymbol{\mu}(\theta, \phi) = |\boldsymbol{\mu}| \begin{pmatrix} \sin\theta\cos\phi \\ \sin\theta\sin\phi \\ \cos\theta \end{pmatrix}. \tag{2.34}$$

The scalar function $f(r)$ describes the finite distribution of the dipole moment in the nucleus, which is responsible for the Bohr-Weisskopf effect [190] and is normalized as

$$4\pi \int_0^\infty \mathrm{d}r\, r^2\, f(r) = 1.$$

Thereby, the magnetic Hamiltonian can be written as

$$\mathrm{H}_M(\mathbf{r}_\mu, \theta, \phi) = \frac{|e|}{4\pi} \boldsymbol{\mu}(\theta, \phi) \cdot \left(F_{\mathrm{BW}}(r) \frac{\mathbf{r}}{r^3} \times \boldsymbol{\alpha} \right), \tag{2.35}$$

and the function $F_{\mathrm{BW}}(r)$ is connected to the distribution function $f(r)$ via

$$F_{\mathrm{BW}}(r) = -4\pi r^2 \partial_r \left(\int_0^\infty \mathrm{d}r'\, \frac{r'^2 f(r')}{\max(r, r')} \right).$$

The magnetic dipole Hamiltonian from Eq. (2.35) can be written as a scalar product of two rank-1 irreducible tensor operators acting on the muonic and nuclear coordinates, respectively, as [182]

$$\mathrm{H}_M(\mathbf{r}_\mu, \theta, \phi) = \sum_{\lambda=-1}^{1} (-1)^\lambda\, d_\lambda(\mathbf{r}_\mu)\; \mu_{-\lambda}(\theta, \phi),$$

$$d_\lambda(\mathbf{r}_\mu) = \frac{-i\sqrt{2}|e|}{4\pi} \left(\boldsymbol{\alpha} \cdot \mathbf{C}_{1\lambda}^{(0)}(\vartheta_\mu, \varphi_\mu) \right) \frac{F_{\mathrm{BW}}(r_\mu)}{r_\mu^2},$$

where $\mathbf{C}_{bc}^{(a)}(\vartheta, \varphi)$ are the vector spherical harmonics [168, Section 7.] and μ_λ are the spherical components with $\lambda = 0, \pm 1$ [168, Section 1.] of the magnetic moment operator from Eq. (2.34). Correspondingly, Eq. (A.13) can be used for the calculation of the expectation value, and the result is

$$\langle F_1 M_1\, I_1 K\, n_1 \kappa_1 | \mathrm{H}_M | F_2 M_2\, I_2 K\, n_2 \kappa_2 \rangle = \delta_{F_1 F_2} \delta_{M_1 M_2} (-1)^{F_1 + j(\kappa_2) + I_1}$$

$$\times \begin{Bmatrix} j(\kappa_1) & j(\kappa_2) & 1 \\ I_2 & I_1 & F_1 \end{Bmatrix} \langle n_1\kappa_1 || \mathbf{d} || n_2\kappa_2 \rangle \langle I_1 K || \boldsymbol{\mu} || I_2 K \rangle.$$

The reduced matrix elements of the nuclear magnetic moment operator can be obtained with literature values of the magnetic moment from [189] and with Eq. (A.17), using the relation

$$\langle IK || \boldsymbol{\mu} || IK \rangle = |\boldsymbol{\mu}|\, \langle IK || C_1 || IK \rangle.$$

The reduced muonic matrix elements can be evaluated as [182]

$$
\begin{aligned}
\langle n_1\kappa_1||\mathbf{d}||n_2\kappa_2\rangle = & -\frac{|e|}{4\pi}(\kappa_1+\kappa_2)(-1)^{j(\kappa_1)+1/2}\sqrt{(2j(\kappa_1)+1)+(2j(\kappa_2)+1)} \\
& \times \begin{pmatrix} j(\kappa_1) & j(\kappa_2) & 1 \\ -1/2 & 1/2 & 0 \end{pmatrix}\pi(l(-\kappa_1)+l(\kappa_2)+1) \\
& \times \int_0^\infty \mathrm{d}r F_{\mathrm{BW}}(r)\left(f_{n_1\kappa_1}(r_\mu)g_{n_2\kappa_2}(r_\mu)+f_{n_2\kappa_2}(r_\mu)g_{n_1\kappa_1}(r_\mu)\right).
\end{aligned}
$$

2.1.4.3 Rediagonalization of muonic fine-structure doublets

The concept of rediagonalization in the context of quasi-degenerate perturbation theory was introduced in Section 2.1.4.1. The unperturbed Hamiltonian is introduced in Eqs. (2.4) and (2.5) for the unperturbed states from Eq. (2.6). The matrix elements necessary for the rediagonalization of the hyperfine states are discussed in Section 2.1.4.2 for the general case. Thereby, all necessary ingredients for the rediagonalization in the dynamical hyperfine structure of muonic atoms are available. In this section, this concept is applied to a simplified part of the muonic ^{185}Re spectrum for clarification. The ^{185}Re nucleus has a ground state angular momentum of $I = 5/2$ [189], and in this section, the first two excited nuclear states with angular momentum quantum numbers of $7/2$ and $9/2$ are considered. As for the muonic states, the $(2p_{1/2},2p_{3/2})$ fine-structure doublet is considered. As a first step, it has to be considered, which unperturbed states $|FM_F IK n\kappa\rangle$ can be formed by the nuclear and the muonic states. In general, for every possible value of F, the projection quantum number has $(2F+1)$ possible values: $M_F = -F, ..., F$. The minimal value for F is $F_{\min} = \min(|j(\kappa)-I|)_{\kappa,I}$ and the maximal value for F is $F_{\max} = \max(j(\kappa)+I)_{\kappa,I}$ for the considered values of κ and I. In this example, the values are $F_{\max} = 6$ and $F_{\min} = 1$. As a next step, it has to be checked for every value of F, which combinations of muonic and nuclear states of the modelspace are able to have the F value. For this, the triangle equation $|j(\kappa)-I| \leq F \leq j(\kappa)+I$ has to hold. In this way, a modelspace is separated into distinct blocks, each with a value of F and a corresponding subset of states from the modelspace, which can form this F value. Since the hyperfine interactions are diagonal in F and M_F, the rediagonalization has to be performed only in the blocks separately and not in the entire modelspace. The separation of the modelspace into the different blocks is shown in Fig. 2.2. For the experimental nuclear excitation energies from [179] and the RMS radius from [178], the resulting level scheme without and with rediagonalized quadrupole interaction is shown in Fig. 2.3, which demonstrates the rich level structure in this case. Furthermore, there is no clear distinction between the fine- and hyperfine structure, since the nuclear rotational states, the fine-structure splitting and the quadrupole matrix elements are all on the same energy scale. In practice, for the calculations in Section 2.3 up to five excited nuclear states are used, which leads to even more energy levels.

After the rediagonalization, the previously unperturbed states $|FM_F IK n\kappa\rangle$ are mixed. The quantum numbers F and M_F describing the total angular momentum of the muon-nucleus system are still well-defined, since the hyperfine structure is diagonal therein.
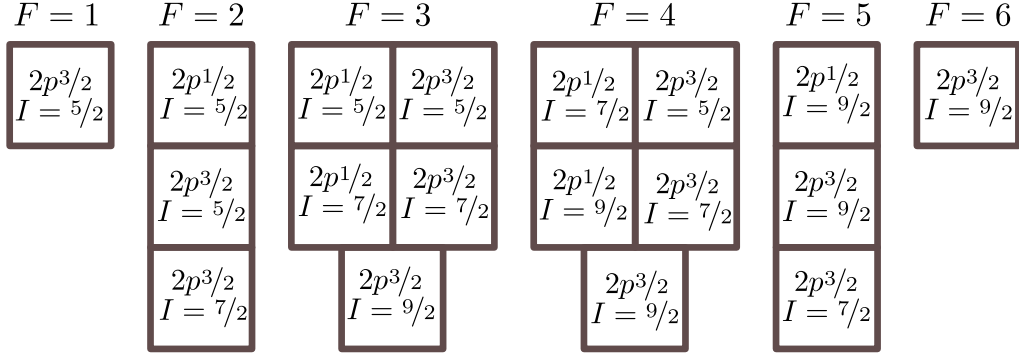
Figure 2.2: Separation of the modelspace consisting of the muonic $2p_{1/2}$ and $2p_{3/2}$ states coupled to the nuclear states with angular momentum 5/2, 7/2, and 9/2. For every possible value of $F = 1, ..., 6$, the states are shown, which are involved in the rediagonalization of the hyperfine interaction.

However, different I, κ, and in principle also n are mixed by the rediagonalization. The mixed state can be written as

$$|FM_F, i\rangle = \sum_{k=1}^{d} \alpha_k^{(i)} |FM_F I_k K n_k \kappa_k\rangle, \qquad (2.36)$$

where $i = 1, ..., d$ and d is the number of states in the modelspace, which can form the total angular momentum F. For the example of rhenium in this section, there is one state for $F = 1, 6$; three states for $F = 2, 5$; and five states for $F = 3, 4$ (see Fig. 2.2). Thus, e.g. for $F = 3$, a 5x5-matrix has to be rediagonalized, and the coefficient-matrix $\alpha_k^{(i)}$ in Eq. (2.36) corresponds to the matrix of corresponding eigenvectors.

2.1.5 Transition probabilities and intensities

It has been shown in Section 2.1.4 that the coupling of muonic states and nuclear rotational states in connection with a strong quadrupole interaction leads to a rich and complicated level structure without a clear distinction of fine- and hyperfine structure. As a result, there is a large number of potential transitions between the states. For example, if the L_α x-rays are considered, i.e. the transitions from the $3d$ fine-structure doublet to the $2p$ fine-structure doublet, there are only four transitions if the hyperfine structure is not considered. One of these transitions is suppressed because it is not an electric dipole transition. On the other hand, due to the dynamical hyperfine structure, there could be in principle hundreds of L_α x-rays and many of them would be of electric dipole type. As a consequence, for the comparison with experimental spectra not only the level structure is needed, but also the corresponding relative intensities. In experimental spectra, the intensity of a transition is proportional to the number of measured photons with the energy of the transition. The intensities are a product of two quantities: Firstly, it is proportional to the transition probability, which can be calculated, in principle, as soon as the wave functions and corresponding energies are known. In this thesis, the transition probabilities are calculated relativistically and without the long-wavelength
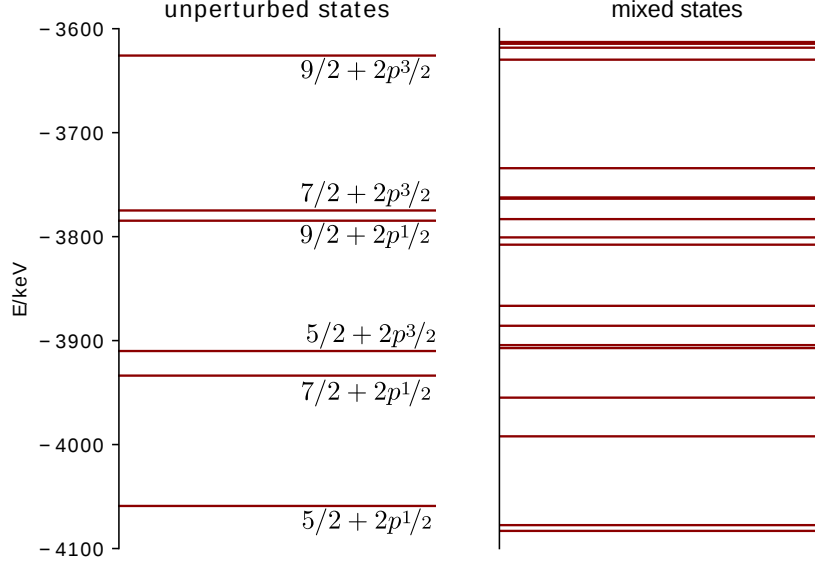
Figure 2.3: Level scheme of the muonic $2p_{1/2}$ and $2p_{3/2}$ states coupled to the nuclear $5/2$, $7/2$, and $9/2$ states in ^{185}Re. Zero energy corresponds to the free, resting muon and the nuclear ground state. Due to the nuclear rotational states and the strong quadrupole interaction, there is no clear distinction between fine- and hyperfine structure, which results in a rich structure of the energy levels.

approximation. Secondly, the intensities are proportional to the population of the initial state. However, for the calculation of the population of the initial states, all transitions to the initial state from even higher states have to be considered. This eventually leads to a cascade calculation for the muon, where the muon is initially in a highly excited state and drops towards the ground state step-by-step by radiative transitions. In the following, the transition probabilities, the population, and the cascade calculations are discussed separately.

As a first step, the transition probabilities due to spontaneous emission of a photon in a muonic transition will be analyzed in this paragraph. Starting point is the general formula for the Einstein coefficient (transition probability per time) for a state with defined total angular momentum from an initial state $|F_i M_i, i_i\rangle$ to a final state $|F_f M_f, i_f\rangle$, where the states, in which the hyperfine structure is diagonalized, are defined in Eq. (2.36). Following [182, Section 6.], this expression reads as

$$A_J^{(\lambda)} = \frac{2\alpha(2J+1)(J+1)}{J} \Delta E_{if} \sum_{M,M_i,M_f} \left| \left\langle F_f M_f, i_f \left| t_{JM}^{(\lambda)} \right| F_i M_f, i_i \right\rangle \right|^2 . \qquad (2.37)$$

Here, ΔE_{if} is the energy difference of the initial and final state, J is the total angular momentum of the photon and $\lambda = 1$ corresponds to an electric transition, whereas $\lambda = 0$ stands for a magnetic transition. The multipole transition operator $t_{JM}^{(\lambda)}$ is defined in Eqs. (6.120), (6.121), (6.128), and (6.129) of Ref. [182] in terms of the components of the

multipole potential $\mathbf{a}_{JM}^{(\lambda)}$ and of the scalar potential φ_{JM} as

$$\boldsymbol{\alpha} \cdot \mathbf{a}_{JM}^{(\lambda)}(\mathbf{r}_\mu) - \varphi_{JM}(\mathbf{r}_\mu) = i\sqrt{\frac{(2J+1)(J+1)}{4\pi J}} t_{JM}^{(\lambda)}(\mathbf{r}_\mu).$$

Using Eq. (2.36) for the definition of the mixed states is terms of the unperturbed states $|FM_F\,IK\,n\kappa\rangle$, the matrix elements are written as

$$\left\langle F_f M_f, i_f \left| t_{JM}^{(\lambda)} \right| F_i M_f, i_i \right\rangle = \sum_{k_i, k_f} \alpha_{k_f}^{(i_f)*} \alpha_{k_i}^{(i_i)} \left\langle F_f M_f\, I_{k_f} K\, n_{k_f} \kappa_{k_f} \left| t_{JM}^{(\lambda)} \right| F_i M_i\, I_{k_i} K\, n_{k_i} \kappa_{k_i} \right\rangle.$$

Since the muonic transitions are considered in this section, the transition operator acts on the muonic coordinates $\mathbf{r}_\mu$ only. These despribe one subsystem of the composite states in Eq. (2.37) with total angular momentum F_i and F_f, respectively. Since the multipole transition operator is an irreducible tensor operator of rank J, Eq. (A.14) can be used for the computation of the matrix elements. This results in the following expression for the matrix elements:

$$\left\langle F_f M_f\, I_{k_f} K\, n_{k_f} \kappa_{k_f} \left| t_{JM}^{(\lambda)} \right| F_i M_i\, I_{k_i} K\, n_{k_i} \kappa_{k_i} \right\rangle = \delta_{I_{k_f} I_{k_i}} (-1)^{F_i + j(\kappa_{k_f}) + I_{k_i} - J}$$

$$\times \sqrt{2F_i + 1}\, \mathrm{C}_{F_i M_i\, JM}^{F_f M_f} \begin{Bmatrix} j(\kappa_{k_i}) & j(\kappa_{k_f}) & J \\ F_f & F_i & I_{k_i} \end{Bmatrix} \left\langle n_{k_f} \kappa_{k_f} \left\| t_J^{(\lambda)} \right\| n_{k_i} \kappa_{k_i} \right\rangle. \quad (2.38)$$

The only dependency on the projection numbers M, M_f, and M_i is in the arguments of the Clebsch-Gordan coefficients. Furthermore, the Clebsch-Gordan coefficients in Eq. (2.38) do not depend on the summation indices k_i and k_f. Therefore, the summation over M, M_f, M_i only affects the Clebsch-Gordan coefficients and the sum rule [168]

$$\sum_{M, M_i, M_f} \left(C_{F_i M_i\, JM}^{F_f M_f} \right)^2 = 2F_f + 1$$

can be used to simplify the calculation of Eq. (2.37) considerably. According to Ref. [182], the reduced matrix elements in the muonic variables in Eq. (2.38) can be evaluated in length gauge as

$$\left\langle n_f \kappa_f \left\| t_J^{(1)} \right\| n_i \kappa_i \right\rangle = \langle n_f \kappa_f \| C_J \| n_i \kappa_i \rangle \tag{2.39}$$

$$\times \int \mathrm{d}r\, r^2 \Bigg\{ j_J(\Delta E_{if}\, r) \left[g_{n_f \kappa_f}(r) g_{n_i \kappa_i}(r) + f_{n_i \kappa_i}(r) f_{n_f \kappa_f}(r) \right]$$

$$+ j_J(\Delta E_{if}\, r) \left[\frac{\kappa_i - \kappa_f}{J+1} \left(g_{n_f \kappa_f}(r) f_{n_i \kappa_i}(r) + g_{n_i \kappa_i}(r) f_{n_f \kappa_f}(r) \right) \right.$$

$$\left. + \left(g_{n_i \kappa_i}(r) f_{n_f \kappa_f}(r) - g_{n_f \kappa_f}(r) f_{n_i \kappa_i}(r) \right) \right] \Bigg\}$$

for electric transitions with $\lambda = 1$ and as

$$\left\langle n_f\kappa_f\middle|\middle|t_J^{(0)}\middle|\middle|n_i\kappa_i\right\rangle = \langle n_f\left(-\kappa_f\right)||C_J||n_i\kappa_i\rangle$$
$$\times \int dr\, r^2 \frac{\kappa_i + \kappa_f}{J+1} j_J(\Delta E_{if}\, r) \left[-g_{n_f\kappa_f}(r)f_{n_i\kappa_i}(r) - f_{n_f\kappa_f}(r)g_{n_i\kappa_i}(r)\right] \tag{2.40}$$

for magnetic transitions with $\lambda = 0$. Here, $j_J(x)$ are the spherical Bessel functions [193, Eq. 10.47.3]. The reduced matrix elements of the normalized spherical harmonics $C_{JM}(\vartheta, \varphi)$ read as [182]

$$\langle n_f\kappa_f||C_J||n_i\kappa_i\rangle =(-1)^{j(\kappa_f)+1/2}\sqrt{(2j(\kappa_i)+1)(2j(\kappa_f)+1)}$$
$$\times \pi(l(\kappa_f)+l(\kappa_i)+J) \begin{pmatrix} j(\kappa_f) & j(\kappa_i) & J \\ -\frac{1}{2} & \frac{1}{2} & 0 \end{pmatrix}, \tag{2.41}$$

where the function $\pi(x)$ is defined in Eq. (2.33). The angular momentum selection rules are implemented in the 6j- and 3j-symbols and in the function $\pi(x)$ in Eqs. (2.38) and (2.41). For electric dipole transitions with $J = 1$ and $\lambda = 1$, the following selection rules have to be fulfilled:

$$\begin{aligned} j(\kappa_i) &= j(\kappa_f) && \text{or} & j(\kappa_i) &= j(\kappa_f) \pm 1, \\ F_i &= F_f && \text{or} & F_i &= F_j \pm 1, \\ l(\kappa_i) &= l(\kappa_f) \pm 1. && && \end{aligned} \tag{2.42}$$

The relativistic expression for the electric transitions in Eq. (2.39) can be simplified in the long-wavelength approximation. This neglects the effects of retardation. In this case, the lower component of the radial spinors $f_{n\kappa}(r)$ is small, and therefore mixed terms $f_{n_1\kappa_1}(r)g_{n_2\kappa_2}(r)$ can be neglected. The term $\sim f_{n\kappa}(r)^2$ is kept for convenience, since $r^2 g_{n\kappa}(r)^2 + r^2 f_{n\kappa}(r)^2$ corresponds to the radial probability density. The long-wavelength approximation means, that $\Delta E_{if}\, r$ is small, and therefore the corresponding spherical Bessel function can be expanded. For small arguments, the spherical Bessel functions can be approximated as

$$j_J(x) \approx \frac{x^J}{(2J+1)!!},$$

where the double factorial is evaluated as $n!! = n \cdot (n-2) \cdot (n-4) \cdot \dots$. Thereby, Eq. (2.39) becomes

$$\left\langle n_f\kappa_f\middle|\middle|t_J^{(1)}\middle|\middle|n_i\kappa_i\right\rangle = \langle n_f\kappa_f||C_J||n_i\kappa_i\rangle$$
$$\times \frac{\Delta E_{if}^J}{(2J+1)!!} \int dr\, r^2\, r^J \left(g_{n_f\kappa_f}(r)g_{n_i\kappa_i}(r) + f_{n_i\kappa_i}(r)f_{n_f\kappa_f}(r)\right),$$

and the corresponding transition probabilities per time from Eq. (2.37) thereby have the energy dependence dependence $\sim \Delta E_{if}^{2J+1}$.

After the transition probabilities have been discussed in the last paragraph, the remaining issue of the population of the initial states is discussed in the following. The transition probabilities can be calculated ab initio, independent from experimental details. Unfortunately, this is not the case for the population. Here, details of the experimental setup and the capture process have to be considered. Muonic atoms are typically created by shooting a slow muon beem on a target, which contains the isotope of interest [83–85]. The average population of the muonic states after the muon has been captured by the nucleus depends on the state of the incoming muon as well as details of the nuclear target. Additionally, for highly excited states, the muon and the atomic electrons are not well separated, as described in Section 2.1.3.4, thus the muon-electron interaction has to be taken into account and for example Auger transitions can occur [194]. In heavy nuclei, this leads to a complicated many-body problem. Even if an initial population of the low-lying muonic states where the electron-muon interaction can be neglected would be known in form of the diagonal elements of the muonic density matrix, the master equation using transition probabilities as given in Eqs.(2.39) and (2.40) has to be solved [194]. Due to the large number of energy levels in the dynamical hyperfine structure and the calculation of the transition probabilities with Eq. (2.37), this is still a very time-consuming calculation.

However, the cascade calculation can be simplified considerably. In experiments, muons typically tend to be captured in circular orbits, which are states with maximal angular momentum $l = n - 1$. Additionally, the fastest transitions are electric dipole transitions of the muon, which change the orbital angular momentum quantum number of the muon by one. The most probable sequence of transitions correspondingly is: $5g \rightarrow 4f \rightarrow 3d \rightarrow 2p \rightarrow 1s$. Especially the $2p \rightarrow 1s$ (K_α x-rays) and $3d \rightarrow 2p$ (L_α x-rays) spectra have been used in the past to obtain information about nuclear structure from experiments with muonic atoms, e.g. in Refs. [73, 77–80, 195, 196]. Under the assumption that the muon starts in a circular orbit and then cascades by electric dipole transitions, the calculation of the intensities is considerably simplified. Because of the selection rules from Eq. (2.42), the $2p$ state can be only populated by the $3d$ states, which can only be populated by the $4f$ states and so on. This approach for the cascade calculations will be used also in this thesis. The population of a state in the, say, $2p$ states can be obtained by summing up all intensities of the transitions from the $3d$ states to this state. Finally, only the initial population of the initial states with the highest n needs to be given. Here, a simple statistical population has proved to describe experiments correctly [195], where every coupled muon-nucleus state with total angular momentum F has a relative population $\sim (2F + 1)$, corresponding to the different M_F values. Furthermore, initially the nucleus is in its ground state, since the excitation of nuclear rotational levels only occurs during the muonic cascade, when energy is transfered from the muon to the nucleus. The cascade starting from the muonic $4f$ states is visualized in Fig. 2.4. In practice, the calculation of the spectrum begins with the diagonalization the hyperfine interaction in the fine-structure doublets of the states with circular orbits ($2p$, $3d$, $4f$). Then, under the assumption of a relative population proportional to $(2F + 1)$ in the fine-structure doublet with the highest quantum number $n = n_{\max}$, all transitions to the next states with $n_{\max-1}$ are calculated. The relative population of the $n_{\max-1}$ states is obtained by summing up the intensities of all transitions to this state. This procedure can be repeated

$$\mu \quad Z$$

$$\frac{4f\frac{7}{2}}{4f\frac{5}{2}} \otimes \underline{I_{nucl} = I_0} \qquad M$$

$$\frac{3d\frac{5}{2}}{3d\frac{3}{2}} \otimes \frac{\overline{\cdots}}{\underline{I_{nucl} = I_0 + 1}} \qquad L$$

$$\frac{2p\frac{3}{2}}{2p\frac{1}{2}} \otimes \frac{\overline{\cdots}}{\underline{I_{nucl} = I_0 + 1}} \qquad K$$

$$1s\frac{1}{2} \otimes \frac{\overline{\cdots}}{\underline{I_{nucl} = I_0 + 1}}$$
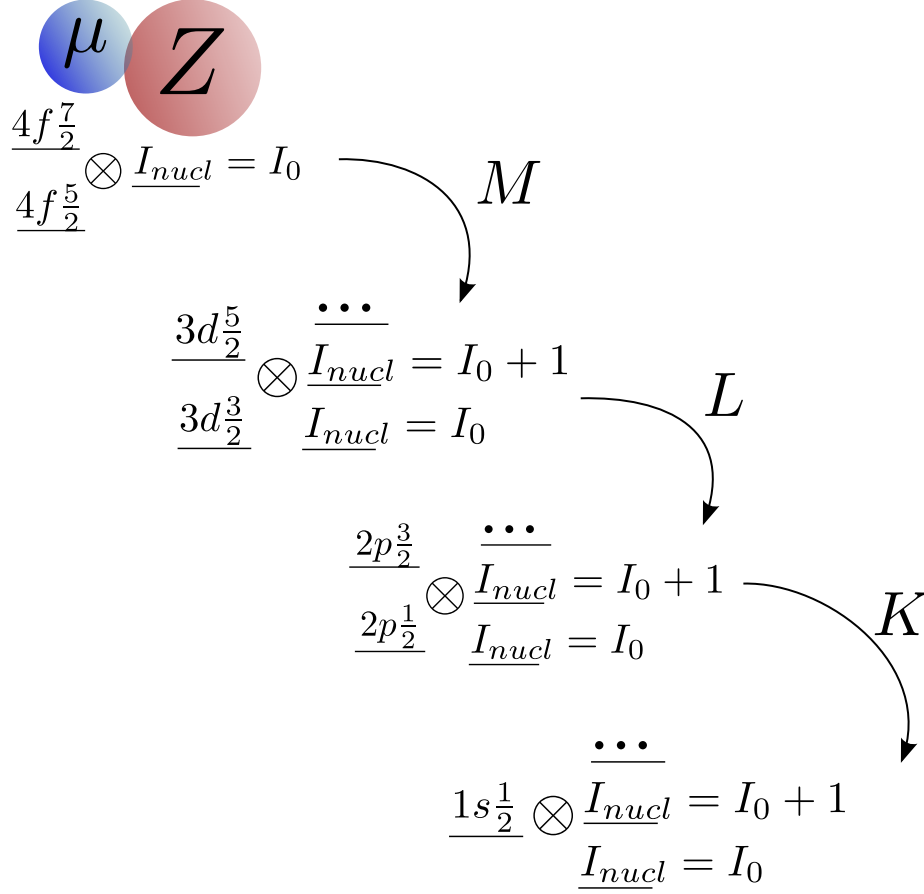
Figure 2.4: Visualization of the muonic cascade, starting from the muonic $4f$ states and the nucleus in its ground state. Then, the muon is cascading towards its ground state through the $3d$ and $2p$ states. Here, excited nuclear rotational states can be populated. The population of a state in the $3d$ modelspace is obtained by summing up all transitions from the $4f$ states to this state, and analogously for the $2p$ states. For a given initial population of the $4f$ states, in this way all intensities can be calculated.

until the muonic ground state is reached, and thereby all line-intensities are obtained. A statistical population $\sim (2F + 1)$ in the higher states leads to a statistical population in the lower states, as long as the hyperfine-structure splitting can be neglected. In states with $n > 3$, the hyperfine-structure splitting is typically small. Therefore, statistically populated $6h$ states lead to (almost) statistically populated $5g$, which in turn result in (almost) statistically populated $4f$ states. Thereby, the line intensities are in practice insensitive on the starting point of the cascade. The calculation of transition probabilities is used in Section 2.3 for the analysis of the spectrum of muonic rhenium.

2.2 Higher order corrections for the dynamical hyperfine structure

In this section, improved calculations of two higher order contributions to the dynamical hyperfine structure are discussed. Firstly, corrections of the quadrupole matrix elements due to vacuum polarization (VP) are considered. Furthermore, a numerical treatment of second order quadrupole interactions is presented. This work was also submitted for publication in Ref. [3].

The contribution of leading order VP to the spherically symmetric part of the charge distribution was briefly discussed in Section 2.1.3.2. However, VP influences multipole interactions of all orders, thus in the context of the dynamical hyperfine structure it influences matrix elements of the quadrupole interaction between muon and nucleus. Until now, the corresponding correction to the matrix elements has only been considered with a power-series expansion [74, 197] or for specific forms of the nuclear charge distribution [198], which does not enable precision calculations for heavy muonic atoms. In this thesis, a new approach is developed in Section 2.2.1 by performing a multipole expansion of the Uehling potential. This enables the calculation of the leading order VP correction to the quadrupole matrix elements for arbitrary charge distributions with all finite size effects.

The approach of quasi-degenerate perturbation theory is discussed in Section 2.1.4.1, and the rediagonalization of the perturbation is applied to the hyperfine interaction in Section 2.1.4.2 and 2.1.4.3. However, there are residual second order corrections due to contributions from outside of the modelspace, as introduced in Eq. (2.28). A non-relativistic estimation of the residual second order electric quadrupole interaction with states outside of this modelspace has been presented in Ref. [199]. In this thesis, an extended, fully relativistic approach is presented in Section 2.2.2.

2.2.1 Quadrupole-Uehling interactions

The resummation of the order $\alpha(Z\alpha)$ VP (Uehling potential) has been discussed in Section 1.1.1, with the result that it can be included in the Dirac equation. The starting point of this section is the renormalized expression for the Uehling potential for a given deformed nuclear charge distribution, which reads in the chosen system of units (Appendix A.1) as [161]

$$V_{\text{uehl}}(\mathbf{r}'_\mu) = -Z\alpha \frac{2\alpha}{3\pi} \int \mathrm{d}^3\mathbf{r}'_N \frac{\rho(\mathbf{r}'_N)}{|\mathbf{r}'_\mu - \mathbf{r}'_N|} K_1(2m_e|\mathbf{r}'_\mu - \mathbf{r}'_N|), \qquad (2.43)$$

where m_e is the electron mass, and primed coordinates belong to the body-fixed nuclear system, as defined in 2.1.2. $K_1(x)$ belongs to the family of functions

$$K_n(x) = \int_1^\infty \mathrm{d}t\, \mathrm{e}^{-xt} \left(\frac{1}{t^3} + \frac{1}{2t^5} \right) \sqrt{t^2 - 1}\, t^n.$$

For different n, the functions $K_n(x)$ are related by

$$
\begin{aligned}
K_n(x) &= -\partial_x K_{n-1}(y), \\
K_{n-1}(x) &= -\int^x \mathrm{d}y\, K_n(y).
\end{aligned}
\tag{2.44}
$$

Furthermore, they can be expressed in terms of Meijer G-functions from Eq. (A.2) as

$$
K_n(x) = \frac{1}{4} G_{1,3}^{3,0}\left(\frac{x^2}{4}\middle|\begin{matrix}-\frac{n}{2}+2\\-\frac{n}{2}+\frac{1}{2},0,\frac{1}{2}\end{matrix}\right) + \frac{1}{8} G_{1,3}^{3,0}\left(\frac{x^2}{4}\middle|\begin{matrix}-\frac{n}{2}+3\\-\frac{n}{2}+\frac{3}{2},0,\frac{1}{2}\end{matrix}\right),
\tag{2.45}
$$

which makes it possible to evaluate them with arbitrary precision implementations of the Meijer G-function in existing libraries or programs like Refs. [200, 201]. The Uehling potential (2.43) depends only on $|\mathbf{r}'_\mu - \mathbf{r}'_N|$, similar to the electric potential (2.3), which can be written as

$$
|\mathbf{r}'_\mu - \mathbf{r}'_N| = |\mathbf{r}_\mu - \mathbf{r}_N| = \sqrt{r_\mu^2 + r_N^2 - 2r_\mu r_N y},
$$

and therefore only depends on the lengths of the vectors and on $y=\cos(\sphericalangle\mathbf{r}_\mu\mathbf{r}_N)$. The dependence on $|\mathbf{r}'_\mu - \mathbf{r}'_N|$ is more complicated for the Uehling potential, but a multipole expansion can be performed nonetheless by expanding the dependence on y in Legendre polynomials. It reads

$$
\begin{aligned}
\frac{K_1(2m_e|\mathbf{r}'_\mu - \mathbf{r}'|)}{|\mathbf{r}'_\mu - \mathbf{r}'|} &= \sum_{l=0}^{\infty} c_l(r_\mu, r_N) P_l(y) \\
&= \sum_{l=0}^{\infty} c_l(r_\mu, r_N) \sum_{m=-l}^{l} \mathrm{C}^*_{lm}(\vartheta'_N, \varphi'_N) \mathrm{C}_{lm}(\vartheta'_\mu, \varphi'_\mu),
\end{aligned}
$$

where the second equality is a consequence of the addition theorem (A.8) of Legendre polynomials. The expansion coefficients are still functions of the lengths of the vectors and are defined as

$$
c_l(r_\mu, r_N) = \frac{2l+1}{2} \int_{-1}^{1} \mathrm{d}y \frac{K_1(2m_e|\mathbf{r}_\mu - \mathbf{r}_N|)}{|\mathbf{r}_\mu - \mathbf{r}_N|} P_l(y).
\tag{2.46}
$$

Eq. (2.46) can be either solved by numerical integration, or expressed in a closed form, using Eq. (2.45) for the functions $K_n(x)$. For the closed form expression, the integration variable y in Eq. (2.46) is substituted by $z = f^{-1}(y) = 2m_e|\mathbf{r}_\mu - \mathbf{r}_N|$ or $y = f(z) = (r_\mu^2 + r_N^2 - (z/2m)^2)/(2r_\mu r_N)$. Thereby, Eq. (2.46) reads as

$$
c_l(r_\mu, r_N) = \frac{2l+1}{4r_\mu r_N m_e} \int\limits_{2m_e|r_\mu - r_N|}^{2m_e(r_\mu + r_N)} \mathrm{d}z\, K_1(z) P_l(f(z)).
\tag{2.47}
$$

Since $f(z)$ is quadratic in z, it follows that $P_l(f(z))$ is a polynomial of degree $2l$. Thereby, Eq.(2.47) can be integrated by part $2l$-times for the two functions $K_1(z)$ and $P_l(f(z))$,

using the relations from Eq. (2.44), to solve the integral as

$$c_l(r_\mu, r_N) = \frac{2l+1}{4r_\mu r_N m_e} \sum_{i=0}^{2l} K_{-i}(z)\, \partial_y^{(i)} P_l(f(z)) \bigg|_{y=2m_e(r_\mu+r_N)}^{y=2m_e|r_\mu-r_N|}.$$

Thereby, the Uehling potential can be written, analogously to the electric potential, as

$$V_{\text{uehl}}(\mathbf{r}_\mu, \phi, \theta) = \sum_{l=0}^{\infty} -Z\alpha \frac{2\alpha}{3\pi} \int \mathrm{d}^3 r_N'\, c_l(r_\mu, r_N) P_l(\cos\vartheta_N') \rho(\mathbf{r}_N') \sum_{m=-l}^{l} \mathrm{C}_{lm}^*(\theta, \phi) \mathrm{C}_{lm}(\vartheta_\mu, \varphi_\mu).$$

$$=: \sum_{l=0}^{\infty} Q_{\text{uehl}}^{(l)}(r_\mu) \sum_{m=-l}^{l} C_{lm}^*(\theta, \phi) C_{lm}(\vartheta_\mu, \varphi_\mu)$$

$$=: \sum_{l=0}^{\infty} V_{\text{uehl}}^{(l)}(\mathbf{r}_\mu, \phi, \theta). \tag{2.48}$$

For $l = 0$, the expression for Uehling potential of a spherical charge distribution [161] which only depends on r_μ is recovered as

$$V_{\text{uehl}}^{(0)}(r_\mu) = -\frac{2\alpha(Z\alpha)}{3m_e r} \int_0^\infty \mathrm{d}r'\, \rho_0(r') \left[K_0(2m_e|r-r'|) - K_0(2m_e(r+r')) \right], \tag{2.49}$$

where the spherically averaged part of the charge distribution is

$$\rho_0(r) = \frac{1}{4\pi} \int_0^{2\pi} \mathrm{d}\varphi \int_0^\pi \mathrm{d}\vartheta \sin(\vartheta) \rho(\mathbf{r}).$$

The approach is applicable for arbitrary charge distributions, and is applied for the quadrupole term with $l = 2$ in Section 2.3. In the following, the quadrupole term $l = 2$ is considered for the models of a charged-shell and point-like quadrupole distribution, where the corresponding term in Eq. (2.48) can be simplified. For the charged-shell quadrupole distribution, the nuclear charge distribution is written as

$$\rho(\mathbf{r}_N) \quad = \rho_0(r_N) + \rho_2(r_N, \vartheta_N)$$

$$\rho_2(r_N, \vartheta_N) = -\alpha Q_0 \frac{5}{8\pi} \frac{\delta(r-R)}{R^4} P_2(\cos\vartheta_N),$$

where the intrinsic quadrupole moment Q_0 is concentrated at the nuclear radius R. Thereby, the quadrupole part of the Uehling potential (2.48) reads

$$V_{\text{uehl}}^{(2)}(\mathbf{r}_\mu, \phi, \theta) = -\alpha Q_0 \frac{\alpha}{3\pi} \frac{c_2(r_\mu, R)}{R^2} \sum_{m=-l}^{l} C_{lm}^*(\theta, \phi) C_{lm}(\vartheta_\mu, \varphi_\mu). \tag{2.50}$$

A point-like quadrupole moment corresponds to the limit of zero nuclear radius R in Eq. (2.50). The limit cannot be calculated naively due to the R^2 factor in the denominator. However, it turns out that the Taylor expansion of $c_2(r_\mu, R)$ around $R = 0$ has
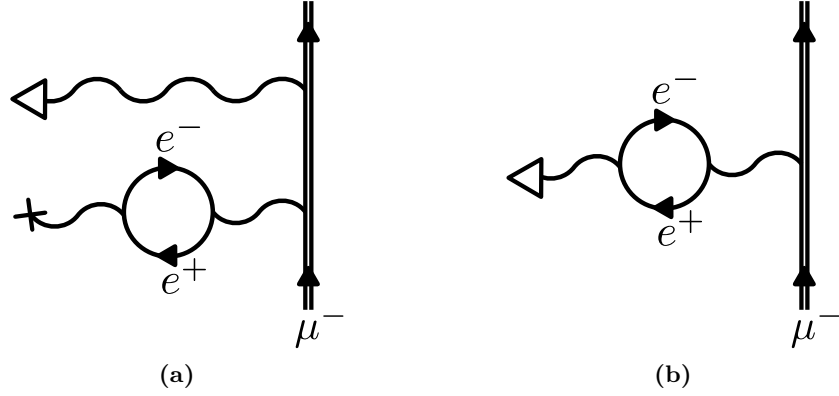
Figure 2.5: Feynman diagrams for the leading order contributions of the vacuum polarization to the quadrupole interaction in muonic atoms. An external double line stands for the bound-muon wave function. A single internal line for the free electron propagator, and a wave line for the photon propagator. A cross represents the interaction with the monopole potential, and a triangle the interaction with the quadrupole potential. Contribution (a) is calculated by including the spherically symmetric contribution of the Uehling potential (2.49) in the Dirac equation; contribution (b) by including the quadrupole contribution of the Uehling potential (2.48) in the matrix elements.

no constant and no linear term. Therefore, $c_2(r_\mu, R)$ can be expanded for small R as

$$c_2(r_\mu, R) = \frac{K_1(2m_e r_\mu) + 2m_e r_\mu K_2(2m_e r_\mu) + 4m_e^2 r_\mu^2/3 K_3(2m_e r_\mu)}{r^3} R^2 + \mathcal{O}(R^3),$$

and therby the point-like limit of quadrupole Uehling potential reads

$$V_{\text{uehl}}^{(2)}(\mathbf{r}_\mu, \phi, \theta) = -\alpha Q_0\, g(r) \sum_{m=-l}^{l} C_{lm}^*(\theta, \phi) C_{lm}(\vartheta_\mu, \varphi_\mu). \tag{2.51}$$

$$g(r) = \frac{\alpha}{3\pi} \frac{K_1(2m_e r_\mu) + 2m_e r_\mu K_2(2m_e r_\mu) + 4m_e^2 r_\mu^2/3 K_3(2m_e r_\mu)}{r^3}.$$

The expressions for the quadrupole Uehling potential for the charged-sphere and point-like distributions from Eqs. (2.50), (2.51), respectively, can be used for testing the implementation of the general case in Eq. (2.48).

2.2.2 Residual second order corrections

The rediagonalization of the hyperfine interaction in muonic atoms is explained in Section 2.1.4, using a modelspace consisting of a muonic fine-structure doublet and the first rotational nuclear states. Also, the leading contribution from states outside of the modelspace is derived in Eq. (2.28). Essentially, it is the second order energy correction due to the hyperfine interaction, excluding all states which are considered in the rediagonalization process. In the following, the residual second order corrections will be discussed

for the case of the rhenium $2p$ modelspace given in Section 2.1.4.3. Here, the modelspace consists of the muonic $2p_{1/2}$ and $2p_{3/2}$ states and the nuclear states $I = 5/2, 7/2, 9/2$. This results in 18 coupled states, with values of the total angular momentum $F = 1, ..., 6$, as shown in Fig. 2.2. The set of these states is called M_μ. The summation over all states, which are not in the modelspace involves all states $|FM_F\,I_iK_i\,n_i\kappa_i\rangle$ as defined in Eq. (2.6), where not all quantum numbers coincide with a state in the considered modelspace M_{2p}. In the following, this summation is schematically written as $\sum_{i\notin M_\mu}$.

After the subspace has been chosen and rediagonalization has been performed, the quadrupole interaction with states outside of the subspace leads to residual second order corrections to the energy levels [199]. For the total second order correction a summation/integration over the complete (discrete and continous) spectrum for both nuclear and muonic states has to be performed. For the complete nuclear spectrum, sophisticated models or numerous experimental data are required. However, the muon is point-like and can be described as a Dirac particle. Therefore, in this work, we calculate the second order corrections due to the electric quadrupole (Eq. (2.29)) and quadrupole-Uehling interaction (l=2-term in Eq. (2.48)), where the nucleus stays in the rotational ground state, but the complete muonic spectrum is considered. For a composite state from Eq. (2.36), where the hyperfine interaction is diagonalized in the modelspace, the second order energy shift due to states outside of the modelspace is

$$\Delta E_{2.\text{ord.}}^{(F,k)} = \sum_{i\notin M_\mu} \frac{\left|\langle FM_F k|\,V_{\text{el}}^{(2)} + V_{\text{uehl}}^{(2)}\,|FM_F n_i\kappa_i I_i K\rangle\right|^2}{E_{F,k} - E_i}, \tag{2.52}$$

where the sum is to be taken over all states not considered in the rediagonalization, including continuum states of the muon, and the unperturbed energy of the state i is $E_i = E_{n_i\kappa_i} + E_{I_i}$.

2.2.3 Evaluation for $^{185}_{75}$Re & $^{235}_{92}$U

Calculations of the quadrupole-Uehling potential and the residual second order corrections have been performed for muonic rhenium and uranium, assuming a deformed Fermi nuclear charge distribution which reads as

$$\rho_{ca\beta}(\mathbf{r}) = N\left[1 + \exp\left(\frac{r - c(1 + \beta\mathrm{Y}_{20}(\vartheta))}{a}\right)\right]^{-1},$$

where c is the half-density radius, a the skin thickness, β the deformation parameter, and N a normalization constant determined by the condition

$$\int \mathrm{d}^3\mathbf{r}\,\rho_{ca\beta}(\mathbf{r}) = 1.$$

Using the deformed Fermi distribution has proved to be suitable for the description of the level structure of heavy muonic atoms, e.g. [73, 78, 79]. Values for the parameters can be estimated by using a value a=2.3 fm/(4 ln 3), which has proved to be a sufficiently accurate value for most nuclei [126]. Then, c and β are chosen such that the quadrupole

moment and RMS value of the distribution are in agreement with the literature values from [178, 189]. For the nuclear states involved in the dynamical hyperfine structure, also the excitation energies are needed from literature [179]. The used parameters are summarized in Table 2.6. With these parameters, the electric and Uehling potentials, both monopole and quadrupole parts, can be calculated numerically. The muon wave functions are obtained by solving the Dirac equation (2.4) with the dual-kinetic-balance method [152]. Thereby, a complete set of muonic bound and continuum states is obtained. An overview for the binding energies of muon states important for the dynamical hyperfine splitting are shown in Table 2.7.

The quadrupole matrix elements can be calculated both for the rediagonalization in the dynamical hyperfine structure and for the evaluation of the residual second-order terms (2.52), using Eq. (2.31). As the next step, the total Hamiltonian (2.1) is diagonalized in finite subspaces or modelspaces consisting of the muonic ($2p_{1/2}$, $2p_{3/2}$) or ($3d_{3/2}$, $3d_{5/2}$) doublet states and nuclear ground state rotational band. For rhenium, the first six states with $I = 5/2, ..., 15/2$ are considered, and for uranium with $I = 7/2, ..., 17/2$. The excitation energies of the nuclear states are summarized, along with other nuclear parameters, in Table 2.6. Thereby, the composite states and corresponding energies E_{quad} from Eq. (2.36) are obtained and finally, for each of these states the residual second order quadrupole correction (2.52) is calculated. Here, the intermediate sum goes over the rotational nuclear and muonic states not included in the modelspace. For the muonic ground state, a rediagonalization is not necessary, since the diagonal matrix elements of the quadrupole interactions vanish for muonic states with $j = 1/2$. The quadrupole-Uehling contribution to the binding energies is the difference of two calculations; once all matrix elements contain both the electric and Uehling interaction $\left(V_{\text{el}}^{(2)} + V_{\text{uehl}}^{(2)}\right)$ and a second time only with the electric part $V_{\text{el}}^{(2)}$ from Eq.(2.31). Results for the residual second order quadrupole correction from Eq. (2.52) and for the quadrupole-Uehling corrections can be found in Table 2.8 for a number of states.

To conclude, the improved calculation of the higher order effects, the quadrupole interaction in the framework of the dynamical hyperfine structure in heavy muonic atoms was analyzed by a fully relativistic treatment of the quadrupole-Uehling potential and of the residual second order terms. The quadrupole-Uehling interaction was obtained rigorously by a multipole expansion of the Uehling potential for an arbitrary nuclear charge distribution. Since it has the same angular structure as the conventional quadrupole interaction, the quadrupole-Uehling expectation value also vanishes between two muonic states with $j = 1/2$, thus it does not affect the muonic ground state. The calculations for uranium show that it can lead to energy corrections almost on the keV level for very heavy nuclei with muonic $2p$ states and thus can be potentially visible in the current experiments. Being a short-ranged potential, it falls of quickly for states further away from the nucleus. For states with $n \geq 3$, we find values below $0.15\,\text{keV}$ even for highest Z. The generalization to Uehling corrections for higher-order multipoles is straight-forward. In the case of muonic atoms, since the influence of higher order multipoles is already small, this correction is expected to be negligible. The residual second order quadrupole corrections in the dynamical hyperfine structure were calculated numerically using a ba-

sis of relativistic wave functions including the nuclear finite-size correction and monopole Uehling correction. In contrast to the first order terms, the muonic ground state energy is affected by the second order corrections. Here, the energy correction amounts up to several keV. Also for muonic $2p$ states, it is of similar size. For the $3d$ levels, we find the energy corrections below $0.5\,$keV, both for rhenium and uranium. If a more advanced nuclear model than the rotational model is used, the additional nuclear states appear as intermediate states in the second order corrections, leading to the nuclear polarization corrections. Therefore, the approach presented in this work provides an excellent basis for an accurate treatment of the muonic spectrum of the nuclear polarization effect in deformed muonic atoms.

Table 2.2: Overview of the binding energies for muonic $^{205}_{83}$Bi, $^{147}_{62}$Sm, and $^{89}_{40}$Zr, obtained by solving the Dirac equation with the spherically symmetric parts of the muon-nucleus interaction. E_C are the binding energies (2.12) for a point-like nucleus. E_fs, E_uehl are the binding energies in the finite-size potential with and without the Uehling correction, respectively. The reduced mass is used to include the non-relativistic recoil corrections from Section 2.1.3.3. If not indicated, the uncertainties are negligible. All energies are in keV.

	state	E_C	E_fs	E_uehl
$^{205}_{83}$Bi	$1s_{1/2}$	21573.3	10699.(51.)	10767.(52.)
	$2s_{1/2}$	5538.6	3654.(15.)	3674.(15.)
	$2p_{1/2}$	5538.6	4893.(3.)	4927.(3.)
	$2p_{3/2}$	4958.9	4706.(5.)	4737.(5.)
	$3s_{1/2}$	2394.3	1796.(5.)	1804.(6.)
	$3p_{1/2}$	2394.3	2170.0(5)	2190.1(5)
	$3p_{3/2}$	2221.4	2131.(1.)	2141.(1.)
	$3d_{3/2}$	2221.4	2216.9(3)	2227.8(3)
	$3d_{5/2}$	2174.6	2172.8(2)	2183.0(2)
$^{147}_{62}$Sm	$1s_{1/2}$	11423.8	7165.(28.)	7213.(29.)
	$2s_{1/2}$	2895.7	2230.(7.)	2242.(7.)
	$2p_{1/2}$	2895.7	2778.(2.)	2795.(2.)
	$2p_{3/2}$	2736.9	2689.(2.)	2706.(2.)
	$3s_{1/2}$	1268.9	1061.(2.)	1066.(2.)
	$3p_{1/2}$	1268.9	1228.6(4)	1234.2(4)
	$3p_{3/2}$	1221.7	1204.7(6)	1210.0(6)
	$3d_{3/2}$	1221.7	1221.4(1)	1226.2(1)
	$3d_{5/2}$	1207.6	1207.4	1212.1
$^{89}_{40}$Zr	$1s_{1/2}$	4595.5	3643.(8.)	3669.(8.)
	$2s_{1/2}$	1155.2	1021.(2.)	1026.(2.)
	$2p_{1/2}$	1155.2	1147.8(2)	1153.7(2)
	$2p_{3/2}$	1129.9	1127.0(2)	1132.6(2)
	$3s_{1/2}$	510.6	469.8(5)	471.4(5)
	$3p_{1/2}$	510.6	508.0(1)	509.8(1)
	$3p_{3/2}$	503.1	502.0(1)	503.8(1)
	$3d_{3/2}$	503.1	503.1	504.5
	$3d_{5/2}$	500.7	500.7	502.1

Table 2.3: Relativistic recoil corrections to the binding energies for muonic $^{205}_{83}$Bi, $^{147}_{62}$Sm, and $^{89}_{40}$Zr. fm (full mass) denotes the finite size binding energy, analogous to the fourth column of Table 2.2, but with the rest mass of the muon used in the Dirac equation. $\Delta E_{\text{rec,nr}}$ is the non-relativistic recoil correction, which is the difference between the finite size Dirac solutions with reduced mass and full mass, respectively. $\Delta E_{n\kappa}^{(\text{rec,rel})}$ is the leading relativistic recoil correction from Section 2.1.3.3. If not indicated, the uncertainties are negligible. All energies are in keV.

	state	$E^{(\text{fm})}$	$\Delta E^{\text{rec,nr}}$	$\Delta E_{n\kappa}^{(\text{rec,rel})\text{a}}$
$^{205}_{83}$Bi	$1s_{1/2}$	10702.(51.)	-2.80(4)	0.39(4)
	$2s_{1/2}$	3656.(15.)	-1.42(2)	0.09(3)
	$2p_{1/2}$	4895.6(3.0)	-2.24(1)	0.12(3)
	$2p_{3/2}$	4708.2(4.6)	-2.27(1)	0.01(1)
	$3s_{1/2}$	1796.6(5.5)	-0.78(1)	0.03(3)
	$3p_{1/2}$	2180.0(0.5)	-1.05	0.03(3)
	$3p_{3/2}$	2131.9(1.3)	-1.06	0.03(3)
	$3d_{3/2}$	2218.1(0.3)	-1.21	0.02(2)
	$3d_{5/2}$	2174.0(0.2)	-1.19	0.02(2)
$^{147}_{62}$Sm	$1s_{1/2}$	7168.(28.)	-3.17(4)	0.29(7)
	$2s_{1/2}$	2231.1(6.7)	-1.31(1)	0.05(5)
	$2p_{1/2}$	2779.4(1.5)	-1.97(1)	0.05(5)
	$2p_{3/2}$	2691.2(1.8)	-1.96(1)	0.04(4)
	$3s_{1/2}$	1062.0(2.3)	-0.68(1)	0.02(2)
	$3p_{1/2}$	1229.5(0.4)	-0.89	0.01(1)
	$3p_{3/2}$	1205.6(0.6)	-0.89	0.01(1)
	$3d_{3/2}$	1222.3(0.1)	-0.93	0.01(1)
	$3d_{5/2}$	1208.3	-0.92	0.01(1)
$^{89}_{40}$Zr	$1s_{1/2}$	3646.5(8.2)	-3.36(3)	0.15(15)
	$2s_{1/2}$	1022.4(1.5)	-1.11(1)	0.02(2)
	$2p_{1/2}$	1149.2(0.2)	-1.43	0.01(1)
	$2p_{3/2}$	1128.4(0.2)	-1.41	0.01(1)
	$3s_{1/2}$	470.3(0.5)	-0.54	0.01(1)
	$3p_{1/2}$	508.6(0.1)	-0.64	0.00
	$3p_{3/2}$	502.7(0.1)	-0.63	0.00
	$3d_{3/2}$	503.7	-0.64	0.00
	$3d_{5/2}$	501.3	-0.63	0.00

^a$\Delta E^{\text{rec,nr}} := E^{(\text{red.mass})} - E^{(\text{fm})}$, see Section 2.1.3.3 for definitions.

Table 2.4: Electron screening corrections ΔE_{S} to the bound muon energy levels for muonic $^{205}_{83}\mathrm{Bi}$, $^{147}_{62}\mathrm{Sm}$, and $^{89}_{40}\mathrm{Zr}$. The subscript 'eff' are the screening corrections with the effective nuclear charge method, whereas '3step' use the 3 step calculation, both described in Section 2.1.3.4. For the superscript (1), only the 1s electrons are considered, while for (1+2), all electrons from with $n = 1, 2$ are considered. All energies are in keV.

	μ-state	$\Delta E_{\mathrm{S,eff}}^{(1)}$	$\Delta E_{\mathrm{S,eff}}^{(1+2)}$	$\Delta E_{\mathrm{S,3step}}^{(1)}$	$\Delta E_{\mathrm{S,3step}}^{(1+2)}$
$^{205}_{83}\mathrm{Bi}$	$1s_{1/2}$	5.555	10.825	5.555	10.825
	$2s_{1/2}$	5.537	10.803	5.538	10.805
	$2p_{1/2}$	5.548	10.817	5.549	10.818
	$2p_{3/2}$	5.547	10.816	5.548	10.817
	$3s_{1/2}$	5.490	10.748	5.494	10.753
	$3p_{1/2}$	5.514	10.776	5.516	10.779
	$3p_{3/2}$	5.512	10.774	5.515	10.777
	$3d_{3/2}$	5.526	10.791	5.528	10.793
	$3d_{5/2}$	5.525	10.789	5.527	10.792
$^{147}_{62}\mathrm{Sm}$	$1s_{1/2}$	3.705	7.312	3.705	7.312
	$2s_{1/2}$	3.699	7.305	3.700	7.305
	$2p_{1/2}$	3.703	7.309	3.703	7.309
	$2p_{3/2}$	3.703	7.309	3.703	7.309
	$3s_{1/2}$	3.682	7.285	3.683	7.286
	$3p_{1/2}$	3.689	7.293	3.691	7.295
	$3p_{3/2}$	3.689	7.293	3.690	7.294
	$3d_{3/2}$	3.694	7.299	3.695	7.300
	$3d_{5/2}$	3.694	7.298	3.694	7.299
$^{89}_{40}\mathrm{Zr}$	$1s_{1/2}$	2.214	4.405	2.214	4.405
	$2s_{1/2}$	2.212	4.402	2.212	4.403
	$2p_{1/2}$	2.213	4.403	2.213	4.403
	$2p_{3/2}$	2.213	4.403	2.213	4.403
	$3s_{1/2}$	2.205	4.395	2.206	4.396
	$3p_{1/2}$	2.207	4.397	2.208	4.398
	$3p_{3/2}$	2.207	4.397	2.208	4.398
	$3d_{3/2}$	2.209	4.399	2.210	4.400
	$3d_{5/2}$	2.209	4.399	2.209	4.400

Table 2.5: Results for the electric quadrupole and magnetic dipole hyperfine splitting for a selection of hyperfine states of muonic $^{205}_{83}$Bi ($I = \frac{9}{2}$), $^{147}_{62}$Sm ($I = \frac{7}{2}$), and $^{89}_{40}$Zr ($I = \frac{9}{2}$). ΔE_Q are the values of the electric quadrupole splitting. ΔE_M^{hom} is the magnetic dipole splitting from Eq. (2.23) using a homogeneous nuclear current distribution and ΔE_M^{sp} using the nuclear magnetization distribution in the single particle model. See Sections 2.1.3.5 and 2.1.3.6 for definitions. All energies are in keV.

nucleus	state	ΔE_Q		ΔE_M^{hom}		ΔE_M^{sp}	
		$F = I - \frac{1}{2}$	$F = I + \frac{1}{2}$	$F = I - \frac{1}{2}$	$F = I + \frac{1}{2}$	$F = I - \frac{1}{2}$	$F = I + \frac{1}{2}$
^{205}Bi	$1s_{1/2}$	0	0	-2.27(20)	1.86(16)	-2.41(20)	1.97(16)
	$2s_{1/2}$	0	0	-0.43(5)	0.35(4)	-0.47(6)	0.38(4)
	$2p_{1/2}$	0	0	-1.23(11)	1.01(9)	-1.31(11)	1.07(10)
	$2p_{3/2}$	7.0(1.0)	13.9(1.9)	-0.55(2)	0.010(4)	-0.554(22)	0.098(4)
	$3s_{1/2}$	0	0	-0.144(20)	0.118(16)	-0.160(20)	0.131(16)
	$3p_{1/2}$	0	0	-0.311(33)	0.255(26)	-0.336(33)	0.275(27)
	$3p_{3/2}$	1.9(3)	3.9(6)	-0.160(7)	0.028(1)	-0.163(7)	0.029(1)
	$3d_{3/2}$	1.01(5)	2.02(10)	-0.161(6)	0.028(1)	-0.163(6)	0.029(1)
	$3d_{5/2}$	0.74(3)	1.72(8)	-0.103(3)	-0.027	-0.103(3)	-0.027
^{147}Sm	$1s_{1/2}$	0	0	0.42(18)	-0.33(14)	0.25(17)	-0.20(14)
	$2s_{1/2}$	0	0	0.072(39)	-0.056(30)	0.033(39)	-0.026(30)
	$2p_{1/2}$	0	0	0.164(58)	-0.127(45)	0.106(58)	-0.082(45)
	$2p_{3/2}$	1.13(11)	2.94(29)	0.066(8)	-0.004(1)	0.058(8)	-0.004(1)
	$3s_{1/2}$	0	0	0.023(13)	-0.018(10)	0.010(13)	-0.008(8)
	$3p_{1/2}$	0	0	0.044(18)	-0.034(14)	0.026(18)	-0.02(1)
	$3p_{3/2}$	0.32(4)	0.84(10)	0.020(3)	-0.001	0.017(3)	-0.001
	$3d_{3/2}$	0.110(4)	0.287(9)	0.015(1)	0.000	0.014(1)	0.000
	$3d_{5/2}$	0.056(3)	0.234(13)	0.010	0.004	0.010	0.004
^{89}Zr	$1s_{1/2}$	0	0	0.36(13)	-0.29(10)	0.23(12)	-0.19(10)
	$2s_{1/2}$	0	0	0.053(23)	-0.043(18)	0.030(23)	-0.025(18)
	$2p_{1/2}$	0	0	0.071(14)	-0.058(11)	0.057(14)	-0.047(11)
	$2p_{3/2}$	-0.48(19)	-0.97(37)	0.023(1)	-0.004	0.022(1)	-0.004
	$3s_{1/2}$	0	0	0.016(7)	-0.013(6)	0.009(7)	-0.007(6)
	$3p_{1/2}$	0	0	0.020(4)	-0.017(4)	0.016(4)	-0.013(4)
	$3p_{3/2}$	-0.143(56)	-0.29(11)	0.007	-0.001	0.007	-0.001
	$3d_{3/2}$	-0.036(12)	-0.072(24)	0.004	0.000	0.004	0.000
	$3d_{5/2}$	-0.029(10)	-0.067(24)	0.003	0.000	0.003	0.000

Table 2.6: Nuclear parameters used in the numerical calculations. I_0 is the nuclear ground state angular momentum. RMS and Q_{spec} are the nuclear RMS radius and spectroscopic quadrupole moment of the nuclear ground state from [178, 189], respectively. c, a, β are the parameters of the deformed Fermi distribution derived from RMS and Q_{spec}. E_I are the excitation energies of the nuclear rotational states with angular momentum I (values are taken from Ref. [179]).

		$^{185}_{75}\mathrm{Re}$	$^{235}_{92}\mathrm{U}$
I_0		5/2	7/2
RMS	[fm]	5.3596(172)	5.8337(41)
Q_{spec}	[b]	2.21(4)	4.936(6)
c	[fm]	6.3517	6.9562
a	[fm]	0.5234	0.5234
β		0.2322	0.2711
E_{I_0+1}	[keV]	125.3587(9)	46.108(8)
E_{I_0+2}	[keV]	284.2(3)	103.903(8)
E_{I_0+3}	[keV]	475.7(4)	171.464(13)
E_{I_0+4}	[keV]	697.1(5)	250.014(21)
E_{I_0+5}	[keV]	949.7(5)	339.976(24)

Table 2.7: Binding energies of the low-lying, unperturbed muonic states due to the spherically symmetric parts of the electric and Uehling potential obtained by solving Eq. (2.4) for muonic rhenium and uranium. E_{c} shows the binding energies for a point-like Coulomb potential, E_{fs} and E_{uehl} include the finite size corrections without and with Uehling potential, respectively. All energies are in keV.

	state	E_{c}	E_{fs}	E_{uehl}
$^{185}_{75}\mathrm{Re}$	$1s_{1/2}$	17229.12	9333.46	9394.02
	$2s_{1/2}$	4398.85	3083.91	3100.44
	$2p_{1/2}$	4398.85	4032.61	4059.50
	$2p_{3/2}$	4033.07	3885.75	3910.50
	$3s_{1/2}$	1912.97	1498.01	1504.28
	$3p_{1/2}$	1912.97	1789.84	1798.66
	$3p_{3/2}$	1804.01	1751.38	1759.75
	$3d_{3/2}$	1804.01	1802.05	1810.30
	$3d_{5/2}$	1773.14	1772.36	1780.16
$^{235}_{92}\mathrm{U}$	$1s_{1/2}$	27351.29	12100.56	12175.51
	$2s_{1/2}$	7074.68	4308.67	4332.13
	$2p_{1/2}$	7074.68	5901.35	5941.39
	$2p_{3/2}$	6130.65	5674.78	5711.89
	$3s_{1/2}$	3033.18	2148.86	2158.31
	$3p_{1/2}$	3033.18	2645.58	2659.26
	$3p_{3/2}$	2751.54	2588.19	2601.27
	$3d_{3/2}$	2751.54	2739.69	2754.06
	$3d_{5/2}$	2679.66	2674.77	2688.10

Table 2.8: Overview of energy corrections due to residual second order electric quadrupole splitting $\Delta E_{2.\text{ord.}}$ and quadrupole-Uehling interaction $\Delta E_{\text{quad-uehl}}$ for $^{185}_{75}\text{Re}$ and $^{235}_{92}\text{U}$. F is the total angular momentum of muon and nucleus, I_N is the nuclear angular momentum and μ-state is the muonic state in spectroscopic notation. For the muonic $2p$ and $3d$ states, these are mixed by the dynamical hyperfine structure, thus I_N (main) and μ-state (main) denote states with the largest contribution. E_{quad} is the binding energy without quadrupole Uehling and residual second order quadrupole interaction. The states are ordered descending in the total energy E_{tot}. See Section 2.2 for details. All energies are in keV.

	F	I_N (main)	μ-state (main)	E_{quad}	$\Delta E_{2.\text{ord.}}$	$\Delta E_{\text{quad-uehl}}$	E_{tot}
$^{185}_{75}\text{Re}$	2	$5/2$	$1s_{1/2}$	9394.02	3.21	0.00	9397.23
	6	$13/2$	$1s_{1/2}$	8696.92	2.06	0.00	8698.98
	8	$15/2$	$1s_{1/2}$	8444.32	1.76	0.00	8446.08
	2	$5/2$	$2p_{1/2}$	4083.31	2.18	0.28	4085.77
	3	$5/2$	$2p_{1/2}$	4077.79	2.07	0.23	4080.09
	3	$9/2$	$2p_{3/2}$	3992.27	2.41	0.41	3995.09
	4	$7/2$	$2p_{1/2}$	3957.33	2.10	0.26	3959.69
	3	$5/2$	$2p_{3/2}$	3886.35	1.12	-0.22	3887.25
	5	$7/2$	$2p_{3/2}$	3814.27	2.08	0.28	3816.63
	4	$9/2$	$2p_{1/2}$	3734.93	1.03	-0.27	3735.69
	6	$9/2$	$2p_{3/2}$	3650.57	1.95	0.25	3652.77
	5	$9/2$	$2p_{3/2}$	3556.36	1.13	-0.24	3557.25
	7	$11/2$	$2p_{3/2}$	3458.14	1.85	0.23	3460.22
	6	$11/2$	$2p_{3/2}$	3344.35	0.93	-0.19	3345.09
	8	$13/2$	$2p_{3/2}$	3111.03	0.68	0.02	3111.73
	7	$15/2$	$2p_{3/2}$	2941.66	0.82	-0.15	2942.33
	8	$15/2$	$2p_{3/2}$	2938.52	0.67	-0.16	2939.03
	3	$5/2$	$3d_{3/2}$	1815.47	0.07	0.03	1815.57
	1	$5/2$	$3d_{3/2}$	1804.28	0.11	-0.03	1804.36
	3	$7/2$	$3d_{5/2}$	1783.72	0.05	0.02	1783.79
	0	$5/2$	$3d_{5/2}$	1772.11	0.11	-0.04	1772.18
$^{235}_{92}\text{U}$	3	$7/2$	$1s_{1/2}$	12175.51	6.83	0.00	12182.34
	7	$15/2$	$1s_{1/2}$	11925.50	4.66	0.00	11930.16
	9	$17/2$	$1s_{1/2}$	11835.54	3.54	0.00	11839.08
	3	$7/2$	$2p_{1/2}$	6019.06	5.99	0.85	6025.90
	4	$7/2$	$2p_{1/2}$	6015.01	5.96	0.83	6021.80
	4	$9/2$	$2p_{1/2}$	5979.31	6.02	0.86	5986.19
	5	$9/2$	$2p_{3/2}$	5928.94	6.06	0.88	5935.88
	6	$11/2$	$2p_{3/2}$	5868.85	6.00	0.89	5875.74
	7	$15/2$	$2p_{1/2}$	5798.66	5.30	0.91	5804.87
	8	$15/2$	$2p_{1/2}$	5745.59	4.71	0.87	5751.17
	5	$7/2$	$2p_{3/2}$	5673.10	3.12	-0.42	5675.80
	6	$9/2$	$2p_{3/2}$	5621.02	3.02	-0.46	5623.58
	2	$7/2$	$2p_{3/2}$	5620.12	2.78	-0.56	5622.34
	9	$17/2$	$2p_{1/2}$	5613.24	2.05	0.13	5615.42
	3	$9/2$	$2p_{3/2}$	5586.28	2.81	-0.54	5588.55
	7	$13/2$	$2p_{1/2}$	5556.38	2.60	-0.50	5558.48
	9	$15/2$	$2p_{3/2}$	5493.59	2.44	0.24	5496.27
	8	$15/2$	$2p_{1/2}$	5479.30	2.14	-0.53	5480.91
	10	$17/2$	$2p_{3/2}$	5393.16	1.77	0.13	5395.06
	9	$17/2$	$2p_{3/2}$	5315.81	1.73	-0.44	5317.10
	3	$7/2$	$3d_{3/2}$	2767.16	0.44	0.09	2767.69
	1	$7/2$	$3d_{5/2}$	2663.35	0.61	-0.13	2663.83

2.3 Structure of muonic $^{185}_{75}$Re & $^{187}_{75}$Re

The analysis of x-rays emitted due to transitions in muonic atoms constitutes one possibility to obtain information on the nuclear charge distribution and measure properties like RMS charge radii, or nuclear quadrupole moments. This section analyzes the structure of muonic rhenium-185 and -187. So far, there is no absolute measurement of the charge radius of $^{185}_{75}$Re [202] and the only experiment reported on muonic rhenium is an extraction of the quadrupole moments of $^{185}_{75}$Re and $^{187}_{75}$Re from the N_α x-rays (n=5 $\rightarrow$ n=4) of natural Re [203], which is mainly a mixture of these two isotopes. Therefore, the theoretical spectra of both isotopes have been used at the same time for fitting the experimental spectrum. As a consequence, the two extracted quadrupole moments in Ref. [203] are not indepentent. During the work on this thesis, the quadrupole moments were extracted independently for these two isotopes. The experimental data used in this section comes from measurements of muonic x-rays with isotopically pure rhenium performed in 2016 by the MuX Collaboration. The high intensity muon beam at the Paul Scherrer Institute (Switzerland) [204, 205] was used as a muon source.

In the following, the muonic transition energies and transition probabilities are analyzed, where the methods described in Sections 2.1 and 2.2 are used. Thereby, the dependence of transitions and intensities of the N_α x-rays ($n = 5 \rightarrow n = 4$) on the quadrupole moment is used in combination with experimental data on isotopically pure $^{185}_{75}$Re and $^{187}_{75}$Re to extract the nuclear quadrupole moment. Also, a good qualitative description based on the rigid-rotor nuclear model (Appendix A.4) of the K_α x-rays ($2p \rightarrow 1s$) is given.

After the muon beam hits the target, a muon can be captured in the Coulomb field of an atomic nucleus in a highly excited states. Then, it starts cascading towards the ground state. In principle, this is a complicated many-body probmlem, involing the nucleus, the muon and the atomic electrons. However, there is an intermediate region with $n \approx 4 - 7$, where finite nuclear size effects are still rather small and at the same time, the muon is not influenced significantly by the surrounding atomic electrons. Therefore, the system is essentially hydrogen-like and no many-body problem has to be solved. In addition, the hyperfine structure is mainly determined by the nuclear quadrupole moment. It has been realized, that in this region, more specifically the n=5 $\rightarrow$ n=4 transitions, nuclear quadrupole moments can be extracted, which has been done for lutetium-175 in Ref. [195] and for natural rhenium in Ref. [203]. As a first application of the calculation of muonic spectra presented in this thesis, the dependence of the transition energies and intensities of the muonic N_α x-rays on the nuclear quadrupole moment is calculated, and by comparing to measurements of isotopically pure ^{185}Re and ^{187}Re, a value for their spectroscopic quadrupole moment is extracted.

Following Section 2.1.5, the most intense transitions are the $E1$-transitions in the circular orbits $5g_{9/2} \rightarrow 4f_{7/2}$ and $5g_{7/2} \rightarrow 4f_{7/2}$. However, also the $5f_{7/2} \rightarrow 4d_{5/2}$, $5g_{7/2} \rightarrow 4f_{7/2}$, and $5f_{5/2} \rightarrow 4d_{5/2}$ transitions have to be considered, since they almost coincide in energy with the $5g \rightarrow 4f$ energies around $365\,\mathrm{keV}$. Therefore, the following approach is chosen for the theoretical prediction: The four fine-structure states of the initial states $5g_{9/2}, 5g_{7/2}, 5f_{7/2}, 5f_{5/2}$ together with the nuclear ground state with $I = 5/2$ define a first model space. Now, the formalism described in Section 2.1.4 can be used to

calculate the energies in this modelspace, including finite size effects, vacuum polarization (Uehling, Källen-Sabry, Wichmann-Kroll in point-like approximation, quadrupole-Uehling), and rediagonalization of the electric quadrupole and magnetic dipole hyperfine interaction. In this way, also contributions non-linear in the nuclear quadrupole moment are included, in contrast to [203]. Excited nuclear states were not considered, since the quadrupole interaction in this case is small compared to the nuclear rotational states. For the N_α x-rays, the nuclear energy splitting is around three orders of magnitude larger. Furthermore, due to the small hyperfine splitting in the $n=4,5$ states, the residual second order terms, as described in Section 2.2.2, are very small. The same procedure is repeated for the final states with $n=4$, i.e. $4f_{7/2}$, $4f_{5/2}$, $4d_{5/2}$, $4d_{3/2}$. Then, the transition probabilities can be calculated from each initial to each final state. For this analysis, the relativistic formulas for $E1$ and $M1$ transitions from Section 2.1.5 are used, assuming an initial statistical population $\sim (2F + 1)$ for each initial state with total angular momentum F. Transitions of higher-order multipolarity have a much smaller transition rate. With this approach, every transition energy and corresponding intensity can be calculated for a given nuclear charge distribution

$$\rho_N(r_N, \vartheta_N) = N \left[1 + \exp\left(\frac{r_N - c(1 + \beta \mathrm{Y}_{20}(\vartheta_N))}{a} \right) \right]^{-1},$$

where N is a normalization constant fixed by the condition $\int \mathrm{d}^3\mathbf{r}\rho(r, \vartheta) = Z$. The three parameters a, c, β are calculated using $a = 2.3\,\mathrm{fm}/(4 \ln 3)$, which is a reasonable estimate for most nuclei [126], such that the RMS charge radius agrees with the literature value from Ref. [178], and the spectroscopic quadrupole moment with some given value Q. The connection of the spectroscopic quadrupole Q moment with the nuclear charge distribution for a nucleus with ground state angular momentum I is

$$Q = 4\pi \frac{I(2I - 1)}{(I + 1)(2I + 3)} \int\limits_0^\infty \mathrm{d}r_N \int\limits_0^\pi \mathrm{d}\vartheta_N \, r_N^4 \sin\vartheta_N \rho_N(r_N, \vartheta_N) \mathrm{P}_2(\cos\vartheta_N),$$

where $\mathrm{P}_l(x)$ are the Legendre polynomials from Appendix A.2. The value of the magnetic moment needed for the calculation of the magnetic dipole interaction is taken from [206]. The influence of finite size effects was checked by also using charged shell and homogeneously charged sphere distribution. With this parametrization, the entire spectrum can be calculated for a given spectroscopic quadrupole moment and by fitting the theoretically calculated spectrum to the experimentally measured one, the quadrupole moment can be extracted. There are five groups of $E1$-transitions in energy range of the $5g \to 4f$ transitions, namely:

1. $5g_{9/2} \to 4f_{7/2}$

2. $5g_{7/2} \to 4f_{5/2}$

3. $5f_{7/2} \to 4d_{5/2}$

4. $5g_{7/2} \to 4f_{7/2}$

    5. $5f_{5/2} \to 4d_{5/2}$

Each of those groups consists of 15 or 16 individual lines itself due to the hyperfine structure. Therefore, 77 individual lines and corresponding intensities are taken into account in the fitting process.

    The difference between two transition energies is especially sensitive to the quadrupole moment, since the majority of the uncertainty due to the nuclear RMS radius cancels, as described in Ref. [203]. Therefore, the energy differences of all $5g_{9/2} \to 4f_{7/2}$ transition compared to the most intense transition in this group, called the centroid transition, is calculated and analogously the corresponding intensities are given relative to the centroid transition. The same holds for the other four groups. Then, the energy difference of the $5g_{9/2} \to 4f_{7/2}$ centroid compared to the other four centroids is calculated. Thereby, the energy differences of all considered transitions compared to the $5g_{9/2} \to 4f_{7/2}$ centroid is parametrized in terms of the nuclear quadrupole moment, and the position of the $5g_{9/2} \to 4f_{7/2}$ centroid can be fitted to the experimental spectrum as a free parameter. The relative intensities of the 5 different groups are either free fit parameters or obtained from other programs for cascade calculations [207]. Since it is too expensive to perform full calculations in the fitting process to experimental data, the full calculations are performed for several values of the quadrupole moment in the proximity of the expected value and are fitted by a quadratic function for every transition energy and intensity as

$$\Delta E^{if}(Q) = \Delta E_0^{if} + \Delta E_1^{if} Q + \Delta E_2^{if} Q^2, \tag{2.53}$$

$$I^{if}(Q) = I_0^{if} + I_1^{if} Q + I_2^{if} Q^2. \tag{2.54}$$

The fitted function and the results from the full calculations agree on the 10^{-4} eV level in the region of the determined quadrupole moment. The resulting dependencies for $^{185}_{75}$Re are given in Table 2.10 for the relative transition energies, in Table 2.11 for the intensities, and in Table 2.9 for fitted energy differences of the centroid transitions. For $^{187}_{75}$Re, the coefficients differ only to a small extent due to different values for the magnetic moment and RMS charge radius and the corresponding tables are given in Appendix A.5. A main experimental challenge is understanding of the line shape due to the detector response function, which broadens the Lorentzian (due to natural life time) essentially into a Voigt profile. This issue is treated in Ref. [208] in detail.

    The calculated spectrum parametrized by the nuclear quadrupole moment can now be fitted efficiently to the experimental spectrum and the result is shown in Fig. 2.6. The $5f_{5/2} \to 4d_{5/2}$ group turned out not to be visible in the fit. Thereby, the *preliminary* extracted spectroscopic quadrupole moment of $^{185}_{75}$Re and $^{187}_{75}$Re is obtained as

$$Q_{\text{Re-185}} = 2.11(2)(7) \, \text{barn},$$
$$Q_{\text{Re-187}} = 1.96(2)(2) \, \text{barn},$$

where the number in the first bracket is the statistical uncertainty and the number in the second bracket is the systematic uncertainty due to the ratio of the intensities. The value is in agreement with the previous literature values [189].

    Furthermore, the low-lying $2p \to 1s$ transitions, or K_α x-rays, have been measured

during the same experiments. The assumption of statistically populated $5g$ states, i.e. $\sim (2F+1)$, and a cascade $5g \to 4f \to 3d \to 2p \to 1s$ as discussed in Sections 2.1.4 and 2.1.5 can explain the spectrum qualitatively, using the rigid rotor model for the nucleus (Appendix A.4). The corresponding comparison for the K_α x-rays ($2p \to 1s$) is shown in Fig. 2.7. For the calculations of the spectra, the first five nuclear rotational states have been considered. In principle, from these spectra, the nuclear RMS radius can be extracted [73]. However, for the low-lying transitions in heavy muonic atoms, the nuclear polarization corrections, e.g. [199], have to be included into the theoretical predictions. These corrections are due to virtual excitations of nuclear states beyond the rigid rotor model and have to be treated with a more accurate nuclear model or experimental data on nuclear transitions. Thus, updated calculations from the nuclear physics side would be highly desirable together with the calculations for the bound muon as presented in this thesis in connection with the new experimental campaign on muonic atoms. This is also discussed in more detail in the conclusion & outlook chapter.
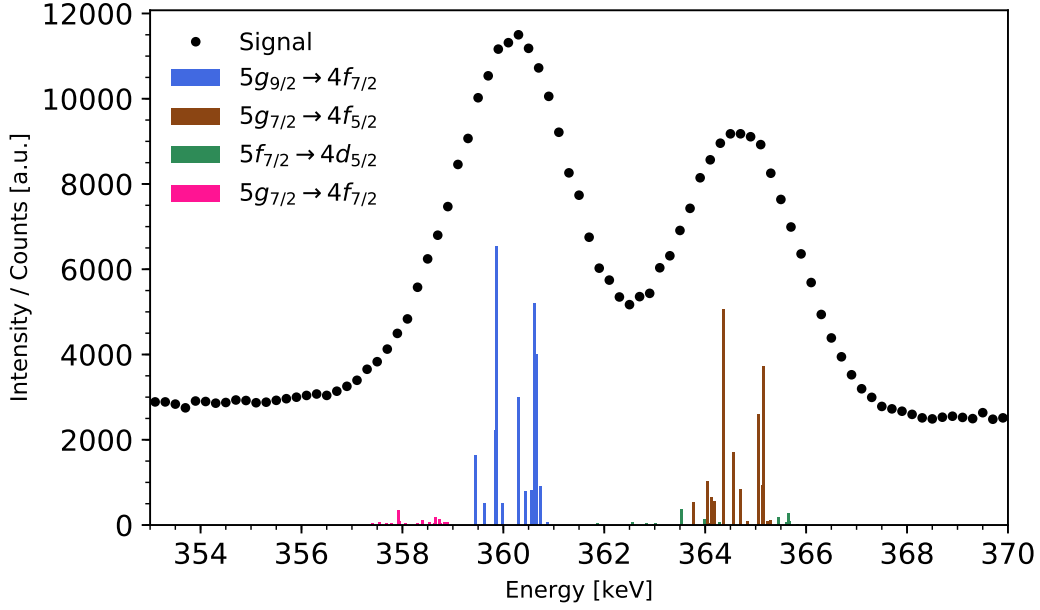
(a)
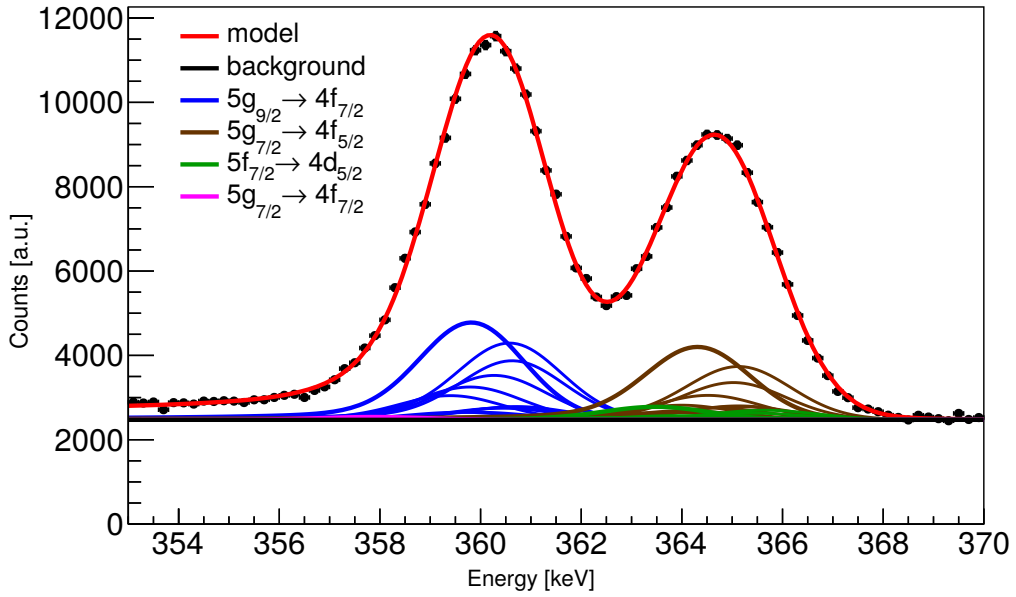
(b)

Figure 2.6: Comparison of the experimental data and theoretical predictions in region of the $5g_{9/2} \to 4f_{7/2}$, $5g_{7/2} \to 4f_{7/2}$, $5f_{7/2} \to 4d_{5/2}$, $5g_{7/2} \to 4f_{7/2}$ groups in $^{185}_{75}$Re. The black dots are the measurements and the nuclear quadrupole moment of $^{185}_{75}$Re has been extracted by fitting the theoretical prediction to the data. In part (a), the colored lines show the calculated transition energies and corresponding transition probabilities. In part (b), the predicted signals for each transition are shown [207]. The center corresponds to the calculated transition probability and the shape is given by the natural line width and the detector response function. The red function represents the calculated total signal and is the sum of all separate signals. Details about the calculations can be found in Section 2.3, and about the detector response function in Ref. [208].
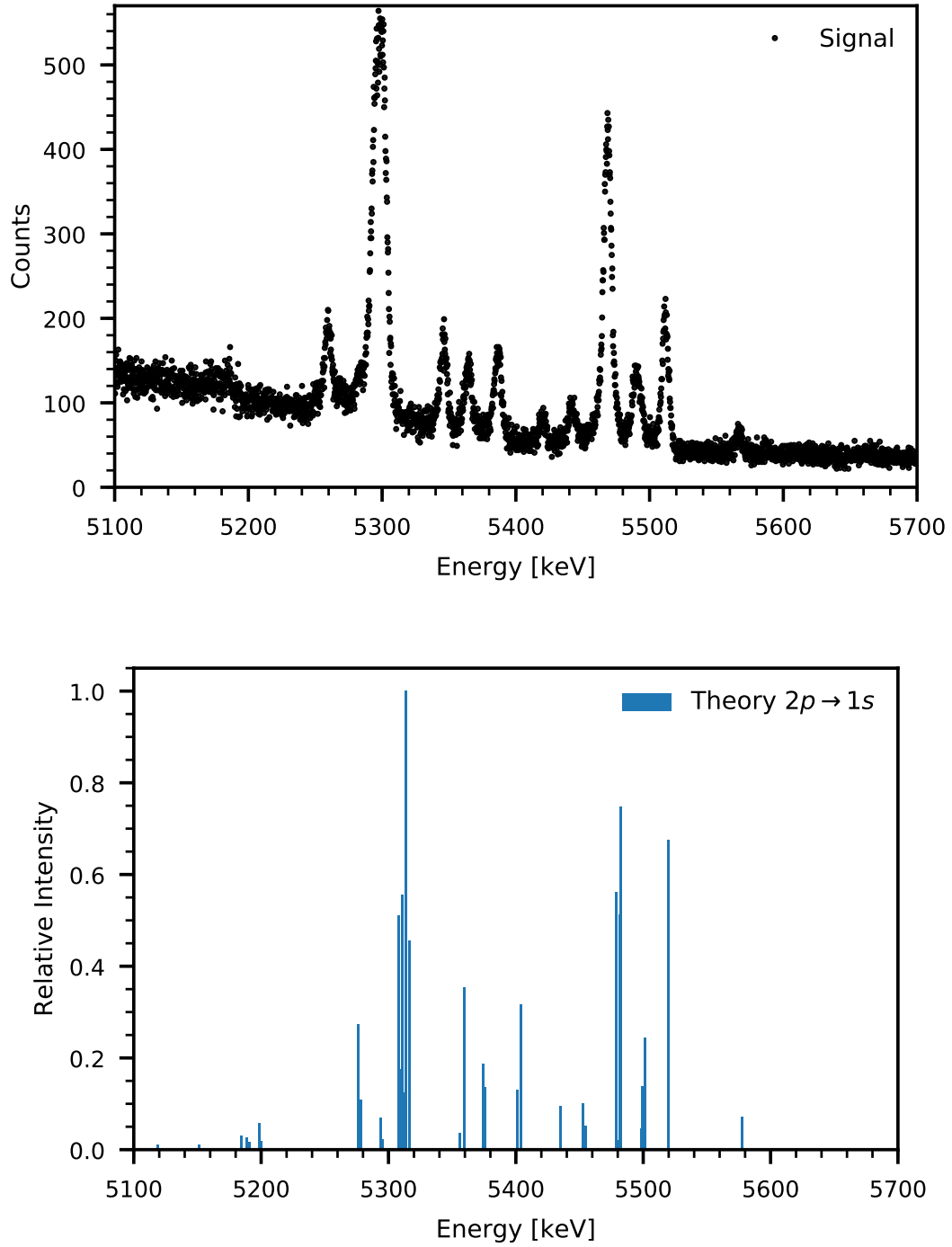
Figure 2.7: Comparison of experimental spectrum (upper plot) and theoretical calculations (lower plot) in the area of the K_α x-rays for muonic $^{185}_{75}$Re. The first 5 rotational states of the $^{185}_{75}$Re nucleus and a muonic cascade starting from statistically populated $5g$ states have been used for the calculations. The spectrum is complex due to excited nuclear states and large hyperfine splitting in the muonic $2p$ states. The small shift of the theoretical values is due to the non-calculated nuclear polarization corrections. For further details, see Section 2.3.

Table 2.9: Quadratic fits of the energies of the centroid transitions for $^{185}_{75}$Re. The formula for the energy difference in terms of a give quadrupole moment Q is given in Eq. (2.53). See Section 2.3 for details.

centroid	$F_i \to F_f$	ΔE_2^{if}[keV/barn^2]	ΔE_1^{if}[keV/barn]	ΔE_0^{if}[keV]
$5g_{9/2} \to 4f_{7/2}$	$7 \to 6$	0.0000	-0.1743	360.2145
$5g_{7/2} \to 4f_{5/2}$	$6 \to 5$	0.0040	-0.1601	364.6631
$5f_{7/2} \to 4d_{5/2}$	$6 \to 5$	-0.0016	-0.4396	364.4165
$5g_{7/2} \to 4f_{7/2}$	$6 \to 6$	-0.0004	-0.1775	358.2798
$5f_{5/2} \to 4d_{5/2}$	$5 \to 5$	-0.0039	-0.4480	361.1407

Table 2.10: Quadratic fits of the transitions energies compared to the most intense (centroid) transition for the most intense transitions for the $5g_{9/2} \to 4f_{7/2}$, $5g_{7/2} \to 4f_{7/2}$, $5f_{7/2} \to 4d_{5/2}$, $5g_{7/2} \to 4f_{7/2}$, and $5f_{5/2} \to 4d_{5/2}$ groups in $^{185}_{75}$Re. The absolute transition energies of the centroid transitions are given in Table 2.9. The formula for the transition energy in terms of a give quadrupole moment Q is given in Eq. (2.53). See Section 2.3 for details.

Group	$F_i \to F_f$	ΔE_2^{if}[eV/barn^2]	ΔE_1^{if}[eV/barn]	ΔE_0^{if}[eV]
$5g_{9/2} \to 4f_{7/2}$	$7 \to 6$	0.0000	0.0000	0.0000
	$6 \to 6$	0.4349	-112.8421	-4.3710
	$6 \to 5$	-3.9990	374.5405	8.1664
	$5 \to 6$	0.0083	-130.4566	-8.6014
	$5 \to 5$	-4.4255	356.9260	3.9360
	$5 \to 4$	-0.0011	385.3921	20.3954
	$4 \to 5$	-4.3353	397.2028	0.5956
	$4 \to 4$	0.0891	425.6690	17.0550
	$4 \to 3$	-1.3357	210.0265	28.0955
	$3 \to 4$	0.2441	494.0067	14.3378
	$3 \to 3$	-1.1807	278.3642	25.3784
	$3 \to 2$	-2.3757	-23.6926	33.7363
	$2 \to 3$	-1.2154	350.5410	23.3930
	$2 \to 2$	-2.4104	48.4842	31.7510
	$2 \to 1$	-1.5016	-218.4484	36.5602
$5g_{7/2} \to 4f_{5/2}$	$6 \to 5$	0.0000	0.0000	0.0000
	$5 \to 5$	0.4268	-116.6524	-6.0881
	$5 \to 4$	-4.0133	397.3030	15.1612
	$4 \to 5$	0.3365	-124.8666	-11.3476
	$4 \to 4$	-4.1035	389.0888	9.9017
	$4 \to 3$	-2.6732	339.4603	29.0257
	$3 \to 4$	-4.2588	440.6240	5.7383
	$3 \to 3$	-2.8284	390.9955	24.8623
	$3 \to 2$	-1.6187	86.2278	39.1264

Group	$F_i \to F_f$	ΔE_2^{if} [eV/barn^2]	ΔE_1^{if} [eV/barn]	ΔE_0^{if} [eV]
		(continuation from previous page)		
	$2 \to 3$	-2.7939	463.6869	21.6868
	$2 \to 2$	-1.5843	158.9191	35.9509
	$2 \to 1$	-2.4783	-172.9226	46.2225
	$1 \to 2$	-1.3654	223.6477	33.7757
	$1 \to 1$	-2.2595	-108.1940	44.0473
	$1 \to 0$	-3.9788	-312.5737	49.2916
$5f_{7/2} \to 4d_{5/2}$	$6 \to 5$	0.0000	0.0000	0.0000
	$5 \to 5$	2.3569	-252.5291	-6.3945
	$5 \to 4$	-39.2156	1142.4006	-7.6361
	$4 \to 5$	0.0075	-267.1910	-14.9468
	$4 \to 4$	-41.5650	1127.7387	-16.1884
	$4 \to 3$	-2.9973	940.7303	47.5074
	$3 \to 4$	-40.8162	1239.4485	-21.8866
	$3 \to 3$	-2.2485	1052.4401	41.8091
	$3 \to 2$	-21.1329	231.4531	70.3569
	$2 \to 3$	-1.6192	1208.9013	37.4969
	$2 \to 2$	-20.5036	387.9143	66.0447
	$2 \to 1$	-23.4328	-470.1437	68.4933
	$1 \to 2$	-20.9818	526.1606	63.5780
	$1 \to 1$	-23.9109	-331.8974	66.0266
	$1 \to 0$	1.6436	-869.1530	73.0235
$5g_{7/2} \to 4f_{7/2}$	$6 \to 6$	0.0000	0.0000	0.0000
	$6 \to 5$	-4.4339	487.3826	12.5375
	$5 \to 6$	0.4268	-116.6524	-6.0881
	$5 \to 5$	-4.0071	370.7302	6.4493
	$5 \to 4$	0.4173	399.1963	22.9087
	$4 \to 5$	-4.0974	362.5159	1.1898
	$4 \to 4$	0.3270	390.9821	17.6492
	$4 \to 3$	-1.0978	175.3397	28.6898
	$3 \to 4$	0.1718	442.5174	13.4858
	$3 \to 3$	-1.2530	226.8749	24.5264
	$3 \to 2$	-2.4480	-75.1819	32.8844
	$2 \to 3$	-1.2185	299.5663	21.3508
	$2 \to 2$	-2.4135	-2.4905	29.7088
	$2 \to 1$	-1.5047	-269.4231	34.5180
	$1 \to 2$	-2.1947	62.2380	27.5336
	$1 \to 1$	-1.2858	-204.6945	32.3428
$5f_{5/2} \to 4d_{5/2}$	$5 \to 5$	0.0000	0.0000	0.0000
	$5 \to 4$	-41.5725	1394.9297	-1.2415
	$4 \to 5$	2.3621	-267.5452	-10.8732
		(continued on next page)		

Group	$F_i \to F_f$	ΔE_2^{if} [eV/barn^2]	ΔE_1^{if} [eV/barn]	ΔE_0^{if} [eV]
		(continuation from previous page)		
	$4 \to 4$	-39.2104	1127.3845	-12.1147
	$4 \to 3$	-0.6427	940.3761	51.5811
	$3 \to 4$	-39.9636	1153.2006	-21.9500
	$3 \to 3$	-1.3959	966.1922	41.7458
	$3 \to 2$	-20.2803	145.2052	70.2936
	$2 \to 3$	-2.0370	1124.7959	34.4113
	$2 \to 2$	-20.9214	303.8089	62.9591
	$2 \to 1$	-23.8506	-554.2491	65.4077
	$1 \to 2$	-20.4551	476.5200	57.6634
	$1 \to 1$	-23.3843	-381.5380	60.1120
	$1 \to 0$	2.1702	-918.7936	67.1089
	$0 \to 1$	-22.4779	-275.1695	57.4097

Table 2.11: Quadratic fits of the relative intensities for the most intense transitions each for the $5g_{9/2} \to 4f_{7/2}$, $5g_{7/2} \to 4f_{7/2}$, $5f_{7/2} \to 4d_{5/2}$, $5g_{7/2} \to 4f_{7/2}$, and $5f_{5/2} \to 4d_{5/2}$ groups in $^{185}_{75}$Re. The intensities are given relative to the most intense (cenroid) transition. The formula for the transition energy in terms of a give quadrupole moment Q is given in Eq. (2.54). See Section 2.3 for details.

Group	$F_i \to F_f$	I_2^{if} [%/barn^2]	I_1^{if} [%/barn]	I_0^{if} [%]
$5g_{9/2} \to 4f_{7/2}$	$7 \to 6$	0.000	0.000	100.000
	$6 \to 6$	-0.011	-0.115	8.045
	$6 \to 5$	-0.008	0.383	78.602
	$5 \to 6$	0.000	-0.002	0.311
	$5 \to 5$	-0.012	0.036	12.375
	$5 \to 4$	0.000	0.214	60.644
	$4 \to 5$	-0.001	0.012	0.669
	$4 \to 4$	-0.001	0.109	13.527
	$4 \to 3$	-0.002	0.007	45.818
	$3 \to 4$	0.000	0.019	0.837
	$3 \to 3$	-0.001	0.104	11.900
	$3 \to 2$	-0.002	-0.102	33.944
	$2 \to 3$	0.000	0.013	0.619
	$2 \to 2$	-0.001	0.050	7.725
	$2 \to 1$	-0.001	-0.105	25.000
$5g_{7/2} \to 4f_{5/2}$	$6 \to 5$	0.000	0.000	100.000
	$5 \to 5$	0.022	0.218	12.062
	$5 \to 4$	0.036	0.360	72.591
	$4 \to 5$	0.003	0.024	0.730
	$4 \to 4$	0.008	0.088	18.102
	$4 \to 3$	0.021	0.397	50.423

(continued on next page)

Group	$F_i \to F_f$	$I_2^{if}[\%/\text{barn}^2]$	$I_1^{if}[\%/\text{barn}]$	$I_0^{if}[\%]$
	(continuation from previous page)			
	$3 \to 4$	0.001	0.009	1.642
	$3 \to 3$	0.012	-0.046	19.212
	$3 \to 2$	0.013	0.257	33.003
	$2 \to 3$	0.002	-0.022	2.192
	$2 \to 2$	0.009	-0.097	16.477
	$2 \to 1$	0.009	0.094	19.797
	$1 \to 2$	0.001	-0.027	1.829
	$1 \to 1$	0.004	-0.078	10.989
	$1 \to 0$	0.005	-0.008	10.262
$5f_{7/2} \to 4d_{5/2}$	$6 \to 5$	0.000	0.000	100.000
	$5 \to 5$	-0.041	-0.307	12.106
	$5 \to 4$	-0.106	1.215	72.304
	$4 \to 5$	0.000	-0.002	0.738
	$4 \to 4$	-0.106	0.343	18.040
	$4 \to 3$	-0.007	0.381	50.338
	$3 \to 4$	-0.016	0.086	1.639
	$3 \to 3$	-0.002	0.330	19.267
	$3 \to 2$	-0.019	-0.188	32.976
	$2 \to 3$	-0.001	0.097	2.206
	$2 \to 2$	-0.009	0.170	16.510
	$2 \to 1$	-0.018	-0.275	19.773
	$1 \to 2$	0.000	0.056	1.836
	$1 \to 1$	-0.010	0.009	10.995
	$1 \to 0$	0.000	-0.157	10.257
$5g_{7/2} \to 4f_{7/2}$	$6 \to 6$	0.000	0.000	100.000
	$6 \to 5$	0.722	1.664	10.899
	$5 \to 6$	-0.010	-0.401	10.234
	$5 \to 5$	-0.117	-8.661	68.235
	$5 \to 4$	0.022	-1.370	15.636
	$4 \to 5$	-0.009	-1.686	15.656
	$4 \to 4$	0.101	-3.994	44.693
	$4 \to 3$	0.210	-3.201	16.754
	$3 \to 4$	0.019	-1.220	16.889
	$3 \to 3$	-0.120	0.243	28.837
	$3 \to 2$	0.149	-2.527	14.555
	$2 \to 3$	-0.054	0.005	14.624
	$2 \to 2$	-0.166	1.893	19.289
	$2 \to 1$	0.015	-0.887	9.296
	$1 \to 2$	-0.066	0.637	9.265
	$1 \to 1$	-0.128	1.955	16.650

Group	$F_i \rightarrow F_f$	I_2^{if} [%/barn^2]	I_1^{if} [%/barn]	I_0^{if} [%]
	(continuation from previous page)			
$5f_{5/2} \rightarrow 4d_{5/2}$	$5 \rightarrow 5$	0.000	0.000	100.000
	$5 \rightarrow 4$	1.842	3.914	17.965
	$4 \rightarrow 5$	-0.008	-1.155	16.736
	$4 \rightarrow 4$	0.792	-16.181	56.816
	$4 \rightarrow 3$	0.382	-5.451	24.306
	$3 \rightarrow 4$	0.130	-5.071	24.769
	$3 \rightarrow 3$	-0.002	-1.881	25.862
	$3 \rightarrow 2$	0.644	-7.174	24.558
	$2 \rightarrow 3$	-0.017	-1.687	24.986
	$2 \rightarrow 2$	-0.278	3.084	8.988
	$2 \rightarrow 1$	0.079	-3.215	20.127
	$1 \rightarrow 2$	-0.351	2.589	19.702
	$1 \rightarrow 1$	0.043	1.509	1.602
	$1 \rightarrow 0$	-0.122	0.943	10.821
	$0 \rightarrow 1$	-0.154	3.105	10.510

2.4 Conclusion

In this chapter, the following results have been presented:

- An state-of-the-art numerical approach, namely the dual-kinetic-balance method based on B-splines, has been used for fully relativistic precision calculations in muonic atoms. Many important contributions have been implemented, like finite nuclear size effects, magnetic and electric hyperfine interactions, electron screening, and the most important QED corrections.

- The calculations include the level mixing of low-lying nuclear rotational states and muonic fine-structure components due to strong electric quadrupole interaction. The transition energies and probabilities were calculated in this framework in a fully relativistic approach, which enables an accurate theoretical prediction of the observed spectra of heavy muonic atoms.

- Additionally, enhanced numerical approaches for the calculation of the quadrupole vacuum polarization correction in the Uehling approximation and for the treatment of residual second order quadrupole interactions have been presented. The extended nuclear charge distribution is described exactly and kept as such in our calculations, and not expanded in a low-order power series.

- The nuclear spectroscopic quadrupole moment of $^{185}_{75}$Re and $^{187}_{75}$Re was extracted by fitting theoretical spectra to the experimental ones in connection with measurements of isotopically pure muonic rhenium perfomed by the MuX collaboration at the Paul Scherrer Institute in 2016. Also, the spectrum of the low-lying transitions was calculated and is in a good qualitative agreement with the measured one. This provides a solid basis for the extraction of further nuclear parameters in the future, including both rhenium and other elements.

Chapter 3

Nuclear shape effects on the bound-electron g factor

In this chapter, non-perturbative calculations of the nuclear deformation (ND) correction to the bound-electron g factor are presented. Results for nuclei across the entire nuclear chart are shown, quantifying the higher-order corrections in the values of the g factor. Furthermore, it is shown how the model dependence and therefore uncertainty of the finite nuclear size correction can be reduced by using deformed nuclear charge distributions and that, in this connection, numerical calculations are necessary for obtaining precise results. A part of the work described in this chapter was submitted for publication in Ref. [4]. In Sections 3.1, 3.2, and 3.3, a motivation and a brief summary of the theory for the bound-electron g factor for spinless nuclei is given. In Section 3.4, the definition of the ND correction from Ref. [144] is given and the numerical approach for its calculation from this thesis is compared to the previously used perturbative method.

3.1 Motivation

The electron's g factor characterizes its magnetic moment in terms of its angular momentum. For an electron bound to an atomic nucleus, the g factor can be predicted in the framework of bound-state quantum electrodynamics (QED) as well as measured in Penning traps, both with a very high degree of accuracy, e.g. [108, 110]. This enables extraction of information on fundamental interactions, constants and nuclear structure. For example, the combination of theory and precise measurements of the bound electron g factor has recently provided an improved value for the electron mass [108], and bound-state QED in strong fields was tested with unprecedented precision [107, 109, 145, 146]. It also enables measurements on characteristics of nuclei such as electric charge radii, as shown for $^{28}_{14}\mathrm{Si}^{13+}$ [110], or the isotopic mass difference as demonstrated for $^{48}_{20}\mathrm{Ca}^{17+}$ and $^{40}_{20}\mathrm{Ca}^{17+}$ in Ref. [112], or, as proposed theoretically, nuclear magnetic moments [147]. Also, it was argued that g-factor experiments with heavy ions could result in a independent determination of the fine-structure constant, which is more accurate than the presently established one [149, 150]. With planned experiments involving high Z nuclei [115, 118, 209] and current experimental accuracies on the 10^{-10} level for low Z, it is important to keep track also of higher-order effects. In this context, besides one-loop QED corrections [129, 134] which are well under control, two-loop QED corrections [123–125, 135] which requires further investigations, and nuclear polarization [138, 139], also the influence of nuclear size [120, 137] and shape is critical. In Refs. [144, 210], the nuclear shape correction to the

bound-electron g factor was introduced and calculated for spinless nuclei using the perturbative effective-radius method (ERM) [187,211]. This effect accounts for the influence of a deformed nuclear charge distribution and changes the g factor up to a 10^{-6} level for heavy nuclei, thus being potentially important for future experiments. Additionally, the uncertainty of the finite nuclear size correction to the Lamb shift in hydrogenlike $^{238}_{92}$U was shown to be sensitive on nuclear deformation effects [187]. This motivates the possibility of lowering the uncertainties for the g factor by considering ND. Therefore, a comparison of experiment and theory for heavy nuclei demands a further improvement and critical scrutiny of the validity of the previously used perturbative methods, as pointed out in Ref. [212].

3.2 Averaged nuclear potential

In this section, the electric interaction energy between a spinless atomic nucleus, described by a rigid rotor model (Appendix A.4), and an electron in a hydrogen-like ion is investigated, following [144, 187]. In Chapter 1, it was shown that to leading order the bound-state energies can be obtained by solving the Dirac equation for the electron in the nuclear potential. For a rigid rotor, the charge density $\rho(\mathbf{r}'_N)$ is given in the nuclear body-fixed frame, and the position of the body fixed frame in the laboratory frame is described in terms of the Euler angles (ϕ, θ, ψ). In the following, primed coordinates refer to the body-fixed system and unprimed coordinates to the laboratory system, and vectors are written in spherical coordinates as $\mathbf{r}_i = (r_i, \vartheta_i, \varphi_i)$. The passive picture of rotations is used, i.e. the vectors are considered as invariant geometric objects and the Euler angles are used to describe the rotations of the coordinate axes. The electric potential energy of an electron at position $\mathbf{r}'_e$ due to the nuclear electric field is

$$V(\mathbf{r}'_e) = -Z\alpha \int \mathrm{d}^3\mathbf{r}'_N \frac{\rho(\mathbf{r}'_N)}{|\mathbf{r}'_e - \mathbf{r}'_N|}.$$

Now, the denominator is expanded in spherical multipoles [180] without any assumptions about the distance of nuclear charge distribution and electron, which results in radial distribution functions of the l-th multipoles, instead of the usual scaling $\sim 1/r^{l+1}$. Hereby, the potential is rewritten as

$$V(\mathbf{r}'_e) = \sum_{l=0}^{\infty} \sum_{m=-l}^{l} V_{lm}(\mathbf{r}'_e) = -Z\alpha \sum_{l=0}^{\infty} \sum_{m=-l}^{l} \int \mathrm{d}^3\mathbf{r}'_N \frac{r_<^l}{r_>^{l+1}} \rho(\mathbf{r}'_N) C^*_{lm}(\vartheta'_N, \varphi'_N) C_{lm}(\vartheta'_e, \varphi'_e),$$

(3.1)

where $r_> = \max(r'_N, r'_e)$, $r_< = \min(r'_N, r'_e)$, and $C_{lm}(\vartheta, \varphi) = \sqrt{4\pi/(2l + 1)}Y_{lm}(\vartheta, \varphi)$ are the normalized spherical harmonics. Since the laboratory frame and the body-fixed frame are related by a rotation, the length of vectors stays the same, i.e. $r'_i = r_i$. Since the angular variables are separated by the multipole expansion, the electronic angles can be transformed to the laboratory system in a simple way, while keeping the nuclear variables in the body-fixed frame. The body-fixed variables ϑ'_e, φ'_e are in general a function of the laboratory ϑ_e, φ_e and the Euler angles (ϕ, θ, ψ). For the special case of spherical

harmonics, the connection is

$$C_{l0}(\vartheta'_e, \varphi'_e) = \sum_{\tilde{m}=-l}^{l} C^*_{l\tilde{m}}(\theta, \phi) C_{l\tilde{m}}(\vartheta_e, \varphi_e).$$

Furthermore, nuclear polarization effects [138] are neglected, so it is assumed that the nucleus is in its ground state only and the interaction with the electron does not induce virtual nuclear transitions. This assumption is a valid approximation, since the typical nuclear energy scales are on the order of $100\,\text{keV}$, which is much larger than typical energies in atomic physics. Under these conditions, the nuclear degrees of freedom can be integrated out via the expectation value of the electric potential with the nuclear ground state wave functions, which correspond in the rigid rotor model to $I = M = K = 0$. Due to the vanishing nuclear spin, only $l = m = \tilde{m} = 0$ terms are non-zero, and the potential (3.1) reduces to

$$V(r_e) = -Z\alpha \int \mathrm{d}^3 \mathbf{r}'_N \frac{\rho(\mathbf{r}'_N)}{r_>} \tag{3.2}$$

$$= -\frac{Z\alpha}{r_e} 4\pi \int_0^{r_e} \mathrm{d}r'_N r'^2_N \rho_0(r'_N) - Z\alpha 4\pi \int_{r_e}^{\infty} \mathrm{d}r'_N r'_N \rho_0(r'_N),$$

with the averaged charge distribution

$$4\pi\rho_0(r'_N) = \int_0^{2\pi} \mathrm{d}\varphi'_N \int_0^{\pi} \mathrm{d}\vartheta'_N \sin\theta \, \rho(\mathbf{r}'_N). \tag{3.3}$$

Thus, for spinless nuclei, the potential is spherically symmetric, although the charge distribution of the nucleus does not have to be. Therefore, the theory of the bound-electron g factor in a spherical potential can be applied also in this case.

3.3 Bound-electron g factor in central potentials

In the previous subsection, it was shown that for spinless nuclei the electric potential for a bound electron is still spherically symmetric, even for deformed nuclear charge distributions. Therefore, in this section, the theory of the g factor in a spherically symmetric potential is presented, following [169, 213]. A more detailed introduction can be found in Ref. [214]. In a weak, homogeneous magnetic field, the g factor is determined by the energy splitting, which is linear in the field strength. Therefore, an electron moving in an arbitrary central potential $V(r)$ of the nucleus and in a homogeneous magnetic field $\mathbf{B}$ is considered. The z axis is aligned along the magnetic field, i.e. $\mathbf{B} = B\mathbf{e}_z$, where $\mathbf{A}(\mathbf{r}) = \mathbf{B} \times \mathbf{r}/2$ is the corresponding vector potential in Coulomb gauge. The stationary Dirac equation for the electron thereby reads as

$$[\boldsymbol{\alpha} \cdot \mathbf{p} + \beta m_e + V(r) - e\boldsymbol{\alpha} \cdot \mathbf{A}(\mathbf{r})] \, |\psi\rangle = E \, |\psi\rangle \, .$$

Since for the g factor in a weak field only the energy splitting linear in the magnetic field strength is needed, it is enough to solve the Dirac equation with the nuclear potential as

$$[\boldsymbol{\alpha} \cdot \mathbf{p} + \beta m_e + V(r)] \left|n\kappa m\right\rangle = E \left|n\kappa m\right\rangle,$$

where the methods for spherical potentials presented in Section 1.2 can be used. Then, the first order energy splitting due to the magnetic field is considered as

$$\Delta E_B = -e \left\langle n\kappa m\right| \boldsymbol{\alpha} \cdot \mathbf{A}(\mathbf{r}) \left|n\kappa m\right\rangle. \tag{3.4}$$

The g factor is defined as the proportionality coefficient between the energy shift and the external magnetic field B as

$$\Delta E_B = m \, g \mu_B B,$$

with the Bohr magneton $\mu_B = |e|\hbar/(2m_e)$ and the magnetic quantum number m. Following Ref. [215] for the calculation of the matrix element in Eq. (3.4), the g factor can be calculated as

$$g = \frac{2m_e\kappa}{j(j+1)} \int_0^\infty \mathrm{d}r r^3 f_{n\kappa}(r) g_{n\kappa}(r). \tag{3.5}$$

It has been shown in Ref. [213], that the radial integral in Eq. (3.5) is related to the derivative of the electron energies with respect to its mass. As a first step, a transformation of the radial integral in Eq. (3.5) can be performed. For this, the first line of the radial equations (1.20) is multiplied by $g(r)$ and the second line is multiplied by $f(r)$. Then, the sum of these equation is independent of the energy E and the potential $V(r)$ and by integrating this sum over r, the following identity of radial integrals is obtained:

$$\int \mathrm{d}r r^3 f(r) g(r) = -\frac{1}{4m_e} \left(1 - 2\kappa \int_0^\infty \mathrm{d}r r^2 (f(r)^2 - g(r)^2) \right).$$

Now, the radial integral on the right hand side can be expressed in terms of the expectation value of the β matrix, using its definition from Appendix A.1, as

$$-\int_0^\infty \mathrm{d}r r^2 (f(r)^2 - g(r)^2) = \left\langle n\kappa m|\beta|n\kappa m\right\rangle$$

Since for potentials which do not depend on the mass of the electron, β can be expressed by the derivative of the Dirac Hamiltonian (1.17) as $\beta = \partial \mathrm{H}_D/\partial m_e$, it follows that

$$\left\langle n\kappa m\right| \beta \left|n\kappa m\right\rangle = \left\langle n\kappa m\right| \partial \mathrm{H}_D/\partial m_e \left|n\kappa m\right\rangle = \partial E_{n\kappa}/\partial m_e,$$

and the g factor (3.5) can be written as

$$g = \frac{-\kappa}{j(j+1)} \left(1 - 2\kappa \frac{\partial E_{n\kappa}}{\partial m_e} \right). \tag{3.6}$$

This formula is valid for arbitrary central potentials and can be used for both numerical and analytical calculations. Using the expression for the energies in the pure Coulomb

potential from Eq. (1.22), the ground state g factor for a point-like nucleus with charge number Z reads as

$$g_{\text{Point}} = \frac{2}{3}\left(1 + 2\sqrt{1 - (Z\alpha)^2}\right),\tag{3.7}$$

a result which can also be obtained by integration of Eq. (3.5) with the known Coulomb wave functions and was reported first by Breit [119].

The resulting bound-electron g factor differs from the point-like value (3.7) for an extended nuclear charge distribution. Correspondingly, the finite nuclear size correction is defined as the difference between the g factor of the extended charge distribution (3.6) and for the point-like nucleus as

$$\delta g_{\text{FS}} = g - g_{\text{Point}}.$$

3.4 Non-perturbative analysis of nuclear shape effects

In this work, we focus on quadrupole deformations and beyond, since atomic nuclei do not possess static dipole moments. Here, the deformed Fermi distribution

$$\rho_{ca\beta_2\beta_4}(r, \vartheta) = N\left[1 + \exp\left(\frac{r - c(1 + \beta_2 Y_{20}(\vartheta) + \beta_4 Y_{40}(\vartheta))}{a}\right)\right]^{-1}\tag{3.8}$$

as a model of the nuclear charge distribution has proved to be very successful, e.g. in heavy muonic atom spectroscopy with deformed nuclei [73,78]. The normal Fermi distribution ($\beta_i = 0$) has also been used in electron-nucleus scattering experiments determining the nuclear charge distribution [216]. Here, a is a skin thickness parameter and c the half-density radius, while β_2, β_4 are deformation parameters. The $Y_{lm}(\vartheta, \varphi)$ are the spherical harmonics and the $Y_{l0}(\vartheta)$ depend only on the polar angle ϑ, and not on the azimuthal angle φ. The normalization constant N is determined by the condition

$$\int \mathrm{d}^3r\, \rho_{ca\beta_2\beta_4}(r, \vartheta) = 1.$$

For the deformed Fermi distribution (3.8) with a fixed charge number Z, the g factor (3.5) is completely determined by the parameters c, a and β_i, and therefore can be written for the ground state as

$$g = g_{\text{point}} + \delta g_{\text{FS}}^{(ca\beta_2\beta_4)},\tag{3.9}$$

where $\delta g_{\text{FS}}^{(ca\beta_2\beta_4)}$ is the finite-size correction depending on the parameters c, a, and β_i. In Ref. [144], the ND correction to the bound electron g factor has been defined as the difference of the finite size effect due to a deformed charge distribution and due to a symmetric charge distribution (i.e. $\beta_i = 0$) with the same nuclear RMS radius as

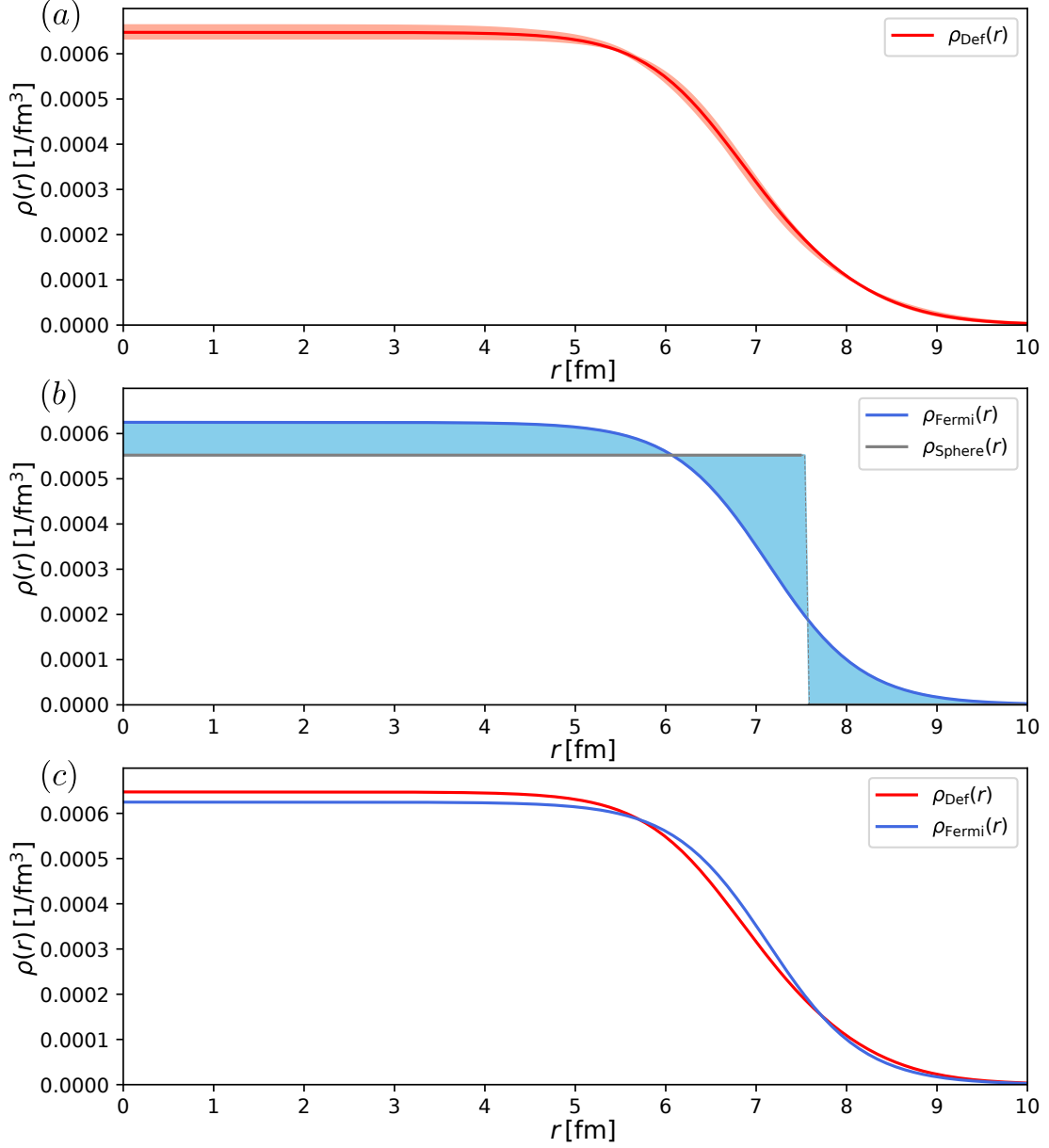$$\delta g_{\text{ND}} = \delta g_{\text{FS}}^{(c_1 a\beta_2\beta_4)} - \delta g_{\text{FS}}^{(c_2 a00)},\tag{3.10}$$

Figure 3.1:
(a): Averaged deformed Fermi distribution from Eq. (3.3) for $^{238}_{92}$U, where the parameters and their uncertainties are taken from [144]. The light red band shows the uncertainties due to the parameters a, β_2, β_4, which is the remaining model uncertainty once the nuclear charge radius is fixed.

(b): (Non-deformed) Fermi distribution and homogeneously charged sphere with the same RMS charge radius as the deformed Fermi distribution. The difference (in light blue) is the conventional model uncertainty of the unclear charge distribution, which is larger compared to using the deformed Fermi distribution in subfigure a).

(c): Comparison of non-deformed and averaged, deformed Fermi distribution with the same RMS radius. The difference causes the nuclear deformation effect.

where $a \approx 2.3 \, \mathrm{fm}/(4\ln(3))$, and c_i are determined such that $\sqrt{\langle r^2 \rangle_\rho}$ of the corresponding charge distribution agrees with the root-mean-square (RMS) values determined experimentally [178]. The n-th moment of a charge distribution $\rho(\mathbf{r})$ is defined as

$$\langle r^n \rangle_\rho = \int \mathrm{d}^3\mathbf{r} \; r^n \rho(\mathbf{r}). \tag{3.11}$$

Values for the deformation parameter β_2 can be obtained from literature values of the reduced electric quadrupole ($E2$) transition probabilities from a nuclear state 2_i^+ to the ground state 0^+ via [217]

$$\beta_2 = \frac{4\pi}{3Z|e|\sqrt{5 \langle r^2 \rangle_\rho /3}} \left[\sum_i B(E2; 0^+ \to 2_i^+) \right]^{1/2}, \tag{3.12}$$

and estimates for β_4 can be found e.g. in Ref. [218]. From Eq. (3.10) it is evident that the ND correction is a difference of two finite-size effects and therefore especially sensitive to higher order effects. For high Z it reaches the 10^{-6} level and therefore it is very significant.

In Ref. [144], $\delta g_{\mathrm{FS}}^{(ca\beta_2\beta_4)}$ and δg_{ND} were calculated with the ERM [211]. It was shown that these mainly depend on the moments $\langle r^2 \rangle_\rho$ and $\langle r^4 \rangle_\rho$ from Eq. (3.11). δg_{ND} can be calculated with the formula [213]

$$\delta g_{\mathrm{FS}}^{(ca\beta_2\beta_4)} = \frac{4}{3} \frac{\partial E_{\mathrm{FS}}(c,a,\beta)}{\partial m_e}, \tag{3.13}$$

which is a direct consequence of Eq. (3.6) and where $E_{\mathrm{FS}}(c,a,\beta_2,\beta_4)$ is the energy correction due to $\rho_{ca\beta_2\beta_4}(r,\vartheta)$ compared to the point-like nucleus.

The effective radius R is defined as the radius of a homogeneously charged sphere with the same energy correction $E_{\mathrm{FS}}^{(\mathrm{sph})}(R)$ as the deformed Fermi distribution via

$$E_{\mathrm{FS}}^{(\mathrm{sph})}(R) \equiv E_{\mathrm{FS}}(c,a,\beta_2,\beta_4). \tag{3.14}$$

The energy correction can be approximated [211] as

$$E_{\mathrm{FS}}^{(\mathrm{sph})}(R) \approx \frac{(Z\alpha)^2}{10} \left[1 + (Z\alpha)^2 f(Z\alpha) \right] (2Z\alpha R m_e)^{2\gamma} m_e. \tag{3.15}$$

Here, $f(x) = 1.380 - 0.162x + 1.612x^2$ and the effective radius is approximately

$$R \approx \sqrt{ \frac{5}{3} \langle r^2 \rangle_{\rho_{ca\beta_2\beta_4}} \left[1 - \frac{3}{4}(Z\alpha)^2 \left(\frac{3}{25} \frac{\langle r^4 \rangle_{\rho_{ca\beta_2\beta_4}}}{\langle r^2 \rangle_{\rho_{ca\beta_2\beta_4}}^2} - \frac{1}{7} \right) \right] }. \tag{3.16}$$

While Eq. (3.13) is exact for an arbitrary central potential, provided that E_{FS} is known exactly, Eq. (3.15) is an approximation derived under the assumption of the difference between point-like and extended potential being a small perturbation. The calculation

of the ND correction to the g factor via the effective radius approach therefore relies on a perturbative evaluation of the energy derivative in Eq. (3.13) and is limited by the accuracy of the finite-size corrections.

In this work, the ND g-factor correction is calculated with three methods. Firstly, with the previously used analytical ERM described above. Secondly, with a numerical ERM, where instead of the approximative Eqs. (3.15) and (3.16), Eq. (3.14) is solved numerically for R and the ND g-factor correction is obtained by using Eq. (3.5) with the wave functions of the corresponding charged sphere. Finally, we also calculate δg_{ND} non-perturbatively by solving the Dirac equation (2.10) numerically with the dual-kinetic-balance method [152] for the potential (3.2), including all finite size effects due to the deformed charge distribution $\rho_{ca\beta}(r, \vartheta)$. Then, the g factors in Eq. (3.10) for the ND correction can be obtained by numerical integration of the wave functions in Eq. (3.5). Alternatively, the derivative of the energies in Eq. (3.6) can be calculated numerically as

$$\frac{\partial E_{n\kappa}}{\partial m_e} \approx \frac{E_{n\kappa}^{(m_e + \delta m_e)} - E_{n\kappa}^{(m_e - \delta m_e)}}{2\delta m_e},$$

with a suitable $\delta m_e / m_e \ll 1$, since the uncertainty of the numerical derivative scales as $(\delta m_e / m_e)^3$. Here, $E_{n\kappa}^{(m_i)}$ stands for the binding energy obtained by solving the Dirac equation with the electron mass replaced by m_i. Both methods were found to be in excellent agreement.

The ND g-factor correction was calculated for a wide range of even-even, both in the proton and neutron number, and therefore spinless nuclei with charge numbers between 16 and 96 using the deformed Fermi distribution from Eq. (3.8) with parameters a, c, and β obtained as described below Eq. (3.10). The required RMS values for the nuclear charge radius are taken from [178] and the reduced transition probabilities needed for the calculation of β_2 via Eq. (3.12) from Ref. [179]. The resulting values for $|\delta g_{\mathrm{ND}}|$, obtained by the non-perturbative method, are shown in Fig. 3.2 as a function of the charge number Z and the neutron number N. If the proton or neutron number is in the proximity of a nuclear magic number 2, 8, 20, 28, 50, 82, and 126, which corresponds to a filled proton or neutron shell [219], the nuclear shell-closure effects also transfer to the g factor, and the ND correction is reduced, as already indicated with the perturbative ERM method in Ref. [214]. In Table 3.2, a comparison between all our numerical approaches and the analytical ERM results from [144] is shown.

Now, let us discuss the main sources for the disagreement of the results obtained with the different approaches, as presented in Table 3.2. Both Eqs. (3.15) and (3.16) are approximations derived by perturbation theory, which affects the accuracy of the analytical ERM $\delta g_{\mathrm{ND}}^{(\mathrm{eff,A})}$. Eq. (3.15) has an estimated relative uncertainty $\lesssim 0.2\,\%$ [211] and (3.16) uses only the second and fourth moment of the nuclear charge distribution for finding the effective radius. Also, it was shown in Ref. [212] that the analytical ERM for arbitrary charge distributions is incomplete in order $(Z\alpha)^2 m_e (Z\alpha m_e R_N)^3$, where R_N is the nuclear RMS charge radius. Furthermore, even if the effective radius is calculated without approximations according to Eq. (3.14), the wave functions of the corresponding homogeneously charged sphere slightly differ from the ones of the deformed Fermi distribution with the same binding energy. This affects values of the g factor and explains the differ-
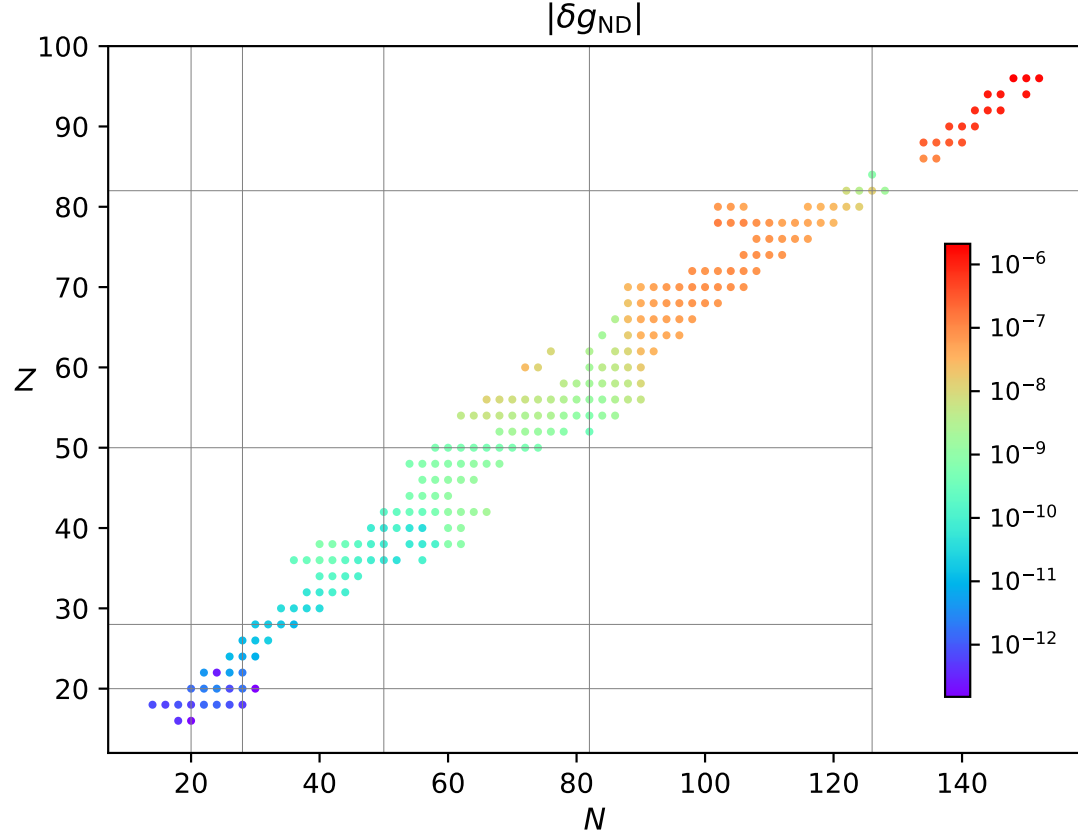
Figure 3.2: Nuclear chart with charge number Z and neutron number N, where the grey lines indicate the magic numbers 20, 28, 50, 82, and 126. The points represent even-even nuclei, where their color displays the magnitude of the ND g-factor correction δg_{ND}, calculated with the numerical, non-perturbative approach, which takes particularly low values around the magic numbers and larger values in between. See [214] for an evaluation with the previously used perturbative method.

ence between the numerical ERM $\delta g_{\mathrm{ND}}^{(\mathrm{eff,N})}$ and the direct numerical calculations $\delta g_{\mathrm{ND}}^{(\mathrm{num})}$. Finally, being a difference of two small finite-nuclear-size corrections, the ND correction can exhibit enhanced sensitivity on the uncertainty of the ERM. From Table 3.2, one can conclude that for high Z, the difference between analytical ERM and non-perturbative calculations is mainly due to the approximations in Eqs. (3.15) and (3.16). The analytical ERM proved to be a good order-of-magnitude estimate of the ND correction, but for high-precision calculations, non-perturbative methods beyond the ERM and without any expansion in $(Z\alpha)$ or $(Z\alpha\, m_e\, R_N)$ are indispensable. Convergence of the numerical methods was checked by varying numerical parameters and using different grids, and the obtained accuracy permits the consideration of nuclear size and shape with an accuracy level much higher than the differences to the perturbative method for the considered nuclei. For low-Z nuclei, however, it becomes increasingly difficult to resolve the small deformation effect with numerical methods. Using double-precision arithmetics, in best case there are 15 to 16 relevant digits in a stored float. Therefore, the small corrections below the 10^{-16} level for light nuclei cannot be resolved. On the other hand, for heavy nuclei the corrections on the 10^{-6} level can be easily seen.

In summary, the ND g-factor correction was calculated non-perturbatively for a wide range of nuclei with quadrupole deformations estimated from nuclear data. By comparing the previously used perturbative ERM and the all-order numerical approach, it was shown that the perturbative ERM overestimates the nuclear deformation correction up to the 20 % level. In the low-Z regime, the ND corrections can safely be neglected, especially for the ions considered in Ref. [108]. However, considering a ND correction up to the parts-per-million level and an expected parts-per-billion accuracy, or even below, for the g-factor experiments with high-Z nuclei, in this case an all-order treatment is indispensable. On the other hand, since the distribution of electric charge inside the nucleus is a major theoretical uncertainty for g factors with heavy nuclei, the extraction of information thereon from experiments is possible. Once QED corrections are known to the required precision, this work demonstrates the required accurate mapping of arbitrary nuclear charge distributions to corresponding g factors.

3.4.1 Reduction of model uncertainty of the finite size g-factor correction

In this part, the connection between nuclear finite size and nuclear deformation correction to the bound-electron g factor is discussed in more detail, since these contributions are intertwined. It is not possible to calculate a value and uncertainty of one of these contribution independently of the other.

Without the consideration of a deformed charge distribution, commonly a non-deformed Fermi distribution (Eq. (3.8) with $\beta_2=\beta_4=0$) which agrees with the RMS radius from literature is used to calculate the finite nuclear size correction. The uncertainty is due to the error in the RMS literature value and also due to model dependence, since even for a fixed RMS value and charge number, there are residual degrees of freedom in the

charge distribution. The uncertainty due to the RMS value can be easily calculated. The uncertainty due to the model dependence is caused by the difference between the Fermi distribution and the true, unknown nuclear charge distribution and is not so easy to estimate. This uncertainty is often estimated as the difference between the effects due to a Fermi distribution and a homogeneously charged sphere, which is considered to be a very conservative estimate [149].

If the finite size correction is calculated as $\delta g_{\mathrm{FS}}^{(ca\beta_2\beta_4)}$ from Eq. (3.9), finite size and deformation effects are already included. Usually, the value of c is determined by the RMS radius from literature. The remaining model uncertainty is reduced to the difference between the deformed Fermi distribution and the true, unknown nuclear charge distribution. As a consequence, precise values for the remaining parameters a, β_2 and β_4 need to be known, e.g. from muonic atom spectroscopy [73, 220]. Furthermore, a reliable estimate of their error bars is needed for the estimate of the difference between deformed Fermi and the true charge distribution. In practice, this leads to a reduced model uncertainty due to the more realistic model of the nuclear charge distribution.

The nuclear deformation effect from Eq. (3.10) was defined in Ref. [144] as the difference of a deformed ($\beta_i \neq 0$) and a normal Fermi distribution ($\beta_i = 0$) for the *same value* of a and the RMS radius. Therefore, the nuclear deformation correction was defined in a model-dependent way, which requires a fixed model for the finite nuclear size correction. As a consequence, the uncertainties of these contributions are not independent. However, for comparison of theoretical and measured values of the g factor, the sum of nuclear finite size and deformation effect is needed. Therefore, an estimation of uncertainties is best performed for $\delta g_{\mathrm{FS}}^{(ca\beta_2\beta_4)}$, which includes both finite size and deformation.

The reduction of model uncertainties is demonstrated in Fig 3.1. Here, the averaged charge distribution for the deformed Fermi distribution for $^{238}_{92}$U with parameters from [144] is shown along with error bars due to the uncertainties in a, c, β_2, and β_4 also according to Ref. [144]. For comparison, the conventional way of estimating the model dependence is also demonstrated by showing the difference between the non-deformed Fermi and charged-sphere charge distribution.

Furthermore, the reduced uncertainties due to consideration of deformation effects are shown for $^{238}_{92}$U in Table 3.1. Parameters and their uncertainties for the RMS radius, a, β_2, and β_4 from Ref. [187] are used. The uncertainty of the finite size g factor correction due to model dependence is reduced by about a factor of 7. Now, the RMS radius error is responsible for the largest part of the total uncertainty. In addition, Table 3.1 shows that the difference of the ERM and the all-order numerical method is larger than the uncertainty due to nuclear parameters.

Table 3.1: Comparison of the finite nuclear size g-factor correction for the (non-deformed) Fermi distribution $\delta g_{\text{FS}}^{(c_1 a00)}$ and the deformed Fermi distribution $\delta g_{\text{FS}}^{(c_2 a\beta_2\beta_4)}$ for $^{238}_{92}$U, evaluated with the effective-radius method (ERM) and numerically. The numbers in the first and second parenthesis are the uncertainties due to the RMS charge radius and the model uncertainty, respectively. Parameters and their uncertainties were taken from Ref. [144]. The results show that considering a deformed charge distribution can significantly reduce the model uncertainty. Furthermore it demonstrates that our numerical method needs to be used for precise calculations.

	ERM	numerical
$\delta g_{\text{FS}}^{(c_1 a00)}$	$1.2842(23)(29) \times 10^{-3}$	$1.2722(23)(23) \times 10^{-3}$
$\delta g_{\text{FS}}^{(c_2 a\beta_2\beta_4)}$	$1.2829(23)(4)\ \times 10^{-3}$	$1.2711(23)(3)\ \times 10^{-3}$

Table 3.2: Comparison of the nuclear deformation g-factor correction obtained by the effective-radius method (ERM) with the analytical expressions from Eqs. (3.15) and (3.16) ($\delta g_{\mathrm{ND}}^{(\mathrm{eff,A})}$), by the ERM with effective radius and corresponding energy correction calculated numerically ($\delta g_{\mathrm{ND}}^{(\mathrm{eff,N})}$) and non-perturbatively by direct numerical calculations ($\delta g_{\mathrm{ND}}^{(\mathrm{num})}$) for several isotopes. R_N is the RMS nuclear electric charge radius from literature [178] and β_2, β_4 are the deformation parameters of the deformed Fermi distribution (3.8). The parameters of the deformed Fermi distribution were either taken from Ref. [144] or calculated as described in the text, where the β_4 values from Ref. [218] were used.

	R_N(fm)	β_2	β_4	$\delta g_{\mathrm{ND}}^{(\mathrm{eff,A})}$	$\delta g_{\mathrm{ND}}^{(\mathrm{eff,N})}$	$\delta g_{\mathrm{ND}}^{(\mathrm{num})}$
$^{58}_{26}$Fe [a]	3.775	0.274	-0.019	-2.10×10^{-11}	-1.95×10^{-11}	-1.99×10^{-11}
$^{82}_{38}$Sr [a]	4.248	0.263	0.001	-3.57×10^{-10}	-3.16×10^{-10}	-3.27×10^{-10}
$^{86}_{38}$Sr [b]	4.226	0.134[c]	0.000	-8.98×10^{-11}	-8.01×10^{-11}	-8.24×10^{-11}
$^{100}_{38}$Sr [b]	4.487	0.435[c]	0.000	-1.08×10^{-09}	-0.97×10^{-09}	-1.00×10^{-09}
$^{98}_{44}$Ru [a]	4.423	0.194	0.038	-6.91×10^{-10}	-6.02×10^{-10}	-6.21×10^{-10}
$^{116}_{48}$Cd [a]	4.620	0.190	-0.038	-1.13×10^{-09}	-0.99×10^{-09}	-1.02×10^{-09}
$^{116}_{50}$Sn [a]	4.625	0.108	-0.008	-5.03×10^{-10}	-4.36×10^{-10}	-4.48×10^{-10}
$^{134}_{54}$Xe [a]	4.790	0.113	0.000	-1.09×10^{-09}	-0.94×10^{-09}	-0.96×10^{-09}
$^{142}_{60}$Nd [b]	4.912	0.100	0.000	-2.01×10^{-09}	-1.71×10^{-09}	-1.76×10^{-09}
$^{150}_{60}$Nd [b]	5.042	0.278	0.000	-1.70×10^{-08}	-1.45×10^{-08}	-1.49×10^{-08}
$^{144}_{62}$Sm [b]	4.945	0.090	0.000	-2.14×10^{-09}	-1.81×10^{-09}	-1.85×10^{-09}
$^{154}_{62}$Sm [b]	5.111	0.328	0.000	-3.24×10^{-08}	-2.75×10^{-08}	-2.82×10^{-08}
$^{152}_{64}$Gd [a]	5.077	0.202	0.050	-1.86×10^{-08}	-1.56×10^{-08}	-1.60×10^{-08}
$^{208}_{82}$Pb [a]	5.501	0.061	0.000	-1.35×10^{-08}	-1.10×10^{-08}	-1.13×10^{-08}
$^{234}_{92}$U [b]	5.829	0.256	0.080	-1.12×10^{-06}	-0.90×10^{-06}	-0.91×10^{-06}
$^{238}_{92}$U [b]	5.851	0.280	0.070	-1.28×10^{-06}	-1.02×10^{-06}	-1.04×10^{-06}
$^{244}_{94}$Pu [a]	5.895	0.284	0.062	-1.57×10^{-06}	-1.25×10^{-06}	-1.27×10^{-06}
$^{248}_{96}$Cm [a]	5.869	0.294	0.040	-1.90×10^{-06}	-1.51×10^{-06}	-1.54×10^{-06}

[a] parameters obtained as described in the text.
[b] parameters of deformed Fermi distribution taken from [144].
[c] value from Ref. [221]

3.5 Conclusion

At first, in this chapter, the following known results are summarized:

- For spinless nuclei, the angular dependence of the interaction energy averaged out and the bound electron is exposed to an averaged, spherically symmetric nuclear potential.

- For these spherically symmetric potentials, the g factor can be calculated with radial integrals or derivatives of the binding energy with respect to the electron mass, using solutions of the Dirac equation.

- Deformed charge distributions cause a nuclear deformation effect on the g factor, which can be calculated perturbatively with the effective-radius method according to Ref. [144].

Thereafter, the following new results were presented in this thesis:

- The nuclear deformation correction is calculated without using the perturbative effective-radius method. Instead, the averaged potential is calculated numerically starting from a given deformed charge distribution. Then, finite-basis-set methods are used to solve the Dirac equation numerically in this potential and the integrals and energy derivatives for the bound electron g factor are also performed numerically. Thereby, nuclear deformation effects on the bound electron g factor are obtained non-perturbatively.

- Results for a wide range of nuclei were presented using the non-perturbative method. It was shown that the results for the deformation effects of the previously used perturbative effective-radius method differ from the non-perturbative results on the 20%-level.

- For uranium-238, it was shown that the uncertainty of the finite nuclear size effect due to model dependence can be reduced significantly with the consideration of deformation effects.

Chapter 4

Bound muon g factor in $^{4}_{2}$He

Another application of the calculations described in this thesis is connected to the bound muon g factor in muonic $^{4}_{2}$He, following the work presented in [2] by the first author B. Sikora. Although the helium nucleus has a low charge number, finite nuclear size corrections have to be considered for precise theoretical predictions. In this thesis, the finite nuclear size, electronic Uehling, muonic Uehling, electronic second/higher order Uehling and electronic Källén-Sabry corrections to the bound muon g factor in muonic $^{4}_{2}$He were calculated. All effects take an extended nuclear charge distribution into account, and the uncertainty due to the value of the RMS charge radius and model dependence of the nuclear charge distribution is taken into account. Other effects, like nuclear polarization, further one- and two-loop QED, recoil, hadronic and weak corrections have been calculated by the other authors in [2]. Thereby, a theoretical prediction of the bound-muon g factor in $^{4}_{2}$He on the 10^{-9} level is obtained.

The calculations are preformed analogously to Chapter 3, but now with a bound muon instead of a bound electron. That is, the Dirac equation

$$[\boldsymbol{\alpha} \cdot \mathbf{p} + \beta m_\mu + V_i(r)] \ket{n\kappa m} = E_{n\kappa} \ket{n\kappa m}$$

is solved for spherically symmetric potentials $V_i(r)$, which are described below. Then, according to Eq. (3.5), the g factors g_i, including the corrections due to V_i can be obtained by radial integration of the solutions as

$$g_i = \frac{2m_\mu \kappa}{j(j+1)} \int_0^\infty \mathrm{d}r\, r^3 f_{n\kappa}(r) g_{n\kappa}(r).$$

The finite nuclear size, the electric-loop (Fig. 1.4 with an external muon and internal electron) and muonic-loop Uehling (Fig. 1.4 with an external muon and internal muon) correction as well as the Källen-Sabry correction (Fig. 1.5 with an external muon and internal electron) to the bound muon g factor are considered by including the corresponding potentials directly in the Dirac equation. A two-parameter Fermi charge distribution

$$\rho(r) = \frac{N}{1 + \exp\left[(r-c)/a\right]}$$

is used, such that the RMS value of $1.6755\,\mathrm{fm}$ agrees with the literature value from Ref. [178] The uncertainty of this charge distribution is estimated by using the uncertainty in the RMS value and the model dependence is estimated conventionally by varying the parameters a between $0.05\,\mathrm{fm}$ and $0.3\,\mathrm{fm}$. The considered potentials are the point-

like Coulomb potential $V_C(r)$ from Eq. (1.21), finite size electric potential $V(r)$ from Eq. (1.2), and Uehling potentials $V_{\text{Uehl}}^{(m_e)}(r)$, $V_{\text{Uehl}}^{(m_\mu)}(r)$ from Eq. (1.14) for the electric- and muonic-loop Uehling potential, respectively. Furthermore, the Källen-Sabry potential with electronic loops $V_{\text{KS}}^{(m_e)}(r)$ from Eq. (1.15) is taken into account. The g-factor corrections are obtained as follows:

i	potential	g_i factor	$\delta g_i/10^{-8}$ correction
0	$V_0(r) = V_C(r)$	1.999 857 988 825 369	–
1	$V_1(r) = V(r)$	1.999 858 083 413 814	$+\ 9.46(4)$
2	$V_2(r) = V(r) + V_{\text{Uehl}}^{(m_e)}(r)$	1.999 857 602 755 145	$-48.0659(4)$
3	$V_3(r) = V(r) + V_{\text{Uehl}}^{(m_e)}(r) + V_{\text{Uehl}}^{(m_\mu)}(r)$	1.999 857 602 647 854	$-\ 0.01073(2)$
4	$V_4(r) = V(r) + V_{\text{Uehl}}^{(m_e)}(r) + V_{\text{KS}}(r)$	1.999 857 599 294 144	$-\ 0.346(1)$

The corrections δg_i are defined as:

correction	definition	effect
δg_1	$g_1 - g_0$	finite nuclear size correction
δg_2	$g_2 - g_1$	electronic-loop Ueling correction
δg_3	$g_3 - g_2$	muonic-loop Ueling correction
δg_4	$g_4 - g_2$	Källen-Sabry correction

Thus, mixed Källen-Sabry and muonic-loop Uehling terms are not considered, but since the individual contributions are already small, the combined contribution is expected to be even smaller and not visible on the 10^{-10}-level at all. Finally, the electronic-loop Uehling correction can be written as $\delta g_1 = 47.9600 \times 10^{-8} + 0.1059 \times 10^{-8}$, where the first terms corresponds to the first order Uehling correction, which is the expectation value of the Uehling potential, corresponding to diagram Fig. 1.4 (a). The second term corresponds to the second and higher-order Uehling corrections, mainly corresponding to diagram Fig. 1.4 (b), but also higher-order diagrams like Fig. 1.4 (c). Higher order iterations do not contribute on the 10^{-10} level. All calculated contributions to the theoretical prediction of the bound muon g factor in $^4_2$He are presented in Table 4.1, where the contributions calculated in this thesis are highlighted in red. There are still uncalculated two-loop light-by-light-scattering diagrams, and the corresponding uncertainty is estimated as 5×10^{-9} [2].

In conclusion, it was demonstrated that the bound-muon g factor in $^4_2$He can be calculated on the 10^{-9} level. A measurement of this g factor as g_{exp} with a similar experimental accuracy could give access to an independent determination of the muon mass, one order of magnitude more accurate than the current value. For this, the dependency of the experimental value g_{exp} and the theoretical value g_{theory} on the muon mass has to be solved for an expression of the muon mass in dependency of the experimental and theoretical value as

$$g_{\text{theory}}(m_\mu) \overset{!}{=} g_{\text{exp}}(m_\mu)$$
$$\rightarrow m_\mu = m_\mu(g_{\text{theory}}, g_{\text{exp}}).$$

Alternatively, an independent determination of the muon magnetic moment anomaly of the free muon $g_{\text{free}} - 2$ may be possible by separating the contributions to the free g factor and the binding corrections as $g_{\text{theory}} = g_{\text{free}} + g_{\text{binding}} \overset{!}{=} g_{\text{exp}}$ [2]. However, it is important to keep in mind that the life time of the muon is around one microsecond, which is too short-lived for measuring the g factor of muonic atoms in the same way as for electronic atoms, for example in Refs. [108, 110] and thus a measurement of the bound-muon g factor on the 10^{-9} level represents a major experimental challenge.

Table 4.1: Various contributions to the g factor of $\mu^4\text{He}^+$. eVP/μVP stands for VP due to virtual $e^-e^+/\mu^-\mu^+$ pairs. The estimated uncertainty of the nuclear size effect stems from the error bar of the nuclear RMS radius and the uncertainty of the nuclear charge distribution model. If not indicated, the uncertainty is negligible. In the last row, the uncertainties due to the calculated and uncalculated (two-loop light-by-light) terms are given separately. The table and caption is taken from Ref. [2] and the contributions highlighted in red were calculated in the framework of this thesis.

Effect	Term	Numerical value	Ref.
Dirac value		1.999 857 988 8	[91, 119]
Finite nuclear size		0.000 000 094 6(4)	[178]
Nuclear pol.		0.000 000 000 0(10)	
One-loop SE	$(Z\alpha)^0$	0.002 322 819 5	[47, 91]
	all-order binding	0.000 000 084 9(10)	
One-loop VP	eVP, Uehling	-0.000 000 479 6	
	eVP, magnetic loop	0.000 000 127 2(4)	
	μVP, Uehling	-0.000 000 000 1	
	hadronic VP, Uehling	-0.000 000 000 1(1)	
Two-loop QED	$(Z\alpha)^0$	0.000 008 264 4	[97, 99]
	SE-SE, $(Z\alpha)^2$— $(Z\alpha)^5$	-0.000 000 000 1	[123, 125, 222, 223]
	S(eVP)E, $(Z\alpha)^2$	0.000 000 000 4	[97, 99, 222, 223]
	Second-order Uehling	-0.000 000 001 1(4)	
	Källén-Sabry	-0.000 000 003 5	
	magnetic loop+Uehling	0.000 000 000 3	
	uncalculated LBL	0.000 000 000 0 (50)	
$\geq$ Three-loop QED	$(Z\alpha)^0$	0.000 000 610 6	[91, 100, 102, 224]
Nuclear recoil	$\left(\frac{m_\mu}{M}\right)^1$, all orders in $Z\alpha$	0.000 006 038 2	[143]
	$\left(\frac{m_\mu}{M}\right)^{2+}$, $(Z\alpha)^2$	-0.000 000 488 7	[225]
	radiative recoil	-0.000 000 004 7	[226]
Weak interaction	$(Z\alpha)^0$	0.000 000 003 1	[91, 227]
Hadronic	$(Z\alpha)^0$	0.000 000 139 3(12)	[91, 228–230]
Sum of terms calculated		2.002 195 193 4(20)$_{\text{calc}}$(50)$_{\text{uncalc}}$	

Summary & Outlook

In the present thesis, nuclear structure effects caused by extended and deformed nuclear charge distributions and corrections from quantum electrodynamics in the spectra of heavy ions and muonic atoms are investigated. Here, the focus is on two topics, namely, on the analysis of the level structure and spectra of muonic atoms, and on improved calculations of the nuclear shape effect on the bound-electron g factor for spinless nuclei beyond the previously used perturbative evaluation.

Chapter 2 deals with high-precision calculations of the spectra of muonic atoms. As a first step, the implementation of the most important effects, namely, finite nuclear size, vacuum polarization, recoil, and electron screening on the fine and hyperfine structure is discussed in Sec. 2.1. This includes calculations of the dynamical hyperfine structure, which means that the hyperfine structure is considered beyond the first order in the quadrupole interaction for the most important states. A finite-basis-set method based on B-splines has been used, which is a well established and efficient method in atomic physics, but had not been used in the context of muonic atoms before. Thereby, a practical, numerical representation of the complete spectrum of muon wave functions is obtained.

In Sec. 2.2, enhanced theoretical approaches for calculations connected to the electric quadrupole interaction between muon and nucleus are presented. Firstly, this includes a numerical evaluation of the leading-order vacuum polarization correction (Uehling potential) to the quadrupole matrix elements for an arbitrary, deformed nuclear charge distribution. In contrast to previous works, this is done without any approximations on the shape of the charge distribution or the distance between nucleus and muon. For this, a multipole expansion of the Uehling potential is performed. In this thesis, the corresponding expansion coefficients are given in a form suitable for numerical evaluation, as well as analytically in terms of special functions. Secondly, the energy correction due to residual second-order quadrupole interaction is calculated by means of the finite basis set of muon wave functions. Both contributions are shown to be potentially important for upcoming experiments.

In Sec. 2.3, the theoretical calculations of this thesis are compared to state-of-the-art experiments in muonic atom spectroscopy, performed recently at the Paul Scherrer Institute (Switzerland) by the MuX collaboration. Theoretical spectra have been fitted to experimental ones by adjusting the parameters of the nuclear model. In this way, the nuclear quadrupole moment of $^{185}_{75}$Re and $^{187}_{75}$Re were extracted from the observed $n=5 \rightarrow n=4$ x-rays. Obtaining values for the nuclear quadrupole moments is of great importance, because they can be tested against predictions from theoretical nuclear models. Also, the spectra of low-lying muonic x-rays in $^{185}_{75}$Re have been explained by the calculations in this thesis.

Chapter 3 covers non-perturbative calculations of nuclear shape effects on the bound-electron g factor. Here, the previously used perturbative method is introduced, which is called the effective-radius method, because the homogeneously charged sphere model of a given radius with approximately the same energy correction as the deformed nuclear charge distribution is used. Then, the non-perturbative, numerical method used in this thesis is explained, wherein the nuclear potential, the solution of the Dirac equation and the corresponding g factor are calculated in an all-numeric manner, starting with the deformed nuclear charge distribution. Calculations for a wide range of nuclei across the nuclear chart reveal that the perturbative evaluation overestimated the nuclear shape effect on the 20% level. The difference between the fully numerical and perturbative, effective-radius method is investigated. It is shown that the formulas for a perturbative calculation of the effective radius and the corresponding energy correction of the homogeneously charged sphere are mainly responsible for the disagreement, but also the incompleteness of the effective radius method itself contributes.

Furthermore, the connection between nuclear finite size and deformation effects is discussed and it is demonstrated how the consideration of deformed nuclei can reduce the model uncertainty in the theoretical prediction of finite-nuclear-size effects on the bound-electron g factor. The previous, conservative estimation of this uncertainty is the difference in the g factors due to a homogeneously charged sphere and a Fermi-type nuclear charge distribution. If parameters of the deformed nuclear charge distribution are available, the finite-nuclear-size and shape g-factor corrections can be calculated with their help. In this way, the remaining model uncertainty is reduced due to the more realistic nuclear model, which is demonstrated with calculations for hydrogen-like uranium.

Finally, in Chapter 4, finite nuclear size and several vacuum polarization corrections to the bound-muon g factor in muonic helium are presented. In combination with other calculations, this enabled a theoretical prediction of the g factor on the 10^{-9} level. It has been shown that not only the finite nuclear size and first-order Uehling correction are important on this level of accuracy, but also the two-loop Uehling and Källén-Sabry corrections, evaluated in this thesis. It was proposed that an independent and more accurate determination of the muon mass is possible through a combination of our results with future measurements of a similiar accuracy.

The ongoing experimental campaign on spectroscopy of heavy muonic atoms by the MuX collaboration will provide further possibilities to extract information on atomic nuclei from muonic x-rays, where the methods and codes from this thesis can be used. Due to progress in the experiments, it will be possible to analyze muonic x-rays also for radioactive nuclei, which will include the measurement of muonic x-rays up to the heaviest elements like $^{248}_{96}$Cm. The analysis of low-lying transitions is particularly interesting, since they contain the most information on the nuclear structure, such as the RMS radius of the electric charge distribution.

Currently, the limiting factor for theoretical predictions of low-lying transitions is the nuclear polarization correction. This is a second-order correction to the-bound state energies due to virtual excitation of the atomic nucleus in a muonic atom. Therefore,

many excited states of the nucleus contribute and as a consequence, an advanced nuclear model or a complete set of experimental data has to be used for a description of the nuclear polarization correction. The calculation of the residual second-order quadrupole interaction, as performed in this thesis, already demonstrated how the muonic part in second-order corrections can be evaluated with finite-basis-set methods. It would be highly desirable to combine the muonic calculations of this thesis with up-to-date nuclear structure theory or experimental data for a precise evaluation of the nuclear polarization correction in heavy muonic atoms. However, *ab initio* calculations for heavy nuclei pose a great challenge for nuclear structure theory.

Thinking further ahead, it would be insightful to cross-check the consistency of nuclear effects in muonic and electronic atoms in the high-Z regime. For example, muonic atom spectroscopy with $^{248}_{96}$Cm can be expected in the near future and the shape of the nuclear charge distribution can be potentially extracted from the corresponding muonic x-rays. Although this is a radioactive isotope, it has a halflife of several hundreds of thousands of years, thus also Penning trap experiments on the bound-electron g factor in $^{248}_{96}$Cm might be feasible. Then, the parameters of the nuclear charge distribution obtained from muonic x-rays can be used to calculate the finite nuclear size and nuclear shape effects for the bound-electron g factor. Provided that all other contributions, such as two-loop QED corrections, are under control, a comparison with the measured g factor can test the consistency of nuclear effects in electronic and muonic atoms. Furthermore, a better understanding of nuclear structure effects and a higher accuracy of nuclear parameters can lead to more stringent tests of QED, for example via g-factor measurements, and to improved determination of fundamental constants.
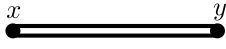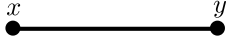
Chapter A

Appendix

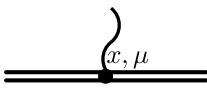## A.1 Conventions and notation

Variables

For the relativistic notation in Chapter 1, the symbols x, y, z, z_1, z_2, and p are used for four vectors corresponding to $x^\mu = (x^0, \mathbf{x}) = (x^0, x^1, x^2, x^3)$, where bold symbols stand for the three-component spacial vectors. The scalar product is $x_\mu y^\mu = x^0 y^0 - \mathbf{x} \cdot \mathbf{y}$, corresponding to the metric $g^{\mu\nu} = \text{diag}(1, -1, -1, -1)$.

In all other chapters, three dimensional vectors in spherical coordinates are written as bold symbols $\mathbf{r} = (r, \vartheta, \varphi)$, where φ is the polar angle and ϑ is the azimuthal angle. The volume element is as usual $\mathrm{d}^3 \mathbf{r} = \mathrm{d}r \mathrm{d}\varphi \mathrm{d}\vartheta\, r^2 \sin\vartheta$.

Feynman rules

In Chapter 1, the following Feynman rules in position space are needed, where the notation follows [155]. If external lines are involved, the corresponding solutions of the Dirac equation have to be used.

fermion propagator (ext. field): $S_A(x, y)$ from Eq. (1.8)

fermion propagator (free): $S_F(x - y)$ from Eq. (1.4)

photon propagator: (in Feynman gauge) $g_{\mu\nu} \dfrac{1}{4\pi^2} \dfrac{1}{(x - y)^2 - i\epsilon}$

vertex: $-ie\gamma^\mu \int \mathrm{d}^4 x$

Dirac matrices

The following representation of the Dirac matrices is chosen, following [42]:
β and γ matrices:

$$\beta = \gamma^0 = \begin{pmatrix} \mathbf{1} & \mathbf{0} \\ \mathbf{0} & -\mathbf{1} \end{pmatrix}; \qquad \gamma^i = \begin{pmatrix} \mathbf{0} & \boldsymbol{\sigma}^i \\ -\boldsymbol{\sigma}^i & \mathbf{0} \end{pmatrix}$$

with

$$\mathbf{0} = \begin{pmatrix} 0 & 0 \\ 0 & 0 \end{pmatrix}; \quad \mathbf{1} = \begin{pmatrix} 1 & 0 \\ 0 & 1 \end{pmatrix}; \quad \boldsymbol{\sigma}^1 = \begin{pmatrix} 0 & 1 \\ 1 & 0 \end{pmatrix}; \quad \boldsymbol{\sigma}^2 = \begin{pmatrix} 0 & -i \\ i & 0 \end{pmatrix}; \quad \boldsymbol{\sigma}^3 = \begin{pmatrix} 1 & 0 \\ 0 & -1 \end{pmatrix};$$

α matrices:

$$\boldsymbol{\alpha}^i = \gamma^0 \gamma^i = \begin{pmatrix} \mathbf{0} & \boldsymbol{\sigma}_i \\ \boldsymbol{\sigma}_i & \mathbf{0} \end{pmatrix}; \quad \text{with } i \in \{1, 2, 3\}.$$

A.2 Special functions

Gamma function

The Gamma funciton is defined as [193, Eq. 5.2.1]

$$\Gamma(z) = \int_0^\infty e^{-t} t^{z-1} \mathrm{d}t, \tag{A.1}$$

where the real part of the complex number z has to be strictly greater than zero (otherwise via analytic continuation).

Meijer G-function

The Meijer G-function is a general special function, which includes many other functions as special cases. It is defined as

$$G_{p,q}^{m,n}\left(z \left| \begin{matrix} a_1, ..., a_p \\ b_1, ..., b_q \end{matrix} \right.\right) = \frac{1}{2\pi \mathrm{i}} \int_L \left(\frac{\prod_{\ell=1}^m \Gamma(b_\ell - s) \prod_{\ell=1}^n \Gamma(1 - a_\ell + s)}{\left(\prod_{\ell=m}^{q-1} \Gamma(1 - b_{\ell+1} + s) \prod_{\ell=n}^{p-1} \Gamma(a_{\ell+1} - s)\right)} \right) z^s \mathrm{d}s, \tag{A.2}$$

where the integration contour L is a suitable path around the poles of $\Gamma(b_l - l)$ and $\Gamma(1 - a_l + s)$ [193, Eq. 16.17.1], and $\Gamma(z)$ is defined in Eq. (A.1). m, n, p, q are integers with $0 \leq m \leq q$ and $0 \leq n \leq p$, and $z, a_1, ..., a_p, b_1, ..., b_q$ are complex numbers where none of the differences $a_i - b_j$ must be positive integers for $0 \leq i \leq n$, $0 \leq j \leq m$.

Arbitrary precision implementations exist in several libraries and computer algebra systems, for example in Refs. [200, 201].

Hypergeometric function

The hypergeometric function $F(a, b, c, z)$ (or sometimes $_2F_1(a, b, c, z)$) is a special case of the Meijer G-function from Eq. (A.2) and can be obtained by

$$F(a, b, c, z) = \frac{\Gamma(c)}{\Gamma(a)\Gamma(b)} G_{2,2}^{1,2}\left(-z \left| \begin{matrix} 1 - a, 1 - b \\ 0, c \end{matrix} \right.\right)$$

It can also be written in terms of Gamma functions as [193, Eq. 15.2.1]

$$F(a, b, c, z) = \frac{\Gamma(c)}{\Gamma(a)\Gamma(b)} \sum_{s=0}^\infty \frac{\Gamma(a+s)\Gamma(b+s)}{\Gamma(c+s)s!} z^s \tag{A.3}$$

for $|z| < 1$ (otherwise via analytic continuation), and c must not be a negative integer or zero.

Wigner D-function

The Wigner D-function is defined via the hypergeometric function from Eq. (A.3) as [168]

$$D^l_{m_1 m_2}(\alpha, \beta, \gamma) = e^{-i(m_1\alpha + m_2\gamma)} d^l_{m_1 m_2}(\beta), \tag{A.4}$$

$$
\begin{aligned}
d^l_{m_1 m_2}(\beta) \quad &= \frac{\xi_{m_1 m_2}}{\mu!} \left(\frac{(s + \mu + \nu)!(s + \mu)!}{s!(s + \nu)!} \right)^{1/2} \quad (\sin \beta/2)^{\mu} (\cos \beta/2)^{\nu} \\
&\times F(-s, s + \mu + \nu + 1, \mu + 1, \sin^2 \beta/2),
\end{aligned}
$$

where $\mu = |m_1 - m_2|$, $\nu = |m_1 + m_2|$, $s = l - (\mu + \nu)/2$ and

$$\xi_{m_1 m_2} = \begin{cases} 1; m_2 \leq m_1 \\ (-1)^{m_2 - m_1}; m_2 < m_1, \end{cases}$$

and $F(a, b, c, x)$ are the hypergeometric functions from Eq. (A.3).

Spherical harmonics

The spherical harmonics $Y_{lm}(\vartheta, \varphi)$ are special cases of the Wigner D-functions [168] from Eq. (A.4):

$$Y_{lm}(\vartheta, \varphi) = \sqrt{\frac{2l + 1}{4\pi}} D^{l*}_{m0}(\varphi, \vartheta, 0) \tag{A.7}$$

The normalized spherical harmonics $C_{lm}(\vartheta, \varphi)$ are used frequently, which are connected to the spherical harmonics as

$$C_{lm}(\vartheta, \varphi) = \sqrt{\frac{4\pi}{2l + 1}} Y_{lm}(\vartheta, \varphi).$$

The set of all spherical harmonics $Y_{lm}(\vartheta, \varphi)$ with positive integer l and $-l \leq m \leq l$ is a complete orthonormal set [168] in the space of functions depending on $(\vartheta, \varphi) \in [0, \pi] \otimes [0, 2\pi]$. Thus, an arbitrary function $f(\vartheta, \varphi)$ can be written as

$$f(\vartheta, \varphi) = \sum_{l=0}^{\infty} \sum_{m=-l}^{l} a_{lm} Y_{lm}(\vartheta, \varphi),$$

with the expansion coefficients obtained by

$$a_{lm} = \int_0^{2\pi} d\varphi \int_0^{\pi} d\vartheta \sin \vartheta Y^*_{lm}(\vartheta, \varphi) f(\vartheta, \varphi).$$

Legendre polynomials

The Legendre polynomials $P_l(\cos\vartheta)$ can be expressed in terms of the spherical harmonics from Eq. (A.7) as

$$P_l(\cos\vartheta) = \sqrt{\frac{4\pi}{2l+1}} Y_{l0}(\vartheta, 0).$$

For two vectors $\mathbf{r}_i = (r_i, \vartheta_i, \varphi_i)$ with $i = 1, 2$, let $y = \cos\sphericalangle(\mathbf{r}_1, \mathbf{r}_2)$ be the cosine of the angle between the two vectors. Then, the following addition theorem [168] for Legendre polynomials and spherical harmonics holds:

$$P_l(y) = \frac{4\pi}{2l+1} \sum_{m=-l}^{l} Y_{lm}^*(\vartheta_1, \varphi_1) Y_{lm}(\vartheta_2, \varphi_2). \tag{A.8}$$

A.3 Angular momentum theory

Following the notation from [168], important results from the theory of rotations and angular momenta are summarized in this appendix.

Rotation of coordinate systems

The passive point of view for rotations is used in this thesis, where vectors are invariant objects and the coordinate axes are rotated. Two systems, the laboratory system with unprimed coordinates and the body-fixed system with primed coordinates are considered. The position of the axes of the body-fixed system is described by the Euler angles $\Omega = (\phi, \theta, \psi)$ in terms of the following three successive rotations of the axes of the laboratory system:

1. Angle ψ about z axis

2. Angle θ about (original) y axis

3. Angle ϕ about (original) z axis

Let $\mathbf{r}$ be a vector with coordinates (r, ϑ, φ) in the laboratory frame and $(r', \vartheta', \varphi')$ in the body fixed frame. Then, the primed angles are a function of the unprimed angles and the three Euler angles and the corresponding relations relations between the coordinates are

$$
\begin{aligned}
r &= r', \\
\cos\vartheta' &= \cos\vartheta \, \cos\theta + \sin\vartheta \sin\theta \cos(\varphi - \phi), \\
\cot(\varphi' + \psi) &= \cot(\varphi - \phi) \cos(\theta) - \frac{\cot\vartheta \sin\theta}{\sin(\varphi - \phi)}.
\end{aligned}
$$

This gives the following relation for spherical harmonics as a function of (ϑ', φ') and the corresponding (ϑ, φ):

$$Y_{lm}(\vartheta', \varphi') = \sum_{m_2=-l}^{l} Y_{lm_2}(\vartheta, \varphi) D_{m_2\,m}^{l}(\phi, \theta, \phi), \qquad (A.9)$$

where $D_{m_1\,m_2}^{l}(\alpha, \beta, \gamma)$ are the Wigner D-functions defined in Eq. (A.4) and $Y_{lm}(\vartheta, \varphi)$ are defined in Eq. (A.4).

Irreducible tensor operators

An irreducible tensor operator [168] of rank l is a $(2l+1)$-component operator $t_{lm}(\mathbf{x})$, depending on the variables $\mathbf{x}$, where the components transform like the spherical harmonics in Eq. (A.9) under a rotation of the coordinate system described by the Euler angles (ϕ, θ, ψ) as

$$t_{lm}(\mathbf{x}') = \sum_{m_2=l}^{l} t_{lm_2}(\mathbf{x}) D_{m_2\,m}^{l}(\phi, \theta, \psi)$$

where the new coordinates $\mathbf{x}'$ are a function of the old $\mathbf{x}$ and the Euler angles (ϕ, θ, ψ). The expectation values of irreducible tensor in rotational states $|l_1 m_1\rangle$, and $|l_2 m_2\rangle$ of defined angular momenta l_1, l_2 with projections m_1, m_2 on the z axis, respectively, can be written as [168]

$$\langle l_1 m_1 | t_{lm} | l_2 m_2 \rangle = (-1)^{l_1 - m_1} \begin{pmatrix} l_1 & l & l_2 \\ -m_1 & m & m_2 \end{pmatrix} \langle l_1 || t_l || l_2 \rangle, \qquad (A.10)$$

where the double-bar matrix element on the right hand side is called the *reduced matrix element*, and the Wigner-$3j$-symbol is defined in [168, Section 8.]. This is also known as the Wigner-Eckardt-theorem, and thereby, the dependence of the matrix element on m_1, m_2, and m can be explicitly written in terms of the Wigner-$3j$-symbol. In practice, this means that matrix elements of irreducible operators only have to be calculated once for a convenient choice of m_1, m_2, and m, and then can be translated to other values of the projections.

Let two systems, system 1 and 2, with rotational states $|j_1 m_1\rangle$ and $|j_2 m_2\rangle$ be coupled to states with defined total angular momentum j as

$$|jm\,j_1 j_2\rangle = \sum_{m_1, m_2} \mathrm{C}_{j_1 m_1\,j_2 m_2}^{jm} |j_1 m_1\rangle \otimes |j_1 m_1\rangle, \qquad (A.11)$$

and analogously for j', m', j_1', j_2'. Here, $\mathrm{C}_{j_1 m_1\,j_2 m_2}^{jm}$ are the Clebsch-Gordan-coefficients, as defined in [168, Section 9.], and let $t_{lm_1}^{(1)}$, $t_{lm_2}^{(2)}$ be two irreducible tensor operators acting on system 1 and system 2, respectively. Then, the scalar product of these to operators is defined as

$$t_l^{(1)} \cdot t_l^{(2)} = \sum_{m} (-1)^{-m}\, t_{lm}^{(1)} \cdot t_{l-m}^{(2)}, \qquad (A.12)$$

and matrix elements thereof can be expressed in terms of the reduced matrix elements as [168]

$$\left\langle j'm' \, j'_1 j'_2 \middle| t_l^{(1)} \cdot t_l^{(2)} \middle| jm \, j_1 j_2 \right\rangle = \delta_{j'j} \delta_{m'm} (-1)^{j+j_1+j'_2} \begin{Bmatrix} j'_1 & j_1 & l \\ j_2 & j'_2 & j \end{Bmatrix} \left\langle j'_1 \middle| \middle| t_l^{(1)} \middle| \middle| j_1 \right\rangle \left\langle j'_2 \middle| \middle| t_l^{(2)} \middle| \middle| j_2 \right\rangle .$$
(A.13)

Another frequently used application of the coupled representation is calculation of the matrix element of one operator $t_{lm_1}^{(1)}$ acting only on the coordinates of system 1, when the states are given in the coupled representation from Eq. (A.11). In this case, the matrix element reads as [168]

$$\left\langle j'm' \, j'_1 j'_2 \middle| t_{lm_l}^{(1)} \middle| jm \, j_1 j_2 \right\rangle = \delta_{j'_2 j_2} (-1)^{j+j'_1+j_2-l} \sqrt{2j+1} \, \mathrm{C}_{jm \, lm_l}^{j'm'} \begin{Bmatrix} j_1 & j_2 & j \\ j' & l & j'_1 \end{Bmatrix} \left\langle j'_1 \middle| \middle| t_l^{(1)} \middle| \middle| j_1 \right\rangle .$$
(A.14)

A.4 Symmetric rigid rotor model

In this thesis, a nuclear model is needed which can account for the two following aspects: Firstly, for the description of hyperfine interactions, it needs to describe the angular momentum of the nucleus in its ground state rotational band, both for nuclei with vanishing and integer or half-integer non-zero ground state angular momentum. Secondly, finite nuclear-size effects need to be included. Therefore, the nuclear model needs to include the charge distribution and correspondingly, the distribution of higher-order multipoles, like the electric quadrupole and magnetic dipole. The simplest collective nuclear model which complies with these requirements is the symmetric rigid rotor model. Here, the nucleus is described by rigid charge distribution in a body fixed nuclear frame, i.e. the nucleus does not change the shape of the charge distribution, but it can rotate, which is described by a rotation of the nuclear body-fixed frame in the laboratory frame. The following derivations follow [168, 231, 232], where the notation and conventions follow [168]. Generally, rotations of coordinate system are described by the three Euler angles $\Omega = (\phi, \theta, \psi)$, where ϕ, θ are the polar and azimuthal angles, respectively, describing the position of the body-fixed z' axis in the laboratory frame. ψ is the polar angle describing the orientation of the x' and y' axes with respect to the z' axis. Correspondingly, these are the degrees of freedom for the rigid rotor model. Motivated by the classical kinetic energy of an axially symmetric rotating rigid body, the total energy can be expressed in terms of the moments of inertia $\Theta_1 = \Theta_2$, Θ_3 and corresponding angular velocities ω_i of the rigid body as

$$E_{\mathrm{rot}} = \frac{1}{2} \Theta_1 \left(\omega_1^2 + \omega_2^2 \right) + \frac{1}{2} \Theta_3 \omega_3^2$$

The angular velocities can be expressed in terms of the Euler angles as

$$\omega_1 = \dot{\theta}\sin\psi - \dot{\phi}\sin\theta\cos\psi,$$
$$\omega_2 = \dot{\theta}\cos\psi + \dot{\phi}\sin\theta\sin\psi,$$
$$\omega_3 = \dot{\phi}\cos\theta + \dot{\psi},$$

and thereby, the Hamiltonian is obtained by introducing the generalized momenta $p_x = \partial E/\partial x$ for $x \in \{\phi, \theta, \psi\}$ as

$$\mathrm{H}(\theta, p_\phi, p_\theta, p_\psi) = \frac{1}{2\Theta_1\Theta_3}\left(\Theta_1 p_\psi^2 + \Theta_3 p_\theta^2 + \Theta_3\left(\frac{p_\psi}{\tan\theta} - \frac{p_\phi}{\sin\theta}\right)^2\right) - \frac{(\theta p_\theta - p_\theta\theta)\cot\theta}{2\Theta_1}p_\theta.$$

Since non-Cartesian coordinates are used, the last term vanishes for the classical theory but is needed for the correct quantum theory with naive canonical quantization due to operator ordering [233]. The corresponding Schrödinger equation for the quantized symmetric rigid rotor can now be obtained by substituting $p_x \to -i\partial_x$. The eigenenergies E and corresponding eigenfunctions can be found by solving the equation [231]

$$\left\{-\frac{1}{2\Theta_1}\left[\partial_\theta^2 + \cot\theta\partial_\theta + \left(\frac{\Theta_1}{\Theta_3} + \cot^2\theta\right)\partial_\psi^2 + \frac{1}{\sin^2\theta}\partial_\phi - \frac{2\cos\theta}{\sin^2\theta}\partial_\phi\partial_\psi\right] - E\right\}D(\phi, \theta, \psi) = 0.$$

The eigenfunctions turn out to be the complex conjugate of the Wigner D-functions $D_{MK}^{I*}(\phi, \theta, \psi)$ and the corresponding eigenenergies are [234]

$$E_{IK} = \frac{I(I+1)}{2\Theta_1} + \left(\frac{1}{2\Theta_3} - \frac{1}{2\Theta_1}\right)K^2. \tag{A.15}$$

Here, K is angular momentum in the body-fixed nuclear frame, corresponding to the ground state angular momentum, if the nucleus is in its ground-state rotational band, and $I(I+1)$ is the squared total angular momentum with the z component in the laboratory frame M. With the correct normalization, the wave functions of the symmetric top read as

$$\langle \phi\,\theta\,\psi | IMK \rangle = \sqrt{\frac{2I+1}{8\pi^2}}D_{MK}^{I*}(\phi, \theta, \psi), \tag{A.16}$$

where the Wigner D-functions are defined in Eq. (A.4). Instead of the energies E_{IK}, also the measured energies of the corresponding nuclear states [179] are used. Matrix elements of operators $O(\phi, \theta, \psi)$ depending on the Euler angles are calculated as

$$\langle I'M'K' | \hat{O} | IMK \rangle = \frac{\sqrt{(2I+1)(2I'+1)}}{8\pi^2}$$
$$\times \int_0^{2\pi}\mathrm{d}\phi\int_0^\pi\mathrm{d}\theta\,\sin\theta\int_0^{2\pi}\mathrm{d}\psi D_{M'\,K'}^{I'}(\phi, \theta, \psi)O(\phi, \theta, \psi)D_{M\,K}^{I*}(\phi, \theta, \psi)$$

For example, in atomic structure calculations, the matrix elements, reduced in M but not in K, of spherical harmonics $Y_{lm}(\theta, \phi)$ with rigid rotor states are needed:

$$\langle I_1 K || Y_l(\theta, \phi) || I_2 K \rangle = (-1)^{I_2+K} \sqrt{(2I_1 + 1)(2I_2 + 1)(2l + 1)/(4\pi)} \begin{pmatrix} I_1 & I_2 & l \\ -K & K & 0 \end{pmatrix}.$$

(A.17)

A.5 Fitting coefficients for $^{187}_{75}$Re

In this appendix, the fitting coefficients for the N_α x-rays ($n = 5 \rightarrow n = 4$) in muonic $^{187}_{75}$Re are given in analogy to Tables 2.9, 2.10, and 2.11 for $^{185}_{75}$Re in Section 2.3. The calculations are described in Section 2.3., as well.

Table A.1: Quadratic fits of the energies of the centroid transitions for $^{187}_{75}$Re. The formula for the energy difference in terms of a give quadrupole moment Q is given in Eq. (2.53). See Section 2.3. for details.

centroid	$F_i \rightarrow F_f$	ΔE_2^{if} [keV/barn^2]	ΔE_1^{if} [keV/barn]	ΔE_0^{if} [keV]
$5g_{9/2} \rightarrow 4f_{7/2}$	$7 \rightarrow 6$	0.0000	-0.1745	360.2146
$5g_{7/2} \rightarrow 4f_{5/2}$	$6 \rightarrow 5$	0.0039	-0.1600	364.6627
$5f_{7/2} \rightarrow 4d_{5/2}$	$6 \rightarrow 5$	-0.0017	-0.4390	364.4118
$5g_{7/2} \rightarrow 4f_{7/2}$	$6 \rightarrow 6$	-0.0004	-0.1777	358.2799
$5f_{5/2} \rightarrow 4d_{5/2}$	$5 \rightarrow 5$	-0.0040	-0.4476	361.1363

Table A.2: Quadratic fits of the transitions energies compared to the most intense (centroid) transition for the most intense transitions for the $5g_{9/2} \rightarrow 4f_{7/2}$, $5g_{7/2} \rightarrow 4f_{7/2}$, $5f_{7/2} \rightarrow 4d_{5/2}$, $5g_{7/2} \rightarrow 4f_{7/2}$, and $5f_{5/2} \rightarrow 4d_{5/2}$ groups in $^{187}_{75}$Re. The absolute transition energies of the centroid transitions are given in Table A.1. The formula for the transition energy in terms of a give quadrupole moment Q is given in Eq. (2.53). See Section 2.3. for details.

Group	$F_i \rightarrow F_f$	ΔE_2^{if} [eV/barn^2]	ΔE_1^{if} [eV/barn]	ΔE_0^{if} [eV]
$5g_{9/2} \rightarrow 4f_{7/2}$	$7 \rightarrow 6$	0.0000	0.0000	0.0000
	$6 \rightarrow 6$	0.1633	-111.7023	-5.6165
	$6 \rightarrow 5$	-3.9877	374.4897	8.3492
	$5 \rightarrow 6$	-0.3011	-129.1571	-10.0531
	$5 \rightarrow 5$	-4.4521	357.0349	3.9127
	$5 \rightarrow 4$	-0.1158	385.8705	20.0992
	$4 \rightarrow 5$	-4.2649	396.9053	0.9660
	$4 \rightarrow 4$	0.0715	425.7409	17.1525
	$4 \rightarrow 3$	-1.4490	210.4971	27.8759
	$3 \rightarrow 4$	0.3917	493.3849	15.1365
	$3 \rightarrow 3$	-1.1288	278.1411	25.8599
	$3 \rightarrow 2$	-2.4508	-23.3796	33.7365
	$2 \rightarrow 3$	-0.9929	349.6010	24.6058

(continued on next page)

Group	$F_i \rightarrow F_f$	ΔE_2^{if}[eV/barn^2]	ΔE_1^{if}[eV/barn]	ΔE_0^{if}[eV]
	(continuation from previous page)			
	$2 \rightarrow 2$	-2.3149	48.0803	32.4824
	$2 \rightarrow 1$	-1.4923	-218.4873	36.9694
$5g_{7/2} \rightarrow 4f_{5/2}$	$6 \rightarrow 5$	0.0000	0.0000	0.0000
	$5 \rightarrow 5$	0.1514	-115.4968	-7.3678
	$5 \rightarrow 4$	-4.0113	397.2890	15.3747
	$4 \rightarrow 5$	0.0406	-123.6257	-12.7721
	$4 \rightarrow 4$	-4.1222	389.1601	9.9704
	$4 \rightarrow 3$	-2.6948	339.5489	29.2849
	$3 \rightarrow 4$	-4.1606	440.2046	6.2784
	$3 \rightarrow 3$	-2.7332	390.5934	25.5929
	$3 \rightarrow 2$	-1.6163	86.2175	39.5999
	$2 \rightarrow 3$	-2.5289	462.5721	23.1333
	$2 \rightarrow 2$	-1.4120	158.1963	37.1402
	$2 \rightarrow 1$	-2.4360	-173.0982	46.9353
	$1 \rightarrow 2$	-1.0387	222.2765	35.6250
	$1 \rightarrow 1$	-2.0626	-109.0180	45.4200
	$1 \rightarrow 0$	-3.8653	-313.0469	50.3434
$5f_{7/2} \rightarrow 4d_{5/2}$	$6 \rightarrow 5$	0.0000	0.0000	0.0000
	$5 \rightarrow 5$	2.2385	-252.0299	-7.0099
	$5 \rightarrow 4$	-37.8953	1136.3946	-1.4308
	$4 \rightarrow 5$	-0.0604	-266.9037	-15.3986
	$4 \rightarrow 4$	-40.1942	1121.5208	-9.8195
	$4 \rightarrow 3$	-2.8349	939.6150	48.6785
	$3 \rightarrow 4$	-39.4097	1233.0822	-15.4146
	$3 \rightarrow 3$	-2.0505	1051.1763	43.0834
	$3 \rightarrow 2$	-21.3568	232.3250	69.8459
	$2 \rightarrow 3$	-1.3748	1207.4408	38.9351
	$2 \rightarrow 2$	-20.6812	388.5895	65.6976
	$2 \rightarrow 1$	-23.5209	-469.5398	68.7165
	$1 \rightarrow 2$	-21.1319	526.7186	63.3219
	$1 \rightarrow 1$	-23.9716	-331.4107	66.3408
	$1 \rightarrow 0$	1.4780	-868.0971	73.0309
$5g_{7/2} \rightarrow 4f_{7/2}$	$6 \rightarrow 6$	0.0000	0.0000	0.0000
	$6 \rightarrow 5$	-4.1510	486.1920	13.9657
	$5 \rightarrow 6$	0.1514	-115.4968	-7.3678
	$5 \rightarrow 5$	-3.9995	370.6953	6.5980
	$5 \rightarrow 4$	0.3368	399.5308	22.7845
	$4 \rightarrow 5$	-4.1104	362.5663	1.1937
	$4 \rightarrow 4$	0.2260	391.4019	17.3802
	$4 \rightarrow 3$	-1.2945	176.1582	28.1036
	$3 \rightarrow 4$	0.1876	442.4464	13.6881
	(continued on next page)			

Group	$F_i \to F_f$	$\Delta E_2^{if}[\text{eV/barn}^2]$	$\Delta E_1^{if}[\text{eV/barn}]$	$\Delta E_0^{if}[\text{eV}]$
	(continuation from previous page)			
	$3 \to 3$	-1.3329	227.2026	24.4115
	$3 \to 2$	-2.6549	-74.3181	32.2881
	$2 \to 3$	-1.1286	299.1814	21.9519
	$2 \to 2$	-2.4507	-2.3393	29.8285
	$2 \to 1$	-1.6280	-268.9069	34.3156
	$1 \to 2$	-2.0773	61.7409	28.3132
	$1 \to 1$	-1.2546	-204.8267	32.8003
$5f_{5/2} \to 4d_{5/2}$	$5 \to 5$	0.0000	0.0000	0.0000
	$5 \to 4$	-40.1338	1388.4245	5.5791
	$4 \to 5$	2.2377	-267.0185	-11.5610
	$4 \to 4$	-37.8961	1121.4060	-5.9819
	$4 \to 3$	-0.5368	939.5002	52.5161
	$3 \to 4$	-38.6498	1147.2215	-15.9242
	$3 \to 3$	-1.2905	965.3157	42.5738
	$3 \to 2$	-20.5969	146.4644	69.3362
	$2 \to 3$	-1.8966	1123.7702	35.3152
	$2 \to 2$	-21.2030	304.9189	62.0777
	$2 \to 1$	-24.0427	-553.2105	65.0966
	$1 \to 2$	-20.6838	477.4056	56.9660
	$1 \to 1$	-23.5235	-380.7237	59.9849
	$1 \to 0$	1.9261	-917.4101	66.6750
	$0 \to 1$	-22.5830	-274.4994	57.4088

Table A.3: Quadratic fits of the relative intensities for the most intense transitions each for the $5g_{9/2} \to 4f_{7/2}$, $5g_{7/2} \to 4f_{7/2}$, $5f_{7/2} \to 4d_{5/2}$, $5g_{7/2} \to 4f_{7/2}$, and $5f_{5/2} \to 4d_{5/2}$ groups in $^{187}_{75}$Re. The intensities are given relative to the most intense (cenroid) transition. The formula for the transition energy in terms of a give quadrupole moment Q is given in Eq. (2.54). See Section 2.3. for details.

Group	$F_i \to F_f$	$I_2^{if}[\%/\text{barn}^2]$	$I_1^{if}[\%/\text{barn}]$	$I_0^{if}[\%]$
$5g_{9/2} \to 4f_{7/2}$	$7 \to 6$	0.000	0.000	100.000
	$6 \to 6$	-0.011	-0.114	8.044
	$6 \to 5$	-0.007	0.379	78.607
	$5 \to 6$	0.000	-0.002	0.311
	$5 \to 5$	-0.012	0.034	12.377
	$5 \to 4$	0.000	0.214	60.644
	$4 \to 5$	-0.001	0.012	0.669
	$4 \to 4$	-0.001	0.108	13.528
	$4 \to 3$	-0.002	0.008	45.817
	$3 \to 4$	0.000	0.019	0.837
	$3 \to 3$	-0.001	0.103	11.901

(continued on next page)

Group	$F_i \to F_f$	$I_2^{if}[\%/\mathrm{barn}^2]$	$I_1^{if}[\%/\mathrm{barn}]$	$I_0^{if}[\%]$
	(continuation from previous page)			
	$3 \to 2$	-0.002	-0.101	33.943
	$2 \to 3$	0.000	0.013	0.619
	$2 \to 2$	-0.001	0.050	7.725
	$2 \to 1$	-0.001	-0.104	24.999
$5g_{7/2} \to 4f_{5/2}$	$6 \to 5$	0.000	0.000	100.000
	$5 \to 5$	0.022	0.219	12.060
	$5 \to 4$	0.035	0.366	72.585
	$4 \to 5$	0.003	0.024	0.730
	$4 \to 4$	0.008	0.090	18.100
	$4 \to 3$	0.020	0.401	50.419
	$3 \to 4$	0.001	0.009	1.642
	$3 \to 3$	0.012	-0.045	19.210
	$3 \to 2$	0.012	0.260	33.001
	$2 \to 3$	0.002	-0.022	2.192
	$2 \to 2$	0.009	-0.096	16.475
	$2 \to 1$	0.009	0.095	19.796
	$1 \to 2$	0.001	-0.027	1.829
	$1 \to 1$	0.004	-0.077	10.987
	$1 \to 0$	0.005	-0.008	10.261
$5f_{7/2} \to 4d_{5/2}$	$6 \to 5$	0.000	0.000	100.000
	$5 \to 5$	-0.041	-0.311	12.110
	$5 \to 4$	-0.099	1.186	72.335
	$4 \to 5$	0.000	-0.002	0.738
	$4 \to 4$	-0.101	0.323	18.062
	$4 \to 3$	-0.007	0.381	50.337
	$3 \to 4$	-0.015	0.084	1.642
	$3 \to 3$	-0.002	0.329	19.268
	$3 \to 2$	-0.020	-0.184	32.972
	$2 \to 3$	-0.001	0.096	2.206
	$2 \to 2$	-0.009	0.170	16.509
	$2 \to 1$	-0.019	-0.274	19.772
	$1 \to 2$	0.000	0.056	1.836
	$1 \to 1$	-0.010	0.009	10.996
	$1 \to 0$	0.000	-0.157	10.257
$5g_{7/2} \to 4f_{7/2}$	$6 \to 6$	0.000	0.000	100.000
	$6 \to 5$	0.686	1.815	10.737
	$5 \to 6$	-0.011	-0.396	10.229
	$5 \to 5$	-0.132	-8.597	68.172
	$5 \to 4$	0.019	-1.356	15.622
	$4 \to 5$	-0.012	-1.674	15.645
	$4 \to 4$	0.092	-3.960	44.663
	(continued on next page)			

Group	$F_i \rightarrow F_f$	$I_2^{if}[\%/\text{barn}^2]$	$I_1^{if}[\%/\text{barn}]$	$I_0^{if}[\%]$
	(continuation from previous page)			
	$4 \rightarrow 3$	0.215	-3.222	16.779
	$3 \rightarrow 4$	0.017	-1.209	16.880
	$3 \rightarrow 3$	-0.128	0.276	28.806
	$3 \rightarrow 2$	0.154	-2.547	14.578
	$2 \rightarrow 3$	-0.056	0.015	14.616
	$2 \rightarrow 2$	-0.170	1.909	19.277
	$2 \rightarrow 1$	0.016	-0.894	9.305
	$1 \rightarrow 2$	-0.067	0.639	9.264
	$1 \rightarrow 1$	-0.127	1.954	16.655
$5f_{5/2} \rightarrow 4d_{5/2}$	$5 \rightarrow 5$	0.000	0.000	100.000
	$5 \rightarrow 4$	1.818	4.016	17.855
	$4 \rightarrow 5$	-0.009	-1.151	16.732
	$4 \rightarrow 4$	0.726	-15.900	56.521
	$4 \rightarrow 3$	0.387	-5.470	24.330
	$3 \rightarrow 4$	0.119	-5.024	24.721
	$3 \rightarrow 3$	-0.004	-1.875	25.858
	$3 \rightarrow 2$	0.655	-7.222	24.615
	$2 \rightarrow 3$	-0.019	-1.680	24.982
	$2 \rightarrow 2$	-0.272	3.057	9.017
	$2 \rightarrow 1$	0.070	-3.176	20.090
	$1 \rightarrow 2$	-0.350	2.585	19.709
	$1 \rightarrow 1$	0.052	1.473	1.641
	$1 \rightarrow 0$	-0.122	0.940	10.826
	$0 \rightarrow 1$	-0.144	3.062	10.558

Bibliography

[1] N. Michel, N. S. Oreshkina, and C. H. Keitel, "Theoretical prediction of the fine and hyperfine structure of heavy muonic atoms," Phys. Rev. A **96**, 032510 (2017).

[2] B. Sikora, H. Cakir, N. Michel, V. Debierre, N. S. Oreshkina, N. A. Belov, V. A. Yerokhin, C. H. Keitel, and Z. Harman, "Improving the accuracy of the muon mass and magnetic moment anomaly via the bound-muon g factor," Phys. Rev. D **97**, 111301 (2018).

[3] N. Michel and N. S. Oreshkina, "Higher-order corrections for the dynamic hyperfine structure of muonic atoms," submitted, ArXiv e-prints arXiv:1809.06623 (2018).

[4] N. Michel, J. Zatorski, N. S. Oreshkina, and C. H. Keitel, "Non-perturbative analysis of nuclear shape effects on the bound electron g factor," submitted, ArXiv e-prints arXiv:1806.00405 (2018).

[5] A. Adamczak, A. Antognini, K. Kirch., N. Ritjoho, A. Skawaran, N. Berger, R. Pohl, F. Wauters, T. E. Cocolios, N. Seveijns, R. Dressler, R. Eichler, A. Knecht, A. Papa, E. Rapisarda, P. Indelicato, K. Jungmann, L. Willmann, N. Michel, N. S. Oreshkina, C. H. Keitel, M. Pospelov, P. Reiter, and S. Roccia, "On the analysis of the hyperfine splitting in muonic spectra: Re-185 and Re-187," in preparation (2018).

[6] N. S. Oreshkina, S. M. Cavaletto, N. Michel, Z. Harman, and C. H. Keitel, "Hyperfine splitting in simple ions for the search of the variation of fundamental constants," Phys. Rev. A **96**, 030501 (2017).

[7] W. H. Wollaston, "A method of examining refractive and dispersive powers, by prismatic reflection," Phil. Trans. R. Soc. Lond. **92**, 365 (1802).

[8] J. Fraunhofer, "Bestimmung des Brechungs- und des Farbenzerstreungs-Vermögens verschiedener Glasarten, in Bezug auf die Vervollkommnung achromatischer Fernröhre," Ann. Phys. **56**, 264 (1817).

[9] G. Kirchhoff and R. Bunsen, "Chemische Analyse durch Spectralbeobachtungen," Ann. Phys. **186**, 161 (1860).

[10] G. Kirchhoff and R. Bunsen, "Chemische Analyse durch Spectralbeobachtungen (zweite Abhandlung)," Ann. Phys. **189**, 337 (1861).

[11] A. J. Ångström, "Über die Fraunhofer'schen Linien im Sonnenspectrum," Ann. Phys. **193**, 290 (1862).

[12] J. J. Balmer, "Notiz über die Spectrallinien des Wasserstoffs," Ann. Phys. **261**, 80 (1885).

[13] A. J. Ångström, "Optische Untersuchungen," Ann. Phys. **170**, 141 (1853).

[14] W. Huggins, "On the Spectrum of the Flame of Hydrogen," Proc. R. Soc. Lond. **30**, 576 (1880).

[15] H. W. Vogel, "Über die neuen Wasserstofflinien und die Dissociation des Calciums," Berichte der deutschen chemischen Gesellschaft **13**, 274 (1880).

[16] J. R. Rydberg, *Recherches sur la constitution des spectres d'émission des éléments chimiques*, vol. 23 of *Kungliga vetenskapsakademiens handlingar* (Kungliga Vetenskapsakademien, 1889).

[17] I. Martinson and L. Curtis, "Janne Rydberg – his life and work," Nucl. Instrum. Methods Phys. Res. B **235**, 17 (2005). The Physics of Highly Charged Ions.

[18] T. Lyman, "The spectrum of hydrogen in the region of extremely short wave lengths," Ap. J. **23**, 181 (1906).

[19] F. Paschen, "Zur Kenntnis ultraroter Linienspektra," Ann. Phys. **332**, 537 (1908).

[20] F. S. Brackett, "Visible and Infra-Red Radiation of Hydrogen," Ap. J. **56**, 154 (1922).

[21] A. H. Pfund, "The Emission of Nitrogen and Hydrogen in the Infrared," J. Opt. Soc. Am. **9**, 193 (1924).

[22] C. J. Humphreys, "The sixth series in the spectrum of atomic hydrogen," J. Res. Natl. Bur. Stand. **50**, 1 (1953).

[23] J. J. Thomson, "Cathode Rays," Philos. Mag. **44**, 293 (1953).

[24] H. Rechenberg, "The electron in physics - selection from a chronology of the last 100 years," Eur. J. Phys. **18**, 145 (1997).

[25] E. Rutherford, "The scattering of α and β particles by matter and the structure of the atom," The London, Edinburgh, and Dublin Philos. Mag. and J. of Sci. **21**, 669 (1911).

[26] M. Planck, "Über das Gesetz der Energieverteilung im Normalspektrum," in "Von Kirchhoff bis Planck: Theorie der Wärmestrahlung in historisch-kritischer Darstellung," , H.-G. Schöpf, ed. (Vieweg+Teubner Verlag, Wiesbaden, 1978), pp. 178–191.

[27] N. Bohr, "On the Constitution of Atoms and Molecules," Philos. Mag. **26**, 1 (1913).

[28] J. J. Thomson, "On the structure of the atom: An investigation of the stability and periods of oscillation of a number of corpuscles arranged at equal intervals around the circumference of a circle; with application of the results to the theory of atomic structure," Philos. Mag. **7**, 6 (1904).

[29] A. Sommerfeld, "Zur Quantentheorie der Spektrallinien," Ann. Phys. **356**, 1 (1916).

[30] E. Schrödinger, "Quantisierung als Eigenwertproblem (erste Mitteilung)," Ann. Phys. **384**, 361 (1926).

[31] E. Schrödinger, "Quantisierung als Eigenwertproblem (zweite Mitteilung)," Ann. Phys. **384**, 489 (1926).

[32] E. Schrödinger, "Quantisierung als Eigenwertproblem (dritte Mitteilung)," Ann. Phys. **385**, 437 (1926).

[33] E. Schrödinger, "Quantisierung als Eigenwertproblem (vierte Mitteilung)," Ann. Phys. **386**, 109 (1926).

[34] W. Heisenberg, "Über quantentheoretische Umdeutung kinematischer und mechanischer Beziehungen." Z. Phys. **33**, 879 (1925).

[35] M. Born and P. Jordan, "Zur Quantenmechanik," Z. Phys. **34**, 858 (1925).

[36] M. Born, W. Heisenberg, and P. Jordan, "Zur Quantenmechanik. II." Z. Phys. **35**, 557 (1926).

[37] E. Schrödinger, "Über das Verhältnis der Heisenberg-Born-Jordanschen Quantenmechanik zu der meinen," Ann. Phys. **384**, 734.

[38] P. Zeeman, "Über einen Einfluss der Magnetisirung auf die Natur des von einer Substanz emittirten Lichtes," Verhandlungen der Physikalischen Gesellschaft (1896).

[39] G. E. Uhlenbeck and S. Goudsmit, "Ersetzung der Hypothese vom unmechanischen Zwang durch eine Forderung bezüglich des inneren Verhaltens jedes einzelnen Elektrons," Naturwissenschaften **47**, 953 (1925).

[40] P. A. M. Dirac, "The quantum theory of the electron," Proc. R. Soc. Lond. A **117**, 610 (1928).

[41] B. Thaller, *The Dirac equation* (Springer-Verlag, 1992).

[42] W. Greiner, *Relativistic Quantum Mechanics* (Springer-Verlag, Berlin Heidelberg, 2000), 3rd ed.

[43] W. E. Lamb and R. C. Retherford, "Fine Structure of the Hydrogen Atom by a Microwave Method," Phys. Rev. **72**, 241 (1947).

[44] J. E. Nafe, E. B. Nelson, and I. I. Rabi, "The Hyperfine Structure of Atomic Hydrogen and Deuterium," Phys. Rev. **71**, 914 (1947).

[45] P. Kusch and H. M. Foley, "Precision Measurement of the Ratio of the Atomic 'g Values' in the $^2P_{\frac{3}{2}}$ and $^2P_{\frac{1}{2}}$ States of Gallium," Phys. Rev. **72**, 1256 (1947).

[46] P. Kusch and H. M. Foley, "The Magnetic Moment of the Electron," Phys. Rev. **74**, 250 (1948).

[47] J. Schwinger, "On Quantum-Electrodynamics and the Magnetic Moment of the Electron," Phys. Rev. **73**, 416 (1948).

[48] T. W. Hänsch, A. L. Schawlow, and G. W. Series, "The spectrum of atomic hydrogen," Sci. Am. **240**, 94 (1979).

[49] S. G. Karshenboim, "Precision study of positronium: Testing bound state QED theory," Int. J. Mod. Phys. A **19**, 3879 (2004).

[50] A. Pineda and J. Soto, "Potential NRQED: The positronium case," Phys. Rev. D **59**, 016005 (1998).

[51] K. Pachucki and S. G. Karshenboim, "Complete Results for Positronium Energy Levels at Order $m\alpha^6$," Phys. Rev. Lett. **80**, 2101 (1998).

[52] A. Czarnecki, K. Melnikov, and A. Yelkhovsky, "Positronium S-state spectrum: Analytic results at $O(m\alpha^6)$," Phys. Rev. A **59**, 4316 (1999).

[53] J. Zatorski, "$O(m\alpha^6)$ corrections to energy levels of positronium with nonvanishing orbital angular momentum," Phys. Rev. A **78**, 032103 (2008).

[54] A. P. Mills and G. H. Bearman, "New Measurement of the Positronium Hyperfine Interval," Phys. Rev. Lett. **34**, 246 (1975).

[55] M. W. Ritter, P. O. Egan, V. W. Hughes, and K. A. Woodle, "Precision determination of the hyperfine-structure interval in the ground state of positronium," Phys. Rev. A **30**, 1331 (1984).

[56] K. Danzmann, M. S. Fee, and S. Chu, "Doppler-free laser spectroscopy of positronium and muonium: Reanalysis of the 1S-2S measurements," Phys. Rev. A **39**, 6072 (1989).

[57] D. Hagena, R. Ley, D. Weil, G. Werth, W. Arnold, and H. Schneider, "Precise measurement of n=2 positronium fine-structure intervals," Phys. Rev. Lett. **71**, 2887 (1993).

[58] M. S. Fee, A. P. Mills, S. Chu, E. D. Shaw, K. Danzmann, R. J. Chichester, and D. M. Zuckerman, "Measurement of the positronium 1^3S_1-2^3S_1 interval by continuous-wave two-photon excitation," Phys. Rev. Lett. **70**, 1397 (1993).

[59] K. P. Jungmann, "Past, Present and Future of Muonium," ArXiv e-prints arxiv:nucl-ex/0404013 (2004).

[60] D. Casperson, T. Crane, V. Hughes, P. Souder, R. Stambaugh, P. Thompson, H. Orth, G. zu Putlitz, H. Kaspar, H. Reist, and A. Denison, "A new high precision measurement of the muonium hyperfine structure interval $\Delta\nu_1$," Phys. Lett. B **59**, 397 (1975).

[61] W. Liu, M. G. Boshier, S. Dhawan, O. van Dyck, P. Egan, X. Fei, M. Grosse Perdekamp, V. W. Hughes, M. Janousch, K. Jungmann, D. Kawall, F. G. Mariam, C. Pillai, R. Prigl, G. zu Putlitz, I. Reinhard, W. Schwarz, P. A. Thompson, and K. A. Woodle, "High Precision Measurements of the Ground State Hyperfine Structure Interval of Muonium and of the Muon Magnetic Moment," Phys. Rev. Lett. **82**, 711 (1999).

[62] K. Pachucki, "$\alpha(Z\alpha)^2 E_F$ correction to hyperfine splitting in hydrogenic atoms," Phys. Rev. A **54**, 1994 (1996).

[63] S. G. Karshenboim, "Leading logarithmic corrections and uncertainty of Muonium hyperfine splitting calculations," Z. Phys. D **36**, 11 (1996).

[64] S. A. Blundell, K. T. Cheng, and J. Sapirstein, "All-Order Binding Corrections to Muonium Hyperfine Splitting," Phys. Rev. Lett. **78**, 4914 (1997).

[65] M. Nio and T. Kinoshita, "Radiative corrections to the muonium hyperfine structure. II. The $\alpha(Z\alpha)^2$ correction," Phys. Rev. D **55**, 7267 (1997).

[66] M. I. Eides, H. Grotch, and V. A. Shelyuto, "Second order in mass ratio radiative-recoil corrections to hyperfine splitting in muonium," Phys. Rev. D **58**, 013008 (1998).

[67] "Muonium Spectroscopy Experiment Using Microwave," http://museum.kek.jp/, called 2018-11-13.

[68] S. J. Brodsky and R. F. Lebed, "Production of the smallest QED atom: True Muonium $(\mu^+\mu^-)$," Phys. Rev. Lett. **102**, 213401 (2009).

[69] A. Bogomyagkov, V. Druzhinin, E. Levichev, A. Milstein, and S. Sinyatkin, "Low-energy electron-positron collider to search and study $(\mu^+\mu^-)$ bound state," ArXiv e-prints arxiv:physics.acc-ph/1708.05819 (2017).

[70] W. Y. Chang, "A Cloud-Chamber Study of Meson Absorption by Thin Pb, Fe, and Al Foils," Rev. Mod. Phys. **21**, 166 (1949).

[71] V. L. Fitch and J. Rainwater, "Studies of X-Rays from Mu-Mesonic Atoms," Phys. Rev. **92**, 789 (1953).

[72] J. A. Wheeler, "Some Consequences of the Electromagnetic Interaction between μ^--Mesons and Nuclei," Rev. Mod. Phys. **21**, 133 (1949).

[73] D. Hitlin, S. Bernow, S. Devons, I. Duerdoth, J. W. Kast, E. R. Macagno, J. Rainwater, C. S. Wu, and R. C. Barrett, "Muonic Atoms. I. Dynamic Hyperfine Structure in the Spectra of Deformed Nuclei," Phys. Rev. C **1**, 1184 (1970).

[74] A. Zehnder, F. Boehm, W. Dey, R. Engfer, H. Walter, and J. Vuilleumier, "Charge parameters, isotope shifts, quadrupole moments, and nuclear excitation in muonic $^{170-174,176}$Yb," Nucl. Phys. A **254**, 315 (1975).

[75] R. Powers, F. Boehm, P. Vogel, A. Zehnder, T. King, A. Kunselman, P. Roberson, P. Martin, G. Miller, R. Welsh, and D. A. Jenkins, "Muonic X-ray study of the charge distribution of ^{165}Ho," Nucl. Phys. A **262**, 493 (1976).

[76] Y. Yamazaki, E. B. Shera, M. V. Hoehn, and R. M. Steffen, "Measurement and model-independent analysis of the x rays of muonic ^{150}Sm and ^{152}Sm," Phys. Rev. C **18**, 1474 (1978).

[77] Y. Tanaka, R. M. Steffen, E. B. Shera, W. Reuter, M. V. Hoehn, and J. D. Zumbro, "Precision Muonic-Atom Measurements of Nuclear Quadrupole Moments and the Sternheimer Effect in Rare-Earth Atoms," Phys. Rev. Lett. **51**, 1633 (1983).

[78] Y. Tanaka, R. M. Steffen, E. B. Shera, W. Reuter, M. V. Hoehn, and J. D. Zumbro, "Systematics of ground-state quadrupole moments of odd-A deformed nuclei determined with muonic M x rays," Phys. Rev. C **29**, 1830 (1984).

[79] Y. Tanaka, R. M. Steffen, E. B. Shera, W. Reuter, M. V. Hoehn, and J. D. Zumbro, "Measurement and analysis of the muonic x rays of ^{151}Eu and ^{153}Eu," Phys. Rev. C **29**, 1897 (1984).

[80] P. Bergem, G. Piller, A. Rueetschi, L. A. Schaller, L. Schellenberg, and H. Schneuwly, "Nuclear polarization and charge moments of ^{208}Pb from muonic x rays," Phys. Rev. C **37**, 2821 (1988).

[81] R. Powers, F. Boehm, A. Zehnder, A. Kunselman, and P. Roberson, "A precision determination of the radial charge parameters and the quadrupole moment of 181Ta using muonic X-rays," Nucl. Phys. A **278**, 477 (1977).

[82] G. Fricke, C. Bernhardt, K. Heilig, L. Schaller, L. Schellenberg, E. Shera, and C. Dejager, "Nuclear Ground State Charge Radii from Electromagnetic Interactions," At. Data Nucl. Data Tables **60**, 177 (1995).

[83] E. Borie and G. A. Rinker, "The energy levels of muonic atoms," Rev. Mod. Phys. **54**, 67 (1982).

[84] S. Devons and I. Duerdoth, *Muonic Atoms* (Springer US, Boston, MA, 1995), pp. 295–423.

[85] C. S. Wu and L. Wilets, "Muonic Atoms and Nuclear Structure," Ann. Rev. of Nucl. Sci. **19**, 527 (1969).

[86] G. Rinker, "Static and dynamic muonic-atom codes-MUON and RURP," Comp. Phys. Comm. **16**, 221 (1979).

[87] R. Pohl, A. Antognini, F. Nez, F. D. Amaro, F. Biraben, J. M. R. Cardoso, D. S. Covita, A. Dax, S. Dhawan, L. M. P. Fernandes, A. Giesen, T. Graf, T. W. Hänsch, P. Indelicato, L. Julien, C.-Y. Kao, P. Knowles, E.-O. Le Bigot, Y.-W. Liu, J. A. M. Lopes, L. Ludhova, C. M. B. Monteiro, F. Mulhauser, T. Nebel, P. Rabinowitz, J. M. F. dos Santos, L. A. Schaller, K. Schuhmann, C. Schwob, D. Taqqu, J. F. C. A. Veloso, and F. Kottmann, "The size of the proton," Nature **466**, 213 (2010).

[88] A. Antognini, F. Nez, K. Schuhmann, F. D. Amaro, F. Biraben, J. M. R. Cardoso, D. S. Covita, A. Dax, S. Dhawan, M. Diepold, L. M. P. Fernandes, A. Giesen, A. L. Gouvea, T. Graf, T. W. Hänsch, P. Indelicato, L. Julien, C.-Y. Kao, P. Knowles, F. Kottmann, E.-O. Le Bigot, Y.-W. Liu, J. A. M. Lopes, L. Ludhova, C. M. B. Monteiro, F. Mulhauser, T. Nebel, P. Rabinowitz, J. M. F. dos Santos, L. A. Schaller, C. Schwob, D. Taqqu, J. F. C. A. Veloso, J. Vogelsang, and R. Pohl, "Proton Structure from the Measurement of 2S-2P Transition Frequencies of Muonic Hydrogen," Science **339**, 417 (2013).

[89] R. Pohl, F. Nez, L. M. P. Fernandes, F. D. Amaro, F. Biraben, J. M. R. Cardoso, D. S. Covita, A. Dax, S. Dhawan, M. Diepold, A. Giesen, A. L. Gouvea, T. Graf, T. W. Hänsch, P. Indelicato, L. Julien, P. Knowles, F. Kottmann, E.-O. Le Bigot, Y.-W. Liu, J. A. M. Lopes, L. Ludhova, C. M. B. Monteiro, F. Mulhauser, T. Nebel, P. Rabinowitz, J. M. F. dos Santos, L. A. Schaller, K. Schuhmann, C. Schwob, D. Taqqu, J. F. C. A. Veloso, and A. Antognini, "Laser spectroscopy of muonic deuterium," Science **353**, 669 (2016).

[90] A. Beyer, L. Maisenbacher, A. Matveev, R. Pohl, K. Khabarova, A. Grinin, T. Lamour, D. C. Yost, T. W. Hänsch, N. Kolachevsky, and T. Udem, "The rydberg constant and proton size from atomic hydrogen," Science **358**, 79 (2017).

[91] P. J. Mohr, D. B. Newell, and B. N. Taylor, "CODATA recommended values of the fundamental physical constants: 2014," Rev. Mod. Phys. **88**, 035009 (2016).

[92] J. Arrington and I. Sick, "Evaluation of the Proton Charge Radius from Electron–Proton Scattering," J. Phys. Chem. Ref. Data **44**, 031204 (2015).

[93] H. Fleurbaey, S. Galtier, S. Thomas, M. Bonnaud, L. Julien, F. m. c. Biraben, F. m. c. Nez, M. Abgrall, and J. Guéna, "New Measurement of the $1S - 3S$ Transition Frequency of Hydrogen: Contribution to the Proton Charge Radius Puzzle," Phys. Rev. Lett. **120**, 183001 (2018).

[94] G. W. Bennett, B. Bousquet, H. N. Brown, G. Bunce, R. M. Carey, P. Cushman, G. T. Danby, P. T. Debevec, M. Deile, H. Deng, W. Deninger, S. K. Dhawan, V. P. Druzhinin, L. Duong, E. Efstathiadis, F. J. M. Farley, G. V. Fedotovich, S. Giron, F. E. Gray, D. Grigoriev, M. Grosse-Perdekamp, A. Grossmann, M. F. Hare, D. W. Hertzog, X. Huang, V. W. Hughes, M. Iwasaki, K. Jungmann, D. Kawall, M. Kawamura, B. I. Khazin, J. Kindem, F. Krienen, I. Kronkvist, A. Lam, R. Larsen, Y. Y. Lee, I. Logashenko, R. McNabb, W. Meng, J. Mi, J. P. Miller, Y. Mizumachi, W. M. Morse, D. Nikas, C. J. G. Onderwater, Y. Orlov, C. S. Özben, J. M. Paley, Q. Peng, C. C. Polly, J. Pretz, R. Prigl, G. zu Putlitz, T. Qian, S. I. Redin, O. Rind, B. L. Roberts, N. Ryskulov, S. Sedykh, Y. K. Semertzidis, P. Shagin, Y. M. Shatunov, E. P. Sichtermann, E. Solodov, M. Sossong, A. Steinmetz, L. R. Sulak, C. Timmermans, A. Trofimov, D. Urner, P. von Walter, D. Warburton, D. Winn, A. Yamamoto, and D. Zimmerman, "Final report of the E821 muon anomalous magnetic moment measurement at BNL," Phys. Rev. D **73**, 072003 (2006).

[95] B. Odom, D. Hanneke, B. D'Urso, and G. Gabrielse, "New Measurement of the Electron Magnetic Moment Using a One-Electron Quantum Cyclotron," Phys. Rev. Lett. **97**, 030801 (2006).

[96] D. Hanneke, S. Fogwell, and G. Gabrielse, "New Measurement of the Electron Magnetic Moment and the Fine Structure Constant," Phys. Rev. Lett. **100**, 120801 (2008).

[97] A. Peterman, Helv. Phys. Act **30**, 407 (1957).

[98] C. M. Sommerfield, "Magnetic Dipole Moment of the Electron," Phys. Rev. **107**, 328 (1957).

[99] C. M. Sommerfield, "The magnetic moment of the electron," Ann. Phys. **5**, 26 (1958).

[100] S. Laporta and E. Remiddi, "The analytical value of the electron (g - 2) at order α^3 in QED," Phys. Lett. B **379**, 283 (1996).

[101] T. Kinoshita and M. Nio, "Improved α^4 term of the electron anomalous magnetic moment," Phys. Rev. D **73**, 013003 (2006).

[102] T. Aoyama, M. Hayakawa, T. Kinoshita, and M. Nio, "Revised Value of the Eighth-Order Contribution to the Electron $g - 2$," Phys. Rev. Lett. **99**, 110406 (2007).

[103] T. Aoyama, M. Hayakawa, T. Kinoshita, and M. Nio, "Tenth-order electron anomalous magnetic moment: Contribution of diagrams without closed lepton loops," Phys. Rev. D **91**, 033006 (2015).

[104] T. Aoyama, M. Hayakawa, T. Kinoshita, and M. Nio, "Erratum: Tenth-order electron anomalous magnetic moment: Contribution of diagrams without closed lepton loops [Phys. Rev. D 91, 033006 (2015)]," Phys. Rev. D **96**, 019901 (2017).

[105] G. Gabrielse, D. Hanneke, T. Kinoshita, M. Nio, and B. Odom, "New Determination of the Fine Structure Constant from the Electron g Value and QED," Phys. Rev. Lett. **97**, 030802 (2006).

[106] G. Gabrielse, D. Hanneke, T. Kinoshita, M. Nio, and B. Odom, "Erratum: New Determination of the Fine Structure Constant from the Electron g Value and QED [Phys. Rev. Lett. 97, 030802 (2006)]," Phys. Rev. Lett. **99**, 039902 (2007).

[107] H. Haffner, T. Beier, N. Hermanspahn, H.-J. Kluge, W. Quint, S. Stahl, J. Verdu, and G. Werth, "High-Accuracy Measurement of the Magnetic Moment Anomaly of the Electron Bound in Hydrogenlike Carbon," Phys. Rev. Lett. **85**, 5308 (2000).

[108] S. Sturm, F. Köhler, J. Zatorski, A. Wagner, Z. Harman, G. Werth, W. Quint, C. Keitel, and K. Blaum, "High-precision measurement of the atomic mass of the electron," Nature **506**, 467 (2014).

[109] J. Verdu, S. Djekic, H. Haffner, S. Stahl, T. Valenzuela, M. Vogel, G. Werth, H.-J. Kluge, and W. Quint, "Electronic g Factor of Hydrogenlike Oxygen $^{16}O^{7+}$," Phys. Rev. Lett. **92**, 093002 (2004).

[110] S. Sturm, A. Wagner, B. Schabinger, J. Zatorski, Z. Harman, W. Quint, G. Werth, C. H. Keitel, and K. Blaum, "g factor of hydrogenlike $^{28}Si^{13+}$," Phys. Rev. Lett. **107**, 023002 (2011).

[111] A. Wagner, S. Sturm, F. Köhler, D. A. Glazov, A. V. Volotka, G. Plunien, W. Quint, G. Werth, V. M. Shabaev, and K. Blaum, "g Factor of Lithiumlike Silicon $^{28}Si^{11+}$," Phys. Rev. Lett. **110**, 033003 (2013).

[112] F. Köhler, K. Blaum, M. Block, S. Chenmarev, S. Eliseev, D. A. Glazov, M. Goncharov, J. Hou, A. Kracke, D. A. Nesterenko, Y. N. Novikov, W. Quint, E. M. Ramirez, V. M. Shabaev, S. Sturm, A. V. Volotka, and G. Werth, "Isotope dependence of the Zeeman effect in lithium-like calcium." Nat. Commun. **7**, 10246 (2016).

[113] S. Sturm, G. Werth, and K. Blaum, "Electron g-factor determinations in Penning traps," Ann. Phys. **525**, 620 (2013).

[114] L. S. Brown and G. Gabrielse, "Geonium theory: Physics of a single electron or ion in a Penning trap," Rev. Mod. Phys. **58**, 233 (1986).

[115] S. Sturm, M. Vogel, F. Köhler-Langes, W. Quint, K. Blaum, and G. Werth, "High-Precision Measurements of the Bound Electron's Magnetic Moment," Atoms **5**, 4 (2017).

[116] J. R. Crespo López-Urrutia, A. Dorn, R. Moshammer, and J. Ullrich, "The Freiburg Electron Beam Ion Trap/Source Project FreEBIT," Phys. Scr. **1999**, 502 (1999).

[117] M. Vogel and W. Quint, "Aspects of fundamental physics in precision spectroscopy of highly charged ions in Penning traps," Ann. Phys. **525**, 505 (2013).

[118] M. Vogel, Z. Andelkovic, G. Birkl, S. Ebrahimi, V. Hannen, D. von Lindenfels, A. Martin, T. Murböck, W. Nörtershäuser, W. Quint, S. Schmidt, D. M. Segal, R. C. Thompson, J. Vollbrecht, C. Weinheimer, and M. Wiesel, "Penning-trap experiments for spectroscopy of highly-charged ions at HITRAP," Phys. Scr. **2015**, 014066 (2015).

[119] G. Breit, "The Magnetic Moment of the Electron," Nature **122**, 649 (1928).

[120] S. G. Karshenboim, "Non-relativistic calculations of the g factor of a bound electron," Phys. Lett. A **266**, 380 (2000).

[121] K. Pachucki and U. D. Jentschura, V. A. Yerokhin, "Nonrelativistic QED approach to the Bound-Electron g Factor," Phys. Rev. Lett. **93**, 150401 (2004).

[122] K. Pachucki, U. D. Jentschura, and V. A. Yerokhin, "Erratum: Nonrelativistic QED Approach to the Bound-Electron g Factor [Phys. Rev. Lett. 93, 150401 (2004)]," Phys. Rev. Lett. **94**, 229902 (2005).

[123] K. Pachucki and A. Czarnecki and U. D. Jentschura and V. A. Yerokhin, "Complete two-loop correction to the bound-electron g factor," Phys. Rev. A **72**, 022108 (2005).

[124] A. Czarnecki and R. Szafron, "Light-by-light scattering in the lamb shift and the bound electron g factor," Phys. Rev. A **94**, 060501 (2016).

[125] A. Czarnecki, M. Dowling, J. Piclum, and R. Szafron, "Two-Loop Binding Corrections to the Electron Gyromagnetic Factor," Phys. Rev. Lett. **120**, 043203 (2018).

[126] T. Beier, "The g_j factor of a bound electron and the hyperfine structure splitting in hydrogenlike ions," Phys. Rep. **339**, 79 (2000).

[127] S. G. Karshenboim, V. G. Ivanov, and V. M. Shabaev, "Vacuum Polarization in a Hydrogen-like Relativistic Atom: g Factor of a Bound Electron," J. Exp. Theor. Phys. Lett. **93**, 477 (2001).

[128] V. A. Yerokhin, P. Indelicato, and V. M. Shabaev, "Self-Energy Correction to the Bound-Electron g Factor in H-like Ions," Phys. Rev. Lett. **89**, 143001 (2002).

[129] V. A. Yerokhin, P. Indelicato, and V. M. Shabaev, "Evaluation of the self-energy correction to the g factor of S states in H-like ions," Phys. Rev. A **69**, 052503 (2004).

[130] R. Lee, A. Milstein, I. Terekhov, and S. G. Karshenboim, "Virtual light-by-light scattering and the g factor of a bound electron," Phys. Rev. A **71**, 052501 (2005).

[131] R. N. Lee, A. I. Milstein, I. S. Terekhov, and S. G. Karshenboim, "g factor of the bound electron and muon," Can. J. Phys. **85**, 541 (2007).

[132] V. A. Yerokhin and U. D. Jentschura, "Electron Self-Energy in the Presence of a Magnetic Field: Hyperfine Splitting and g Factor," Phys. Rev. Lett. **100**, 163001 (2008).

[133] V. A. Yerokhin and U. D. Jentschura, "Self-energy correction to the hyperfine splitting and the electron g factor in hydrogenlike ions," Phys. Rev. A **81**, 012502 (2010).

[134] V. A. Yerokhin and Z. Harman, "One-loop electron self-energy for the bound-electron g factor," Phys. Rev. A **95**, 060501 (2017).

[135] V. A. Yerokhin and Z. Harman, "Two-loop QED corrections with closed fermion loops for the bound-electron g factor," Phys. Rev. A **88**, 042502 (2013).

[136] B. Sikora, V. A. Yerokhin, N. S. Oreshkina, H. Cakir, C. H. Keitel, and Z. Harman, "Theory of the two-loop self-energy correction to the g factor in non-perturbative Coulomb fields," ArXiv e-prints arXiv:1804.05733 (2018).

[137] D. A. Glazov and V. M. Shabaev, "Finite nuclear size correction to the bound-electron g factor in a hydrogenlike atom," Phys. Lett. A **297**, 408 (2002).

[138] A. V. Nefiodov, G. Plunien, and G. Soff, "Nuclear-polarization correction to the bound-electron g factor in heavy hydrogenlike ions," Phys. Rev. Lett. **89**, 081802 (2002).

[139] A. V. Volotka and G. Plunien, "Nuclear Polarization Study: New Frontiers for Tests of QED in Heavy Highly Charged Ions," Phys. Rev. Lett. **113**, 023002 (2014).

[140] M. I. Eides and T. J. S. Martin, "Universal Binding and Recoil Corrections to Bound State g Factors in Hydrogenlike Ions," Phys. Rev. Lett. **105**, 100402 (2010).

[141] K. Pachucki, "Nuclear mass correction to the magnetic interaction of atomic systems," Phys. Rev. A **78**, 012504 (2008).

[142] V. M. Shabaev, "QED theory of the nuclear recoil effect on the atomic g factor," Phys. Rev. A **64**, 052104 (2001).

[143] V. M. Shabaev and V. A. Yerokhin, "Recoil Correction to the Bound-Electron g Factor in H-Like Atoms to All Orders in αZ," Phys. Rev. Lett. **88**, 091801 (2002).

[144] J. Zatorski, N. S. Oreshkina, C. H. Keitel, and Z. Harman, "Nuclear Shape Effect on the g Factor of Hydrogenlike Ions," Phys. Rev. Lett. **108**, 063005 (2012).

[145] F. Köhler, S. Sturm, A. Kracke, G. Werth, W. Quint, and K. Blaum, "The electron mass from g-factor measurements on hydrogen-like carbon $^{12}C^{5+}$," J. Phys. B: At. Mol. Opt. Phys. **48**, 144032 (2015).

[146] J. Zatorski, B. Sikora, S. G. Karshenboim, S. Sturm, F. Köhler-Langes, K. Blaum, C. H. Keitel, and Z. Harman, "Extraction of the electron mass from g-factor measurements on light hydrogenlike ions," Phys. Rev. A **96**, 012502 (2017).

[147] V. A. Yerokhin, K. Pachucki, Z. Harman, and C. H. Keitel, "QED theory of the nuclear magnetic shielding in hydrogenlike ions," Phys. Rev. Lett. **107**, 043004 (2011).

[148] G. Werth, H. Häffner, N. Hermanspahn, H.-J. Kluge, W. Quint, and J. Verdú, "The g Factor of Hydrogenic Ions: A Test of Bound State QED," in "The Hydrogen Atom: Precision Physics of Simple Atomic Systems," , S. G. Karshenboim, F. Bassani, F. Pavone, M. Inguscio, and T. Hänsch, eds. (Springer Berlin Heidelberg, Berlin, Heidelberg, 2001), pp. 204–220.

[149] V. M. Shabaev, D. A. Glazov, N. S. Oreshkina, A. V. Volotka, G. Plunien, H.-J. Kluge, and W. Quint, "g-Factor of Heavy Ions: A New Access to the Fine Structure Constant," Phys. Rev. Lett. **96**, 253002 (2006).

[150] V. A. Yerokhin, E. Berseneva, Z. Harman, I. I. Tupitsyn, and C. H. Keitel, "g Factor of Light Ions for an Improved Determination of the Fine-Structure Constant," Phys. Rev. Lett. **116**, 100801 (2016).

[151] V. A. Yerokhin, E. Berseneva, Z. Harman, I. I. Tupitsyn, and C. H. Keitel, "Weighted difference of g factors of light Li-like and H-like ions for an improved determination of the fine-structure constant," Phys. Rev. A **94**, 022502 (2016).

[152] V. M. Shabaev, I. I. Tupitsyn, V. A. Yerokhin, G. Plunien, and G. Soff, "Dual Kinetic Balance Approach to Basis-Set Expansions for the Dirac Equation," Phys. Rev. Lett. **93**, 130405 (2004).

[153] S. Weinberg, *The Quantum theory of fields. Vol. 1: Foundations* (Cambridge University Press, 2005), 3rd ed.

[154] W. H. Furry, "On Bound States and Scattering in Positron Theory," Phys. Rev. **81**, 115 (1951).

[155] C. Itzykson and J.-B. Zuber, *Quantum field theory* (Dover, 2005).

[156] M. E. Peskin and D. V. Schroeder, *An Introduction to quantum field theory* (Addison-Wesley, 1995).

[157] V. Shabaev, "Two-time Green's function method in quantum electrodynamics of high-Z few-electron atoms," Phys. Rep. **356**, 119 (2002).

[158] E. A. Uehling, "Polarization Effects in the Positron Theory," Phys. Rev. **48**, 55 (1935).

[159] E. H. Wichmann and N. M. Kroll, "Vacuum Polarization in a Strong Coulomb Field," Phys. Rev. **101**, 843 (1956).

[160] G. Källen, "Fourth Order Vacuum Polarization," K. Dan. Vidensk. Selsk. Mat.-Fys. Medd. **29**, 17 (1955).

[161] L. W. Fullerton and G. A. Rinker, "Accurate and efficient methods for the evaluation of vacuum-polarization potentials of order $Z\alpha$ and $Z\alpha^2$," Phys. Rev. A **13**, 1283 (1976).

[162] A. A. Elizarov, V. M. Shabaev, N. S. Oreshkina, and I. I. Tupitsyn, "Hyperfine splitting in heavy ions with the nuclear magnetization distribution determined from experiments on muonic atoms," Nucl. Instrum. Methods Phys. Res. B **235**, 65 (2005).

[163] R. Barbieri, J. A. Mignaco, and E. Remiddi, "On the fourth-order radiative corrections to the electron-photon vertex," Lett. Nuovo Cimento **3**, 588 (1970).

[164] R. Barbieri, J. A. Mignaco, and E. Remiddi, "Electron form factors up to fourth order. - I," Nuovo Cimento A **11**, 824 (1972).

[165] R. Barbieri, J. A. Mignaco, and E. Remiddi, "Electron form factors up to fourth order. - II," Nuovo Cimento A **11**, 865 (1972).

[166] R. Barbieri and E. Remiddi, "Infra-red divergences and adiabatic switching. Fourth-order vaccum polarization," Nuovo Cimento A **13**, 99 (1973).

[167] P. Indelicato, "Nonperturbative evaluation of some QED contributions to the muonic hydrogen $n = 2$ Lamb shift and hyperfine structure," Phys. Rev. A **87**, 022501 (2013).

[168] D. A. Varshalovich, A. N. Moskalev, and V. K. Khersonskii, *Quantum Theory of Angular Momentum* (World Scientific, Singapore, 1988).

[169] M. Rose, *Relativistic Electron Theory* (John Wiley and Sons, 1961).

[170] W. R. Johnson, S. A. Blundell, and J. Sapirstein, "Finite basis sets for the Dirac equation constructed from B splines," Phys. Rev. A **37**, 307 (1988).

[171] G. W. F. Drake and S. P. Goldman, "Application of discrete-basis-set methods to the Dirac equation," Phys. Rev. A **23**, 2093 (1981).

[172] L. W. Wansbeek, S. Schlesser, B. K. Sahoo, A. E. L. Dieperink, C. J. G. Onderwater, and R. G. E. Timmermans, "Charge radii of radium isotopes," Phys. Rev. C **86**, 015503 (2012).

[173] H. D. Vries, C. D. Jager, and C. D. Vries, "Nuclear charge-density-distribution parameters from elastic electron scattering," At. Data Nucl. Data Tables **36**, 495 (1987).

[174] L.-B. Wang, P. Mueller, K. Bailey, G. W. F. Drake, J. P. Greene, D. Henderson, R. J. Holt, R. V. F. Janssens, C. L. Jiang, Z.-T. Lu, T. P. O'Connor, R. C. Pardo, K. E. Rehm, J. P. Schiffer, and X. D. Tang, "Laser Spectroscopic Determination of the ^{6}He Nuclear Charge Radius," Phys. Rev. Lett. **93**, 142501 (2004).

[175] H. De Witte, A. N. Andreyev, N. Barré, M. Bender, T. E. Cocolios, S. Dean, D. Fedorov, V. N. Fedoseyev, L. M. Fraile, S. Franchoo, V. Hellemans, P. H. Heenen, K. Heyde, G. Huber, M. Huyse, H. Jeppessen, U. Köster, P. Kunz, S. R. Lesher, B. A. Marsh, I. Mukha, B. Roussière, J. Sauvage, M. Seliverstov, I. Stefanescu, E. Tengborn, K. Van de Vel, J. Van de Walle, P. Van Duppen, and Y. Volkov, "Nuclear Charge Radii of Neutron-Deficient Lead Isotopes Beyond $N = 104$ Midshell Investigated by In-Source Laser Spectroscopy," Phys. Rev. Lett. **98**, 112502 (2007).

[176] P. Mueller, I. A. Sulai, A. C. C. Villari, J. A. Alcántara-Núñez, R. Alves-Condé, K. Bailey, G. W. F. Drake, M. Dubois, C. Eléon, G. Gaubert, R. J. Holt, R. V. F. Janssens, N. Lecesne, Z.-T. Lu, T. P. O'Connor, M.-G. Saint-Laurent, J.-C. Thomas, and L.-B. Wang, "Nuclear Charge Radius of ^{8}He," Phys. Rev. Lett. **99**, 252501 (2007).

[177] K. Kirch, "Slow Muons and Muonium," ArXiv e-prints (2016).

[178] I. Angeli and K. Marinova, "Table of experimental nuclear ground state charge radii: An update," At. Data Nucl. Data Tables **99**, 69 (2013).

[179] Evaluated Nuclear Structure Data Files (ENSDF) (http://www.nndc.bnl.gov/ensdf/).

[180] J. D. Jackson, *Classical electrodynamics* (Wiley, New York, 1999), 3rd ed.

[181] W. Zickendraht, "Why Are Most Nuclei Axially Symmetric?" Ann. Phys. **503**, 229 (1991).

[182] W. R. Johnson, *Atomic Structure Theory* (Springer, Berlin Heidelberg, 2007), 1st ed.

[183] L. D. Landau and L. M. Lifshitz, *Quantum Mechanics Non-Relativistic Theory, Third Edition: Volume 3* (Butterworth-Heinemann, 1981), 3rd ed.

[184] J. Friar and J. Negele, "Breit equation analysis of recoil corrections to muonic atom energy levels," Phys. Lett. B **46**, 5 (1973).

[185] P. Vogel, "Electron Screening in Muonic Atoms," Phys. Rev. A **7**, 63 (1973).

[186] H. Bethe and E. Salpeter, *Quantum Mechanics of One- and Two-Electron Systems* (Plenum Publishing Corporation, 1977).

[187] Y. S. Kozhedub, O. V. Andreev, V. M. Shabaev, I. I. Tupitsyn, C. Brandau, C. Kozhuharov, G. Plunien, and T. Stöhlker, "Nuclear deformation effect on the binding energies in heavy ions," Phys. Rev. A **77**, 032501 (2008).

[188] E. Y. Korzinin, N. S. Oreshkina, and V. M. Shabaev, "Hyperfine Splitting of Low-Lying Levels in Heavy Li-Like Ions," Phys. Scr. **71**, 464 (2005).

[189] N. J. Stone, "Table of nuclear magnetic dipole and electric quadrupole moments," At. Data Nucl. Data Tables **90**, 75 (2005).

[190] A. Bohr and V. F. Weisskopf, "The Influence of Nuclear Structure on the Hyperfine Structure of Heavy Elements," Phys. Rev. **77**, 94 (1950).

[191] R. M. Steffen, "Precision measurements of nuclear quadrupole moments by muonic x-rays," Hyperfine Interact. **24**, 223 (1985).

[192] J. J. Sakurai, *Modern Quantum Mechanics* (Addison-Wesley, 1994), 2nd ed.

[193] "*NIST Digital Library of Mathematical Functions*," http://dlmf.nist.gov/, Release 1.0.19 of 2018-06-22. F. W. J. Olver, A. B. Olde Daalhuis, D. W. Lozier, B. I. Schneider, R. F. Boisvert, C. W. Clark, B. R. Miller and B. V. Saunders, eds.

[194] V. Pisano, G. Puddu, P. Quarati, and L. Sulis, "The use of the master equation in the cascade of exotic systems in a pure Coulomb field," Nuovo Cimento A **72**, 27 (1982).

[195] W. Dey, P. Ebersold, H. Leisi, F. Scheck, H. Walter, and A. Zehnder, "Nuclear spectroscopic ground-state quadrupole moments from muonic atoms," Nucl. Phys. A **326**, 418 (1979).

[196] S. D. Wit, G. Backenstoss, C. Daum, J. Sens, and H. Acker, "Measurement and analysis of muonic X-ray spectra in deformed nuclei," Nucl. Phys. **87**, 657 (1966).

[197] B. Fricke, "Zur vakuumpolarisation in myonenatomen," Z. Phys. A **218**, 495 (1969).

[198] J. Pearson, "Vacuum polarization induced by the nuclear quadrupole moment in mu-mesonic atoms," Nucl. Phys. **45**, 401 (1963).

[199] M.-y. Chen, "Nuclear Polarization in Muonic Atoms of Deformed Nuclei," Phys. Rev. C **1**, 1176 (1970).

[200] Wolfram Research, Inc., "Mathematica, Version 11.3," Champaign, IL, 2018.

[201] F. Johansson *et al.*, *mpmath: a Python library for arbitrary-precision floating-point arithmetic (version 0.18)* (2013). `http://mpmath.org/`.

[202] H. Schopper, *Nuclear Charge Radii* (Springer, Berlin, Heidelberg, 2004).

[203] J. Konijn, J. Panman, J. Koch, W. V. Doesburg, G. Ewan, T. Johansson, G. Tibell, K. Fransson, and L. Tauscher, "Pionic 4f - 3d transition in 181Ta, natural Re, and 209Bi and the strong interaction level shift and width of the pionic 3d state," Nucl. Phys. A **326**, 401 (1979).

[204] "*LTP Experiments*," https://www.psi.ch/ltp/experiments, called 2018-09-20.

[205] "*LTP Facilities*," https://www.psi.ch/ltp/facilities, called 2018-09-20.

[206] N. Stone, "Table of nuclear electric quadrupole moments," At. Data Nucl. Data Tables **111-112**, 1 (2016).

[207] E. Rapisarda, *Private communication* (2018).

[208] S. Vogiatzi, *Master Thesis* (Eidgenössische Technische Hochschule, Zürich, 2018).

[209] H.-J. Kluge, T. Beier, K. Blaum, L. Dahl, S. Eliseev, F. Herfurth, B. Hofmann, O. Kester, S. Koszudowski, C. Kozhuharov, G. Maero, W. Nörtershäuser, J. Pfister, W. Quint, U. Ratzinger, A. Schempp, R. Schuch, T. Stöhlker, R. Thompson, M. Vogel, G. Vorobjev, D. Winters, and G. Werth, "HITRAP: A Facility at GSI for Highly Charged Ions," in "Current Trends in Atomic Physics," , vol. 53 of *Advances in Quantum Chemistry*, S. Salomonson and E. Lindroth, eds. (Academic Press, 2008), pp. 83 – 98.

[210] J. Zatorski, "Nuclear deformation correction to the *g*-factor of hydrogen-like ions in S-state," (2013). Working notes.

[211] V. M. Shabaev, "Finite nuclear size corrections to the energy levels of the multicharged ions," J. Phys. B **26**, 1103 (1993).

[212] S. G. Karshenboim and V. G. Ivanov, "Finite-nuclear-size contribution to the *g* factor of a bound electron: Higher-order effects," Phys. Rev. A **97**, 022506 (2018).

[213] S. G. Karshenboim, R. N. Lee, and A. I. Milstein, "*g* factor of an electron or muon bound by an arbitrary central potential," Phys. Rev. A **72**, 042101 (2005).

[214] N. Michel, *Precision Physics of the Bound Electron g-factor* (Master Thesis, Ruprecht-Karls-Universität, Heidelberg; http://hdl.handle.net/11858/00-001M-0000-0028-48C8-0, 2015).

[215] M. Rose, *Relativistic Electron Theory* (John Wiley and Sons, 1961).

[216] B. Hahn, D. G. Ravenhall, and R. Hofstadter, "High-Energy Electron Scattering and the Charge Distributions of Selected Nuclei," Phys. Rev. **101**, 1131 (1956).

[217] F. Träger, "On the charge distribution of calcium nuclei," Z. Phys. A **299**, 33 (1981).

[218] P. Möller, J. Nix, W. Myers, and W. Swiatecki, "Nuclear Ground-State Masses and Deformations," At. Data Nucl. Data Tables **59**, 185 (1995).

[219] P. Ring and P. Schuck, *The Nuclear Many-Body Problem* (Springer-Verlag, 1980).

[220] D. A. Close, J. J. Malanify, and J. P. Davidson, "Nuclear charge distributions deduced from the muonic atoms of ^{232}Th, ^{235}U, ^{238}U, and ^{239}Pu," Phys. Rev. C **17**, 1433 (1978).

[221] F. Buchinger, E. B. Ramsay, E. Arnold, W. Neu, R. Neugart, K. Wendt, R. E. Silverans, P. Lievens, L. Vermeeren, D. Berdichevsky, R. Fleming, D. W. L. Sprung, and G. Ulm, "Systematics of nuclear ground state properties in $^{78-100}$Sr by laser spectroscopy," Phys. Rev. C **41**, 2883 (1990).

[222] M. I. Eides and H. Grotch, "Gyromagnetic Ratios of Bound Particles," Ann. Phys. **260**, 191 (1997).

[223] A. Czarnecki, K. Melnikov, and A. Yelkhovsky, "Anomalous magnetic moment of a bound electron," Phys. Rev. A **63**, 012509 (2000).

[224] T. Aoyama, M. Hayakawa, T. Kinoshita, and M. Nio, "Tenth-order QED contribution to the electron *g*-2 and an improved value of the fine structure constant," Phys. Rev. Lett. **109**, 111807 (2012).

[225] K. Pachucki, "Nuclear mass correction to the magnetic interaction of atomic systems," Phys. Rev. A **78**, 012504 (2008).

[226] H. Grotch, "Electron *g* Factor in Hydrogenic Atoms," Phys. Rev. Lett. **24**, 39 (1970).

[227] A. Czarnecki, B. Krause, and W. J. Marciano, "Electroweak Corrections to the Muon Anomalous Magnetic Moment," Phys. Rev. Lett. **76**, 3267 (1996).

[228] J. Prades, E. de Rafael, and A. Vainshtein, *The hadronic light-by-light scattering contribution to the muon and electron anomalous magnetic moments* (World Scientific, Singapore, 2010), vol. 20 of *Advanced Series on Directions in High Energy Physics*, chap. 9, pp. 303–317.

[229] D. Nomura and T. Teubner, "Hadronic contributions to the anomalous magnetic moment of the electron and the hyperfine splitting of muonium," Nucl. Phys. B **867**, 236 (2013).

[230] A. Kurz, T. Liu, P. Marquard, and M. Steinhauser, "Hadronic contribution to the muon anomalous magnetic moment to next-to-next-to-leading order," Phys. Lett. B **734**, 144 (2014).

[231] A. Edmonds, *Angular Momentum in Quantum Mechanics* (Princeton University Press, 1960), 2nd ed.

[232] J. Brown and A. Carrington, *Rotational Spectroscopy of Diatomic Molecules* (Cambridge University Press, 2003).

[233] B. Podolsky, "Quantum-Mechanically Correct Form of Hamiltonian Function for Conservative Systems," Phys. Rev. **32**, 812 (1928).

[234] R. d. L. Kronig and I. I. Rabi, "The Symmetrical Top in the Undulatory Mechanics," Phys. Rev. **29**, 262 (1927).

Acknowledgements

In the following lines, I want to express my gratitude to all people who contributed to this thesis:

First of all, I want to thank Honorarprof. Dr. Christoph H. Keitel for the possibility to work on my PhD project in his division at such a prestigious institute and inspiring environment, and for all the support of my project.

I am thankful to Dr. Natalia S. Oreshkina for the supervision, the numerous discussions, advice and at the same time enough space to follow my own ideas.

I am very grateful to Dr. Jacek Zatorski for the fruitful and pleasant collaboration.

I wish to thank PD Dr. Wolfgang Quint for his efforts in being the second referee and Prof. Dr. Maurits W. Haverkort and Prof. Dr. Kurt Roth for being part of the examination committee.

Furthermore, I am very thankful to Dr. Aldo Antognini, Dr. Andreas Knecht, Dr. Elisa Rapisarda, Alexander A. Skawran, Stella M. Vogiatzi, and everyone else from the MuX collaboration. It was a great motivation and inspiration to have a theoretical project which is at the same time closely connected to exciting experiments.

I am also greatly indebted to Halil Cakir for his excellent updated codes for the numerical calculation with B-splines.

I want to thank my office colleagues Dr. Shika Bhadoria, Dr. Jiří Daněk, Kamil Dzikowski, Dr. Jonas Gunst, Dr. Nicolas Teeny, and all other division members for the good atmosphere, nice conversations and interesting discussions in the office and during breaks.

I wish to thank the secretary of our division, Sibel Babacan, for the excellent organization and administration.

Many thanks to Dr. Shikha Bhadoria, Halil Cakir, Dr. Jiří Daněk, Dr. Vincent Debierre, Kamil Dzikowski, PD Dr. Zoltán Harman, Dr. Bastian Sikora, and Dr. Jacek Zatorski for proofreading the thesis.

Finally, I am deeply grateful to my family and to Kasia for their love and support, especially during the occasionally stressful times as a doctoral student.